SUBARRAY SELECTION IN OCTAVE ARRAYS

A THESIS SUBMITTED TO
THE GRADUATE SCHOOL OF NATURAL AND APPLIED SCIENCES
OF
MIDDLE EAST TECHNICAL UNIVERSITY

BY

ALİ RIZA KADEROĞLU

IN PARTIAL FULFILLMENT OF THE REQUIREMENTS
FOR
THE DEGREE OF MASTER OF SCIENCE
IN
ELECTRICAL AND ELECTRONICS ENGINEERING

FEBRUARY 2022

Approval of the thesis:

SUBARRAY SELECTION IN OCTAVE ARRAYS

submitted by **ALİ RIZA KADEROĞLU** in partial fulfillment of the requirements for the degree of **Master of Science in Electrical and Electronics Engineering Department, Middle East Technical University** by,

Prof. Dr. Halil Kalıpçılar
Dean, Graduate School of **Natural and Applied Sciences** ——————

Prof. Dr. İlkay Ulusoy
Head of Department, **Electrical and Electronics Engineering** ——————

Prof. Dr. Tolga Çiloğlu
Supervisor, **Electrical and Electronics Engineering, METU** ——————

Examining Committee Members:

Prof. Dr. Umut Orguner
Electrical and Electronics Engineering, METU ——————

Prof. Dr. Tolga Çiloğlu
Electrical and Electronics Engineering, METU ——————

Prof. Dr. Kemal Leblebicioğlu
Electrical and Electronics Engineering, METU ——————

Assist. Prof. Dr. Gökhan Muzaffer Güvensen
Electrical and Electronics Engineering, METU ——————

Assist. Prof. Dr. Yakup Özkazanç
Electrical and Electronics Engineering, Hacettepe University ——————

Date: 04.02.2022

I hereby declare that all information in this document has been obtained and presented in accordance with academic rules and ethical conduct. I also declare that, as required by these rules and conduct, I have fully cited and referenced all material and results that are not original to this work.

Name, Surname: Ali Rıza Kaderoğlu

Signature   :

ABSTRACT

SUBARRAY SELECTION IN OCTAVE ARRAYS

Kaderoğlu, Ali Rıza

M.S., Department of Electrical and Electronics Engineering

Supervisor: Prof. Dr. Tolga Çiloğlu

February 2022, 121 pages

Sensor layout of the octave array is designed to process a frequency range of several octaves. Array aperture of the highest octave band is limited to uniform line array (ULA) segment at the center. Forming a sparse array layout for the highest frequency band by using some of the remaining elements apart from ULA could bring some advantages such as higher array gain and better detection performance. Using a sparse array has a drawback of violating the spatial Nyquist limit, which may cause high sidelobes to appear in the beampattern. It is aimed to select an optimum layout with larger aperture length and higher gain without being affected by disadvantages of using sparse arrays. Performance of the selected layout depends on the used direction of arrival estimation (DOA) method. In this thesis, both conventional and coarray based DOA methods are reviewed firstly. Then, several optimization problems are stated for selecting a subarray layout. These problems use some array parameters such as peak-to-sidelobe level (PSL), Cramer-Rao bound, method of interval errors (MIE) and redundancy. Minimization of PSL is used to reduce the high sidelobe levels. To minimize DOA estimation error, CRB and MIE are used as cost functions. PSL constraint is added to minimization of CRB problem to prevent grating lobes in the array beampattern. Minimum redundancy array and robust minimum redundancy

array are obtained by using redundancy and fragility in the optimization problems. Performances of proposed array layouts are compared with the existing solution using extensive computer simulations.

Keywords: Direction of arrival (DOA) estimation, sensor arrays, optimization problem, co-array, beamforming

ÖZ

OKTAV DİZİNLERDE ALT DİZİN SEÇİMİ

Kaderoğlu, Ali Rıza
Yüksek Lisans, Elektrik ve Elektronik Mühendisliği Bölümü
Tez Yöneticisi: Prof. Dr. Tolga Çiloğlu

Şubat 2022 , 121 sayfa

Oktav dizinin sensör yerleşimi birden çok sayıda oktavı içeren bir frekans aralığına göre yapılmıştır. En yüksek oktav bandı için dizinin merkezinde bulunan düzgün doğrusal dizin kullanılmaktadır. En yüksek frekans bandı için doğrusal dizin dışında kalan elemanları ile aralıklı bir sensor yerleşimi kullanımı yüksek dizin kazancı ve daha iyi tespit performansı gibi çeşitli avantajlar sunabilir. Düzgün olmayan bir doğrusal dizin kullanımında daha geniş bir açıklığa erişilmesine karşılık elemanlar arası uzaklıkta Nyquist limiti ihmal edildiği için ışıma deseninde yüksek yan lob seviyeleri elde edilebilmektedir. Daha büyük açıklığa ve dizin kazancına sahip olan, aynı zamanda aralıklı yerleşimin olumsuz yönlerinden etkilenmeyen bir eniyi dizin seçimi hedeflenmektedir. Seçilen dizinin performansı kullanılan yön kestirim yöntemine göre değişir. Bu tezde öncelikle hem geleneksel hem de ortak dizin yön bulma yöntemleri incelenmektedir. Daha sonra alt dizin seçimi problemi için çeşitli eniyileme problemleri belirtilmektedir. Bu problemler yan lob seviyesi, Cramer-Rao sınırı, aralık hataları yöntemi ve yedeklilik gibi parametreleri kullanmaktadır. Yan lob bastırımı probleminde yüksek yan lobların bastırımı, Cramer-Rao ve aralık hataları yöntemi problemlerinde daha düşük yön kestirimi hatası, yan lob kısıdına sahip Cramer-Rao

probleminde dizinde çıkan yan loblardan kurtulmak ve düşük yön kestirim hatası, yedeklilik problemlerinde ise en küçük yedekli dizin ve sağlam en küçük yedekli dizini elde etmek hedeflenmektedir. Önerilen dizin yerleşimi ve mevcut çözümün performansları çok sayıda bilgisayar simülasyonu kullanılarak karşılaştırılacaktır.

Anahtar Kelimeler: Geliş yönü kestirimi, sensör dizinleri, eniyileme problemi, ortak dizin, ışın demetleme

To my family...

ACKNOWLEDGMENTS

TABLE OF CONTENTS

LIST OF TABLES

TABLES

LIST OF FIGURES

FIGURES

LIST OF ABBREVIATIONS

BCRB   Bayesian Cramer Rao Bound

CRB   Cramer Rao Bound

DI   Directivity Index

DOA   Direction of Arrival

DOF   Degree of Freedom

dB   Decibel

deg   Degree

FIM   Fisher Information Matrix

FLOP   Floating Point Operation

GA   Genetic Algorithm

hp   Half-power

LCMV   Linearly Constrained Minimum Variance

MDL   Minimum Description Length

ML   Maximum Likelihood

MAP   Maximum Aposteriori Estimator

MLE   Maximum Likelihood Estimator

MHA   Minimum Hole Array

MRA   Minimum Redundancy Array

MIE   Method of Interval Errors

MSE   Mean Squared Error

MTC   Monte Carlo

MUSIC   Multiple Signal Classification

MVDR   Minimum Variance Distortionless Response

NN   Null-to-null

PSL	Peak-to-sidelobe Level
RMRA	Robust Minimum Redundancy Array
RMSE	Root Mean Square Error
SINR	Signal to Interference-Noise Ratio
SMI	Sample Matrix Inverse
SNR	Signal to Noise Ratio
SS	Spatial Smoothing
SSC	Spatially Smoothed Coarray
SS MUSIC	Spatially Smoothed MUSIC
SS MVDR	Spatially Smoothed MVDR
TOA	Three Octave Array
ULA	Uniform Line Array

CHAPTER 1

INTRODUCTION

In this thesis, it is mainly focused on subarray selection from a given (sparse) sensor array in order to improve certain performance metrics by employing different optimization programs. This problem has a practical aspect as well, since such sparse arrays are commonly utilized in towed passive/active sonar systems. These systems collect sound signals emitted/reflected from underwater targets [1] with a hydrophone array towed by the main platform. In general, these towed systems have an "octave array" sensor structure in order to process signals within a larger bandwith with similar array characteristics such as beamwidth and array gain.

An octave array is a combination of uniform line arrays which are designed for a frequency range of several octaves [2]. The shortest uniform line array (ULA) at the center of the octave array is used for the highest frequency band. For ULA, angular resolution is improved when its element spacings are greater than half of the wavelength. Unfortunately, this improvement causes high sidelobe levels. Despite having higher sidelobe levels, using an array layout for the high frequency band with non uniformly spaced elements could bring some improvements to the octave array for DOA estimation. Selection of this non uniformly spaced subarray can be achieved via an optimization program, which will assure that certain performance metrics will be met while other constraints are satisfied. Motivation of this thesis is to study this optimization problem (with different cost functions and constraints) and provide different solutions for the narrowband source scenario with an octave array.

This chapter will provide an introduction by giving a background review, followed by the proposed methods for the optimization, contributions and the outline of the thesis.

1.1 Literature Review

In this section, brief reviews on direction of arrival (DOA) estimation methods, coarray based techniques, array layout optimization and performance bounds are given.

Arrays with M sensors could reach only $O(M)$ degrees of fredom using conventional DOA estimation methods. Conventional methods can be divided into two main groups which are beamformers and subspace methods. Beamformers are classified as data-independent and data-dependent. Bartlett beamformer is a data-independent method [3, 4], whereas Capon [5], linearly constrained minimum variance (LCMV) beamformer [6], loaded sample matrix inverse (SMI) [7] and robust Capon [8] are some of the data-dependent adaptive beamformers. Multiple apodization is also a data-dependent method which brings the high angular resolution and lower sidelobes with less computational cost [9, 10]. As conventional subspace methods, MUSIC [11] and ESPRIT [12] are two of the most common techniques.

$O(M^2)$ DOF could be reached with M sensors by using second-order statistics from the sensor data. Detecting more sources than the number of sensors is achieved by exploiting the difference coarray. Some of the well-known sparse linear arrays used for coarray based methods are perfect array [13], minimum hole array (MHA) [14], minimum redundancy array (MRA) [13], robust minimum redundancy array (RMRA) [15] and nested array [16]. With these arrays, methods like KR-MUSIC [17] and SS-MUSIC [16] are applied on the coarray data for obtaining a higher DOFs.

In array layout optimization, discrete parameters are used since the solution space is formed by the fixed sensor positions. Evolutionary algorithms such as genetic algorithm [18–20] and particle swarm optimization [21] are used for array selection problem. Selecting an array layout among a large amount of sensor positions is named as array thinning in the literature [22]. In most of the array thinning problems, optimization tries to minimize peak to sidelobe level of the beampattern of an array steered to a fixed direction. Iterative FFT technique has been proposed for a faster convergence to reach the minimum possible peak-to-sidelobe level (PSL) [23]. Hybrid genetic algorithm and modified iterative Fourier transform (HGAMIFT) algorihm has been developed to use both enhanced search ability of genetic algorithm and

fast convergence velocity of MIFT [24]. In addition to minimizing PSL, gross error minimization is used for optimizing the array geometry for DOA estimation [25].

After selecting an array layout, its DOA estimation performance could be evaluated using a number of performance bounds. Cramer Rao bound is a lower bound on the variance of DOA angle estimation [26]. It is a tight bound when the SNR is high. Therefore, it can give reliable estimates in the asymptotic region of MSE curves. Both threshold and asymptotic regions of MSE curves could be approximated using method of interval errors (MIE) [27].

1.2 Proposed Optimization Problems

In a large portion of this thesis, new array layouts for processing signals within the high frequency band in an octave array are studied. For this purpose, six different optimization problems are solved using genetic algorithm. These optimization problems are based on the parameters such as PSL, CRB, MIE, redundancy and fragility. A brief description of each problem is as follows.

1. **Minimizing the maximum of the PSL values for different steering angles:** Minimizing PSL is chosen as the cost function for most of the array thinning optimizations [23, 24]. As sidelobe levels decrease, probability of detection of false targets also reduces. For calculating PSL of different array layouts in the optimization, Bartlett beamformer is employed to generate the beampattern. It is also used as the DOA estimation method for evaluating the performance of the final layout as a result of the optimization. According to the simulation results presented in Chapter 6, array layout obtained with this cost function has a better source separation performance and less DOA estimation error than the ULA since the aperture of the new layout is wider.

2. **Minimizing the Bayesian CRB for a constant SNR value:** With this cost function, it is aimed to obtain an array layout whose DOA estimation error for the selected SNR value is minimized. Selecting a layout that can operate in lower SNR values might be achieved if the selected SNR value is less than threshold SNR. Instead of using deterministic CRB which depends on a single

angle, Bayesian CRB is calculated by assuming the source DOA being random with uniform distribution. Bartlett beamformer is used as the DOA estimation method for evaluating the result of this optimization problem. According to the simulation results presented in Chapter 6, obtained array layout has a poor performance when the number of sensors is fixed in the optimization due to the grating lobes caused by the sparsity.

3. **Minimizing the Bayesian CRB for a constant SNR value with a PSL constraint:** Aim of this optimization problem is solving grating lobe problem obtained as a result of the second optimization problem. Performance of the resultant layout is evaluated by using Bartlett beamformer. Array layout obtained with this cost function in Chapter 6 has a better source separation performance and less DOA estimation error than the other layouts using Bartlett beamformer.

4. **Minimizing the Bayesian MIE for a constant SNR value:** It is aimed to obtain an array layout with less DOA estimation error similar to the second optimization problem. MIE gives better approximations than CRB for threshold SNR region. For a better estimation for low SNR values, MIE is used as the cost function rather than CRB. There is a similarity between resultant layout and ULA when there is a sensor number constraint. Bartlett beamformer is used to evaluate the performance of the layout obtained by this optimization.

5. **Minimizing the redundancy:** Aim of this optimization is to select MRA from the elements of three octave array. SS-MUSIC is used as the DOA estimation method for the obtained MRA. It is seen that MRA detect more sources than the other layouts in Chapter 6 since SS-MUSIC is a coarray based method with $O\left(M^2\right)$ elements.

6. **Minimizing the redundancy with a fragility constraint:** Aim of this optimization is to select RMRA from the elements of three octave array to obtain a robust layout as ULA against sensor failures. SS-MUSIC is used as the DOA estimation method for the obtained MRA. Since the available elements for layout selection optimization are fixed, resultant layout is similar to ULA.

Each of these problems are examined in detail in Chapter 6 along with Monte Carlo analyses.

1.3 Contributions

Amount of information for octave arrays is limited in the literature although it has been in use for many years. Main aim of this thesis is to propose new array layouts with elements from outside the ULA for the three octave array. Contributions from this thesis could be summarized as follows:

- Bayesian CRB for single source is employed for estimating the RMS error performance of an array [28]. In this study, Bayesian CRB is utilized as the cost function for subarray selection problem. Benefit of using Bayesian CRB over deterministic CRB is that the average performance over all possible angles is obtained.

- Bayesian MIE for single source is employed for estimating the RMS error performance of an array since it can approximate both asymptotic and threshold SNR regions. In this study, Bayesian MIE is also utilized as the cost function for subarray selection problem. Benefit of using Bayesian MIE over deterministic MIE is that the average performance over all possible angles is obtained

- Array layouts using different optimization cost functions are proposed for the highest frequency band for the octave arrays instead of ULA. In the optimizations, PSL, Bayesian CRB, Bayesian CRB with PSL constraint, Bayesian MIE, redundancy and redundancy with fragility constraint are used as the cost functions. It is explained in detail why these parameters are chosen in Section 1.2.

- Coarray based DOA estimation methods are applied on MRA and RMRA whose elements are selected among the elements of the octave array.

1.4 Thesis Outline

The outline of this thesis is as follows. Narrowband array signal model and array performance measures are described in Chapter 2. The classical DOA estimation methods are reviewed in Chapter 3, and coarray based DOA estimation methods are reviewed in Chapter 4 in addition to coarray parameters and sparse array examples.

Detailed information about genetic algorihm and cost functions are given in Chapter 5. Optimization results and performance comparisions are shown in Chapter 6. Conclusions and future work are provided in Chapter 7.

In Chapter 2, narrowband signal model is explained with array manifold vector, source and noise signals. Then, array beampattern is defined and performance measures are described.

Chapter 3 starts with beamforming definition. Then, Bartlett and Capon beamformer are reviwed as a DOA estimation method. After explaining beamformer types, MUSIC and dual apodization methods are described. As a solution for coherent sources, spatial smoothing process is explained.

Chapter 4 covers the coarray related topics. After defining coarray parameters, some types of sparse linear arrays are shown. Then, DOA estimation methods for difference coarrays are explained.

Chapter 5 gives detailed information for the array selection optimization. Firstly, genetic algorithm is presented. Then, different cost functions for layout optimization are explained.

In Chapter 6, first, three octave array and performance metrics for the optimization results are given. Then, optimization problems for selecting 16 sensors and their results with performance comparisons are presented. After that, optimization problems for selecting more than 16 sensors and their results with performance comparisons are shown. Lastly, three different array layouts are proposed for dual apodization method and their results are also given.

In Chapter 7, conclusions of the thesis work and required inprovements for the future are given.

CHAPTER 2

ARRAY SIGNAL MODEL

Sensor arrays have many applications both in civil and military systems. Probably the most well known applications are radar and sonar systems. The main uses of these systems are to increase the signal to noise/interference ratio of the signal of interest, determine the angle of arrival of the signal, or to separate signals in a crowded environment. In this chapter the general approach for array signal processing is given, along with the notation and array signal model.

2.1 Array Manifold Vector

In the array signal model, array properties and phase differences between sensors while receiving signal of interest are represented with array manifold vector. It is also known as *array steering vector*. It depends on the array geometry, wavelength and direction of source. The angle convention used in this study is given in Figure 2.1. Any given unit vector is represented with (ϕ, θ) pair. ϕ angle is measured on xy plane from x-axis to the vertical projection of the unit vector on xy plane. θ angle on the other hand is measured from the z-axis to the unit vector on the plane containing z-axis and the unit vector. With this angle convention, the unit vector pointing to (ϕ, θ) direction will be in the following form.

$$\mathbf{g} = \begin{bmatrix} \cos(\phi)\sin(\theta) \\ \sin(\phi)\sin(\theta) \\ \cos(\theta) \end{bmatrix} \tag{2.1}$$

One common assumption in these applications is the far-field assumption. As the distance between the source and sensors increases, wavefront of the received signal can
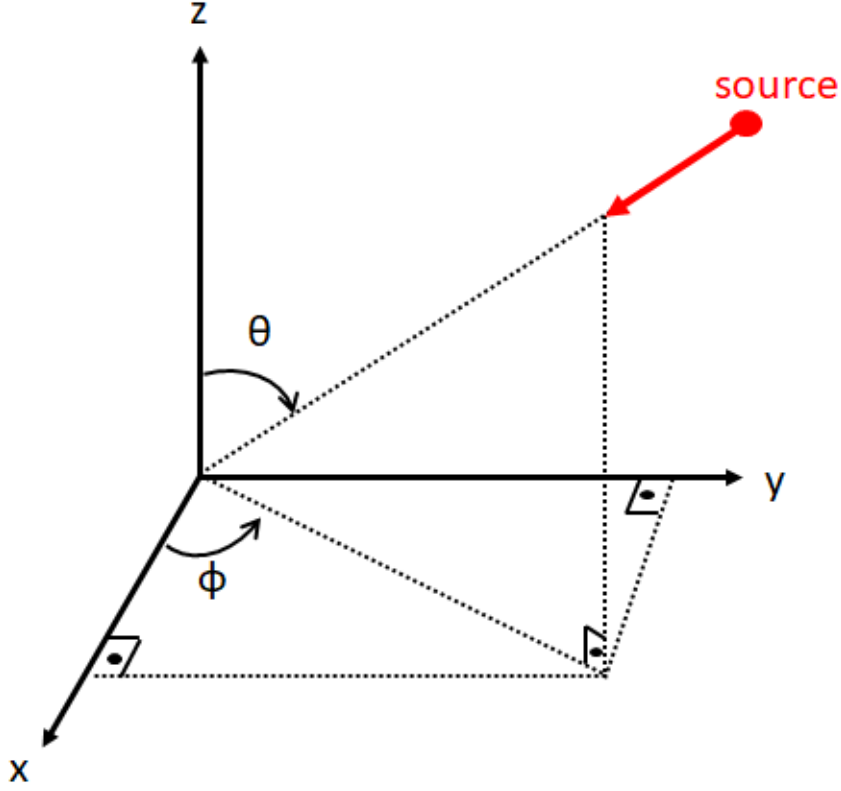
Figure 2.1: Spherical coordinate system and angle definitions

be approximated as planar. This approximation can be used to simplify the manifold definition. In order to satisfy the far-field assumption, distance between the source and array should be greater than $2D^2/\lambda$ [29]. λ denotes operating wavelength and D denotes the aperture which is the largest physical dimension of the array. For a uniform line array, there will be an equal time delay between adjacent sensors with identical signals (assuming negligible propagation loss along the array) when the source is in the far field [30]. The signal impinging on the sensor array, will have the following time delays associated with each sensor.

$$\tau_n = \frac{-\mathbf{g}^{\mathrm{T}}\mathbf{p}_n}{c} \tag{2.2}$$

$$\mathbf{p}_n = \begin{bmatrix} p_{x_n} \\ p_{y_n} \\ p_{z_n} \end{bmatrix} \tag{2.3}$$

8

where $\mathbf{p}_n$ is the position vector of the nth sensor and c is the propagation speed of the incoming wave. The resulting phase delays in each channel is as follows,

$$\omega_c = 2\pi f_c \quad [rad/s] \tag{2.4}$$

$$\lambda_c = \frac{c}{f_c} \quad [m] \tag{2.5}$$

$$\omega_c \tau_n = -\frac{\omega_c \mathbf{g}^T \mathbf{p}_n}{c} = -\frac{2\pi f_c}{c} \mathbf{g}^T \mathbf{p}_n = -\frac{2\pi}{\lambda_c} \mathbf{g}^T \mathbf{p}_n. \tag{2.6}$$

The equivalent effect of this time delay in frequency domain is given in 2.7.

$$\mathcal{F}\{x(t - \tau_n)\} = X(\omega) \exp(-j\omega\tau_n) \tag{2.7}$$

For narrow-band signals, this can be approximated as,

$$\mathcal{F}^{-1}\{X(\omega) \exp(-j\omega\tau_n)\} \approx \mathcal{F}^{-1}\{X(\omega) \exp(-j\omega_c\tau_n)\}$$
$$= x(t) \exp(-j\omega_c\tau_n). \tag{2.8}$$

We can arrange the phase delays for each channel in vector form as,

$$\mathbf{a}(\phi,\theta) = \begin{bmatrix} \exp(-j\omega_c\tau_0) \\ \exp(-j\omega_c\tau_1) \\ \vdots \\ \exp(-j\omega_c\tau_{M-1}) \end{bmatrix} = \begin{bmatrix} \exp(-j\frac{2\pi}{\lambda_c}\mathbf{g}^T\mathbf{p}_0) \\ \exp(-j\frac{2\pi}{\lambda_c}\mathbf{g}^T\mathbf{p}_1) \\ \vdots \\ \exp(-j\frac{2\pi}{\lambda_c}\mathbf{g}^T\mathbf{p}_{M-1}) \end{bmatrix}. \tag{2.9}$$

2.9 is generally referred to as *the array manifold vector* [28].

2.2 Narrowband Signal Model

Aim of the array signal processing is to detect *N* sources by using *M* sensors. Different signal models are employed for this purpose in different DF (Direction Finding) problems. Narrowband signal model is probably the most common signal model used in various array signal problems in the literature [28]. This model uses the following assumptions,

- Sources are in the far-field of the array.

- Sources are modelled as point emitters.

9

- Medium between the source and array is homogeneous.

- Number of sources N is known or estimated from the data.

- Sensor array is assumed to be LTI.

Additionally the source signal *s(t)* is modeled as a baseband signal. It has both real and imaginary parts which are denoted by $s_I(t)$ and $s_Q(t)$ respectively as given in 2.10a. The emitted signal, $x(t)$, is the modulated version of this baseband signal around a carrier frequency.

$$s(t) = s_I(t) + js_Q(t) \tag{2.10a}$$

$$x(t) = 2Re\left(s(t)e^{j\omega_c t}\right) \tag{2.10b}$$

$$x(t) = s(t)e^{j\omega_c t} + s^*(t)e^{-j\omega_c t} \tag{2.10c}$$

$$X(\omega) = S(\omega - \omega_c) + S^*(-(\omega + \omega_c)) \tag{2.10d}$$

$$x(t) = 2\left[s_I(t)\cos(\omega_c t) - s_Q(t)\sin(\omega_c t)\right] \tag{2.10e}$$

$$x(t) = 2\sqrt{s_I^2(t) + s_Q^2(t)}\cos\left(\omega_c t + \arctan\left(\frac{s_Q(t)}{s_I(t)}\right)\right) \tag{2.10f}$$

$$x(t) = \alpha(t)\cos(\omega_c t + \Psi(t)) \tag{2.10g}$$

The emitted signal $x(t)$ will be received by the sensor array and each element will read the signal with different time delays, $\{\tau_n\}_{n=1}^M$. This delay, along with element responses $\{h_n(t)\}$ can be modeled in time and frequency domain as in (2.11) and (2.12) respectively.

$$\tilde{y}_n(t) = h_n(t) * x(t - \tau_n) + e_n(t) \tag{2.11}$$

$$\tilde{Y}_n(\omega) = H_n(\omega)X(\omega)\exp(-j\omega\tau_n) + E_n(\omega) \tag{2.12}$$

where $e_n(t)$ is the additive noise for the nth channel. By inserting $X(\omega)$ into 2.12, $\tilde{Y}_n(\omega)$ can be written in terms of source signal $S(\omega)$.

$$\tilde{Y}_n(\omega) = H_n(\omega) \left[S(\omega - \omega_c) + S^*(-(\omega + \omega_c))\right] \exp(-j\omega\tau_n) + E_n(\omega) \quad (2.13)$$

After receiving the bandpass signal, $\tilde{y}_n(t)$ is demodulated for further processing. To demodulate $\tilde{y}_n(t)$, the signal is multiplied by the conjugate of the complex carrier signal and then filtered by a low pass filter.

$$\bar{y}_n(t) = \tilde{y}_n(t)e^{-j\omega_c t} \quad (2.14)$$

$$\bar{Y}_n(\omega) = \frac{H_n(\omega + \omega_c)}{2} \left[S(\omega) + S^*(-\omega - 2\omega_c)\right] \exp(-j(\omega + \omega_c)\tau_n)$$

$$+ E_n(\omega + \omega_c) \quad (2.15)$$

$$y_n(t) = \text{LPF}\{\bar{y}_n(t)\} \quad (2.16)$$

$$Y_n(\omega) = \frac{H_n(\omega + \omega_c)}{2} S(\omega) \exp(-j(\omega + \omega_c)\tau_n) + E_n(\omega + \omega_c) \quad (2.17)$$

Amplitude of the frequency response of the source signal $S(\omega)$ decays rapidly with the frequency if received signal is narrowband. In [28, p. 34], narrowband criterion is given as

$$B\frac{D}{c} \ll 1 \quad (2.18)$$

where B is the bandwidth of the received signal, D is the array aperture and c is the signal propagation speed. With this narrowband signal assumption, 2.17 reduces to

$$Y_n(\omega) = H_n(\omega_c)S(\omega) \exp(-j\omega_c\tau_n) + E_n(\omega + \omega_c) \quad (2.19)$$

$$y_n(t) = H_n(\omega_c)s(t) \exp(-j\omega_c\tau_n) + e_n(t) \quad (2.20)$$

If the sensors are assumed to be identical, their frequency responses will also be the same. To simplify the equation, we can set $H_n(\omega_c) = 2$ for $n = \{0, 1, ..., M - 1\}$ where *M* is the number of sensors in the array.

$$y_n(t) = exp(-j\omega_c\tau_n)s(t) + e_n(t) \quad (2.21)$$

Note that the exponential term in 2.21 is the nth entry of the array manifold vector. Consequently the received baseband signals for all sensors could be written in a vector form $\mathbf{y(t)}$ as follows,

$$\mathbf{y(t)} = \mathbf{a}(\phi, \theta)s(t) + \mathbf{e(t)} \quad (2.22)$$

11

where $t = kT$, T is the sampling period and $k = \{0, 1, ..., N - 1\}$ and N representing the number of snapshots. When we have multiple sources, narrowband signal model can be written as

$$\mathbf{y(t)} = \mathbf{AS} + \mathbf{e}(t) \tag{2.23}$$

$$\mathbf{A} = [\mathbf{a}(\phi_1, \theta_1), \mathbf{a}(\phi_2, \theta_2), \cdots, \mathbf{a}(\phi_P, \theta_P)] \tag{2.24}$$

$$\mathbf{S} = [s_1(t), s_2(t), \cdots, s_P(t)]^{\mathrm{T}} \tag{2.25}$$

where P is the number of sources, $\mathbf{A}$ is the array manifold matrix which contains the manifold vectors for the source directions and $\mathbf{S}$ is the source signal vector.

2.3 Source Signal

There are different models used for modeling the source signal. Deterministic and Gaussian random signal approaches are two of the commonly used model in the array signal model [28]. In the deterministic approach, properties like frequency, duration, bandwidth and type of the signal is known. There is not any randomness in the signal. In the Gaussian random approach, source signal is assumed to be a Gaussian random process with known mean vector and covariance matrix. A white Gaussian process is most commonly used here with a zero mean vector and a diagonal covariance matrix. Since the source signal in the narrowband model is a baseband signal, a complex white Gaussian process is used and modeled as both stationary and circularly symmetric.

Note: A complex Gaussian random vector $\in \mathbb{C}^N$ can be formed by two independent real jointly Gaussian random vectors in $\mathbb{R}^N$. A complex Gaussian random vector is said to be circularly symmetric when both its mean and pseudo-covariance are zero. They can be defined only with their covariance matrix if they are both jointly Gaussian and circularly symmetric [31].

2.4 Noise Signal

In the array signal model, noise signal is also modelled as complex white Gaussian process. It is both spatially and temporally white and circularly symmetric. Being

spatially white means that noise samples received at every sensor are uncorrelated from each other. Since it is a stationary process, noise samples received in the same channel are also uncorrelated.

2.5 Array Beampattern

Array beampattern defines the complex gain of the array to a unit plane wave of frequency ω and direction (ϕ, θ) [28]. It is an important parameter for evaluation of the array performance. It can be written as,

$$B(\phi, \theta) = \mathbf{w}^{\mathrm{H}} \left(\mathbf{R}(\phi, \theta) \circ \mathbf{a}(\phi, \theta) \right) \tag{2.26}$$

where $\mathbf{w} = [w_0, w_1, \cdots, w_{M-1}]^{\mathrm{T}}$ is the weight vector applied to M sensors, $\mathbf{R}(\phi, \theta) = [R_0(\phi, \theta), R_1(\phi, \theta), \cdots, R_{M-1}(\phi, \theta)]^{\mathrm{T}}$ is the element pattern vector of M sensors, $\mathbf{a}(\phi, \theta)$ is the array manifold vector, $\circ$ denotes Hadamard (element-wise) product and $\mathbf{H}$ is the Hermitian (complex conjugate) operator. With the assumption of identical element pattern, element pattern vector in 2.26 becomes scalar,

$$B(\phi, \theta) = R_0(\phi, \theta) \mathbf{w}^{\mathrm{H}} \mathbf{a}(\phi, \theta) \tag{2.27}$$

If the element response is ignored or sensors are omni-directional, 2.27 reduces to 2.28. This result is also known as *array factor*.

$$B(\phi, \theta) = \mathbf{w}^{\mathrm{H}} \mathbf{a}(\phi, \theta) \tag{2.28}$$

In order to plot the pattern and analyze its parameters, power pattern in linear and in dB scales are calculated as,

$$B_{p,l}(\phi, \theta) = \left| \mathbf{w}^{\mathrm{H}} \mathbf{a}(\phi, \theta) \right|^2 \tag{2.29}$$

$$B_p(\phi, \theta) = 20 \log_{10} \left| \mathbf{w}^{\mathrm{H}} \mathbf{a}(\phi, \theta) \right| \tag{2.30}$$

Array beampattern specifications are described with a number of parameters. A summary of these parameters and their definitions are as follows.

- **Mainlobe** is the region in the array beampattern without any null response around the steered to direction (ϕ, θ).

13

- **Null-to-null beamwidth** (ϕ_{NN}) is the width of the mainlobe measured between the null points in the left and right.

- Half of the null-to-null beamwidth $\frac{\phi_{NN}}{2}$ defines **Rayleigh resolution limit** which is the minimum angular distance for the separation of two sources with the classical DOA methods [32].

- **Half power beamwidth** (ϕ_{hp}) is the distance between cut-off points (ϕ_1, θ_1) and (ϕ_2, θ_1) whose powers are $B_{p,l}(\phi_1, \theta_1) = 0.5$ and $B_{p,l}(\phi_2, \theta_1) = 0.5$. This parameter is also known as **3 dB beamwidth**.

- **Peak-to-sidelobe level** is the peak difference between the mainlobe and nearest sidelobe to it.

- Null locations have an effect on the signal levels from the sources after the beamforming. If one of the nulls lies at the direction of target, the target cannot be seen from the peaks in the spatial spectra. Sidelobe levels also have an effect on the target peaks on the spatial spectra. Problem of grating lobe arises if there is a spatial aliasing in the array. **Grating lobes** have similar levels related to the mainlobe and causes false target detections at the spectra. Spatial aliasing is observed when $\omega_c \frac{d}{c} > \pi$ where d is the distance between two adjacent sensors. By using wavelength λ_c, this condition becomes,

$$\omega_c \frac{d}{c} > \pi$$
$$2\pi f_c \frac{d}{c} > \pi$$
$$\frac{2\pi}{\lambda_c} d > \pi$$
$$d > \frac{\lambda_c}{2} \tag{2.31}$$

This condition is also named as *spatial Nyquist theorem*. Beampattern parameters that are explained in here is shown on a beampattern of 10-element uniform line array in Figure 2.2. Inter-element distance of the array is chosen as λ_c which violates the spatial Nyquist theorem. Array is steered to $(90°, 90°)$ and weight vector is chosen as $\mathbf{w} = [1/10, 1/10, \cdots, 1/10]^{\mathrm{T}}$.
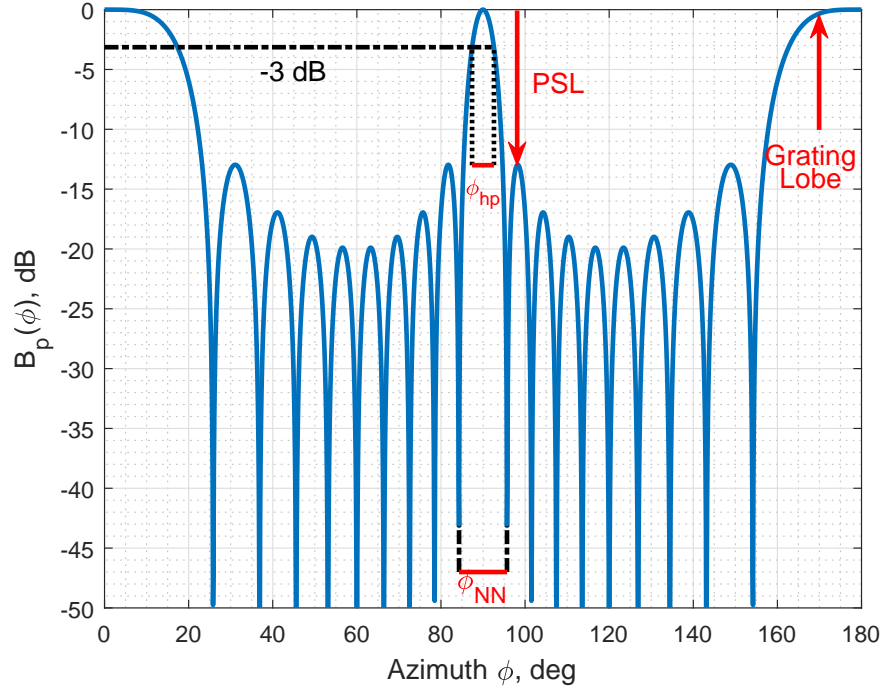
Figure 2.2: A Beampattern and Its Parameters

2.6 Array Performance Measures

Sensor arrays can be compared with each other using a number of different performance measures. Some of the performance parameters for beampatterns are given in Section 2.5. In addition to them, three main performance measures are given in this section. These measures are directivity, array gain and sensitivity.

2.6.1 Directivity and Directivity Index

One of the common parameters is directivity and denoted by D. It is the ratio of source signal power to the noise power at the array output [28]. Noise is assumed to be isotropic which means that it has a uniform distribution over a sphere. Directivity is calculated as

$$D = \frac{B_{p,l}(\phi_s, \theta_s)}{\frac{1}{4\pi} \int_0^\pi d\theta \int_0^{2\pi} d\phi \sin\theta B_{p,l}(\phi, \theta)} \tag{2.32}$$

where (ϕ_s, θ_s) is direction of the source signal. If sensor weight vector $\mathbf{w}$ is normalized to obtain $B_{p,l}(\phi_s, \theta_s) = 1$, 2.32 can be written as evident in [28, Eq. (2.145)],

15

$$D = \left(\frac{1}{4\pi} \int_0^\pi d\theta \int_0^{2\pi} d\phi \sin\theta B_{p,l}(\phi, \theta) \right)^{-1} \tag{2.33}$$

For a linear array, Equation 2.33 is further reduced to [28, Eq. (2.155)],

$$D = \left(\mathbf{w}^{\mathrm{H}} \mathbf{S} \mathbf{w} \right)^{-1} \tag{2.34}$$

where $\mathbf{S}$ is the sinc matrix. n^{th} row and m^{th} column element of the sinc matrix can be defined as,

$$\mathbf{S}_{nm} \triangleq \operatorname{sinc}\left(\frac{2\pi}{\lambda} p_{nm} \right) \tag{2.35}$$

where p_{nm} is the distance between n^{th} and m^{th} sensor. For a uniform line array whose inter-element distance is $\frac{\lambda}{2}$, 2.35 becomes,

$$D = \left(\mathbf{w}^{\mathrm{H}} \mathbf{w} \right)^{-1} = \left(\|\mathbf{w}\|^2 \right)^{-1} \tag{2.36}$$

Directivity D can also be converted to dB scale and it becomes *directivity index* (*DI*),

$$DI = 10 \log_{10} D \tag{2.37}$$

2.6.2 Array Gain

Main aim of using a sensor array is to increase the *signal to noise ratio* SNR by summing signals coherently and noise incoherently. This SNR improvement can be measured by *array gain*. It is one of the important array performance measures and denoted by A_w. Array gain can be defined as the ratio of output SNR to input SNR,

$$A_w = \frac{\mathrm{SNR}_{out}}{\mathrm{SNR}_{in}} \tag{2.38}$$

where SNR_{in} is the SNR of the signal received by the sensors and SNR_{out} is the SNR at the array output after beamforming. Array output can be written by applying sensor weights to the received signals which can be expressed with narrowband signal model in Equation 2.22,

$$z(t) = \mathbf{w}^{\mathrm{H}} \mathbf{y}(\mathbf{t}) \tag{2.39}$$

16

where $t = kT$, $k = \{0, 1, ..., N - 1\}$, T is the sampling period and N is the number of snapshots. Power of the array output signal can be found as,

$$
\begin{aligned}
P_{\mathbf{z}} &= \mathbf{E}\{z(t)z^{\mathrm{H}}(t)\} \\
&= \mathbf{E}\{\left(\mathbf{w}^{\mathrm{H}}\mathbf{y}(t)\right)\left(\mathbf{y}^{\mathrm{H}}(t)\mathbf{w}\right)\} \\
&= \mathbf{E}\{\left(\mathbf{w}^{\mathrm{H}}\left(\mathbf{a}(\phi, \theta)s(t) + \mathbf{e}(t)\right)\right)\left(\left(s^{\mathrm{H}}(t)\mathbf{a}^{\mathrm{H}}(\phi, \theta) + \mathbf{e}^{\mathrm{H}}(t)\right)\mathbf{w}\right)\} \\
&= \left(\mathbf{w}^{\mathrm{H}}\mathbf{a}(\phi, \theta)\mathbf{E}\{s(t)s^{\mathrm{H}}(t)\}\mathbf{a}^{\mathrm{H}}(\phi, \theta)\mathbf{w}\right) + \left(\mathbf{w}^{\mathrm{H}}\mathbf{a}(\phi, \theta)\mathbf{E}\{s(t)\mathbf{e}^{\mathrm{H}}(t)\}\mathbf{w}\right) \\
&\quad + \left(\mathbf{w}^{\mathrm{H}}\mathbf{E}\{\mathbf{e}(t)s^{\mathrm{H}}(t)\}\mathbf{a}^{\mathrm{H}}(\phi, \theta)\mathbf{w}\right) + \left(\mathbf{w}^{\mathrm{H}}\mathbf{E}\{\mathbf{e}(t)\mathbf{e}^{\mathrm{H}}(t)\}\mathbf{w}\right) \quad (2.40)
\end{aligned}
$$

According to the narrowband array signal model, noise signals in every sensor are uncorrelated with each other. In addition, source signal is modeled as random Gaussian process and its samples are uncorrelated with noise signal.

$$
\mathbf{E}\{s(t)s^{\mathrm{H}}(t)\} = \sigma_s^2 \tag{2.41}
$$

$$
\mathbf{E}\{\mathbf{e}(t)\mathbf{e}^{\mathrm{H}}(t)\} = \sigma_e^2 \mathbf{I_M} \tag{2.42}
$$

$$
\mathbf{E}\{s(t)\mathbf{e}^{\mathrm{H}}(t)\} = \mathbf{0_{1xM}} \tag{2.43}
$$

$$
\mathbf{E}\{\mathbf{e}(t)s^{\mathrm{H}}(t)\} = \mathbf{0_{Mx1}} \tag{2.44}
$$

where $\mathbf{I_M}$ is the identity matrix of dimension M x M , $\mathbf{0_{1xM}}$ is the vector of dimension 1 x M with all zero elements and $\mathbf{0_{Mx1}}$ is the vector of dimension M x 1 with all zero elements. By using 2.41, 2.42, 2.43 and 2.44, array output power in 2.40 can be written as,

$$
P_{\mathbf{z}} = \mathbf{w}^{\mathrm{H}}\mathbf{a}(\phi, \theta)\sigma_s^2 \mathbf{a}^{\mathrm{H}}(\phi, \theta)\mathbf{w} + \sigma_e^2 \mathbf{w}^{\mathrm{H}}\mathbf{I_M}\mathbf{w} \tag{2.45}
$$

By normalizing weight vector $\mathbf{w}$ such that $\mathbf{w}^{\mathrm{H}}\mathbf{a}(\phi, \theta) = 1$, 2.45 is reduced to,

$$
P_{\mathbf{z}} = \sigma_s^2 + \sigma_e^2 \mathbf{w}^{\mathrm{H}}\mathbf{w} \tag{2.46}
$$

SNR_{in} and SNR_{out} can be defined as,

$$
\mathrm{SNR}_{in} = \frac{\sigma_s^2}{\sigma_e^2} \tag{2.47}
$$

$$
\mathrm{SNR}_{out} = \frac{\sigma_s^2}{\sigma_e^2 \mathbf{w}^H \mathbf{w}} \tag{2.48}
$$

By using 2.47 and 2.48, array gain for spatially white noise can be expressed as,

$$
A_w = \frac{\mathrm{SNR}_{out}}{\mathrm{SNR}_{in}} = \frac{1}{\|\mathbf{w}\|^2} = \left(\|\mathbf{w}\|^2\right)^{-1} \tag{2.49}
$$

With respect to 2.49, array gain for spatially white noise is equal to the directivity for a uniform line array with $\lambda/2$ element spacing.

Sensitivity to gain, phase and sensor positioning errors is another important array performance measure. For small error variances and arbitrary array geometry, it is the inverse of the array gain for spatially white noise case [28, Eq. (2.209)]. It is denoted by T_{se}.

$$T_{se} = A_w^{-1} = \|\mathbf{w}\|^2 \tag{2.50}$$

CHAPTER 3

DIRECTION OF ARRIVAL ESTIMATION

Arrays of sensors are used for many different applications in sonar, radar, communication etc. Using an array of sensors has many advantages over using a single sensor. For instance, with appropriate signal processing, the signal to noise ratio of the incoming signal can be increased, and/or the direction of the incoming signal can be estimated. This estimation problem is known as *direction of arrival estimation (DOA)* where the parameter of interest is the direction of incoming signal(s). There is a vast literature on this subject [28] and many DOA methods. In this chapter we give a brief review of some of the most commonly used/referred DOA methods.

3.1 Beamforming

Beamforming can be defined as spatial filtering of signals by using a sensor array. Analogous to filtering of digital/analog signals, a spatial filtering operation can be achieved using sensor data with different delays. As we have explained in Chapter 2, the received signals in the sensor array are delayed versions of each other. And these delays are a known (or predictable) function of sensor positions and the direction of source signal. Since only the narrowband signal model is considered in this thesis, the main interest will be on the narrowband beamformer illustrated in Figure 3.1. The main idea of this signal processing structure, is to align (in time axis) the signal of interest received by different channels and coherently sum the resulting signals. With the white noise assumption, delayed noise signals will still be uncorrelated, hence they will be summed incoherently. The main objective is to exploit this processing gain obtained by the coherent sum of the desired signals over the incoherent summa-
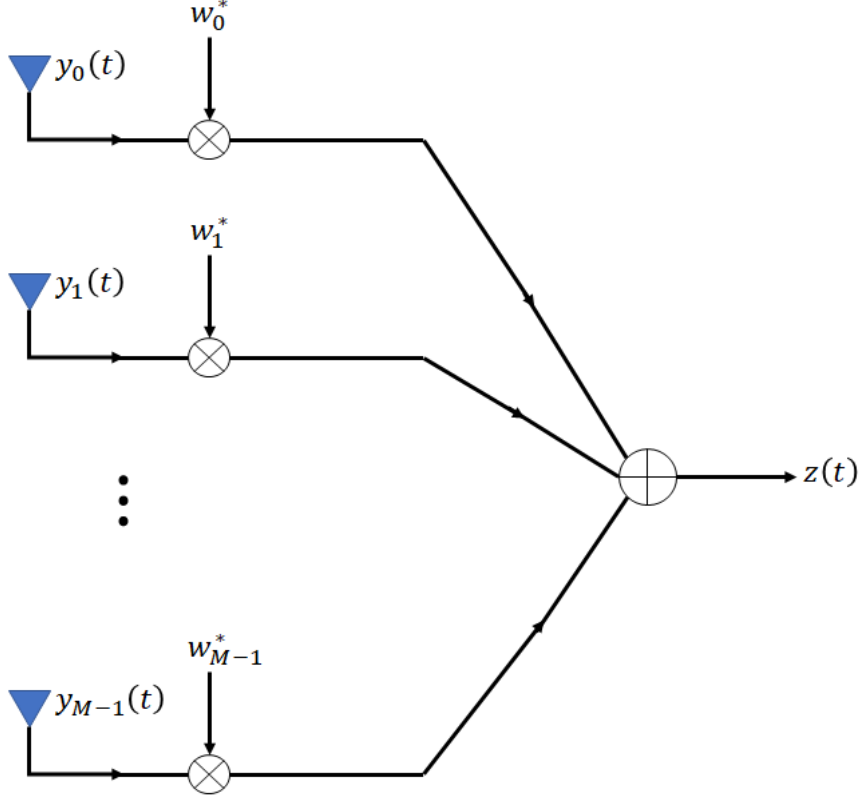
Figure 3.1: Time-domain narrowband beamformer

tion of noise signals. The delays and/or gains to be applied to each sensor channel can be represented by a complex number, $\{w_n\}_{n=1}^{M}$, which is the nth element of the weight vector $\mathbf{w}$. In mathematical form, elements of the sensor weight vector $\mathbf{w}$ are multiplied with the received channels and summed to steer the beam to desired direction,

$$z(t) = \sum_{n=0}^{M-1} w_n^* y_n(t) = \mathbf{w}^H \mathbf{y}(t) \tag{3.1}$$

where $t = kT$, $k = \{0, 1, ..., N-1\}$, T is the sampling period and N is the number of snapshots. Power of the beamformer output can be found by,

$$\begin{aligned}
P_{\mathbf{z}} &= \frac{1}{N} \sum_{k=0}^{N-1} |z(kT)|^2 \\
&= \frac{1}{N} \sum_{k=0}^{N-1} \mathbf{w}^H \mathbf{y}(kT) \mathbf{y}^H(kT) \mathbf{w} \\
&= \mathbf{w}^H \frac{1}{N} \left(\sum_{k=0}^{N-1} \mathbf{y}(kT) \mathbf{y}^H(kT) \right) \mathbf{w}
\end{aligned} \tag{3.2}$$

20

Different DOA methods require the knowledge of the exact covariance of the received signal vector $\mathbf{y}$, which is in general not available, hence needs to be estimated. The most common method to do so is to estimate it with the *sample covariance matrix* and denoted by $\hat{\mathbf{R}}_{\mathbf{y}}$ [4],

$$\hat{\mathbf{R}}_{\mathbf{y}} = \frac{1}{N}\sum_{k=0}^{N-1}\mathbf{y}(kT)\mathbf{y}^{\mathrm{H}}(kT) \tag{3.3}$$

In order sample covariance matrix to converge the exact covariance, we need a large number of snaphots (N). In practice this number is in general limited to much smaller values than desired. Note that the term in parentheses in (3.2) is the sample covariance matrix, hence we can simplify the output power to the following,

$$P_{\mathbf{z}} = \mathbf{w}^{\mathrm{H}}\hat{\mathbf{R}}_{\mathbf{y}}\mathbf{w} \tag{3.4}$$

3.2   DOA Estimation with Beamforming

One of the methods used for finding DOA angles of sources is forming a spatial spectrum with beamforming. Array is steered to one direction at a time by selecting the sensor weight vector $\mathbf{w}$ and the output power is recorded. Spatial power spectrum is found by repeating it for every angle of interest. Peak points represent the directions with maximum powers and they are classified as DOA estimates for the source signals. Spatial spectrum with beamforming can be written as,

$$P_{\mathbf{z}}\left(\phi,\theta\right) = \mathbf{w}^{\mathrm{H}}\left(\phi,\theta\right)\hat{\mathbf{R}}_{\mathbf{y}}\mathbf{w}\left(\phi,\theta\right) \tag{3.5}$$

where $(\phi,\theta) \in \{(\phi_1,\theta_1),\cdots,(\phi_L,\theta_L)\}$ is the steering direction, $\mathbf{w}\left(\phi,\theta\right)$ is the sensor weight vector used for *steering* the array to (ϕ,θ), $P_{\mathbf{z}}\left(\phi,\theta\right)$ is the beamformer output power for the direction (ϕ,θ) and L is the number of steering angle pairs.

Sensor weights can be selected to maximize *signal to interference and noise ratio* (SINR) by minimizing the output power due to the noise and interference signals. Before giving the SINR equation, narrowband array signal model is modified by adding the interference signal as follows,

$$\mathbf{y}(t) = \mathbf{a}(\phi_0,\theta_0)s_0(t) + \mathbf{a}(\phi_1,\theta_1)s_1(t) + \mathbf{e}(t) \tag{3.6}$$

21

where (ϕ_0, θ_0) is the direction of the desired signal, (ϕ_1, θ_1) is the direction of the interference signal, $s_0(t)$ is the desired signal and $s_1(t)$ is the interference signal. Equation 3.6 can be written as the summation of the desired source and interference-noise combination components,

$$\mathbf{y}(t) = \mathbf{s}(t) + \mathbf{n}(t) \tag{3.7}$$

where $\mathbf{s}(t) = \mathbf{a}(\phi_0, \theta_0)s_0(t)$ and $\mathbf{n}(t) = \mathbf{a}(\phi_1, \theta_1)s_1(t) + \mathbf{e}(t)$. Then, covariance matrices of the desired signal and interference-noise components can be written as,

$$\mathbf{R_s} = \mathbf{E}\{\mathbf{s}(t)\mathbf{s}^{\mathrm{H}}(t)\} \tag{3.8}$$

$$\mathbf{R_n} = \mathbf{E}\{\mathbf{n}(t)\mathbf{n}^{\mathrm{H}}(t)\} \tag{3.9}$$

After expressing the signal and noise-interference covariance matrices in 3.8 and 3.9, SINR is defined as,

$$\mathrm{SINR} = \frac{\mathbf{w}^{\mathrm{H}}\mathbf{R_s}\mathbf{w}}{\mathbf{w}^{\mathrm{H}}\mathbf{R_n}\mathbf{w}} \tag{3.10}$$

To pass the desired signal from the beamformer undistorted, sensor weight vector $\mathbf{w}$ is selected such as,

$$\mathbf{w}^{\mathrm{H}}\mathbf{R_s}\mathbf{w} = 1 \tag{3.11}$$

Equation 3.11 is valid for multiple number of source signals. If there is a single source, 3.11 is simplified as,

$$\mathbf{w}^{\mathrm{H}}\mathbf{a}(\phi_0, \theta_0) = 1 \tag{3.12}$$

where (ϕ_0, θ_0) is the DOA of the single source. Then, beamformer weight vector selection problem can be written as

$$
\begin{aligned}
\max_{\mathbf{w}} \quad & \frac{\mathbf{w}^{\mathrm{H}}\mathbf{R_s}\mathbf{w}}{\mathbf{w}^{\mathrm{H}}\mathbf{R_n}\mathbf{w}} \\
\text{subject to} \quad & \mathbf{w}^{\mathrm{H}}\mathbf{R_s}\mathbf{w} = 1
\end{aligned} \tag{3.13}
$$

By inserting the undistorted response constraint into the cost function, 3.13 becomes,

$$
\begin{aligned}
\min_{\mathbf{w}} \quad & \mathbf{w}^{\mathrm{H}}\mathbf{R_n}\mathbf{w} \\
\text{subject to} \quad & \mathbf{w}^{\mathrm{H}}\mathbf{R_s}\mathbf{w} = 1
\end{aligned} \tag{3.14}
$$

According to Equation 3.14, maximizing SINR is equal to minimizing the output power of noise and interference with the undistorted response constraint. Equation

3.14 is valid for multiple number of sources. For a single source case, this optimization problem can be rewritten by using the constraint in 3.12,

$$\min_{\mathbf{w}} \quad \mathbf{w}^{\mathrm{H}} \mathbf{R_n} \mathbf{w}$$
$$\text{subject to} \quad \mathbf{w}^{\mathrm{H}} \mathbf{a}(\phi_0, \theta_0) \;=\; 1 \tag{3.15}$$

where (ϕ_0, θ_0) is the steering direction. In Section 2.6, source and noise samples are assumed to be uncorrelated according to the narrowband array signal model. Interference signal can also be modeled as random Gaussian process and assumed to be uncorrelated with both desired signal and noise. In that case, correlations between desired signal, interference and noise can be written as,

$$\mathbf{R_s} = \mathbf{E}\{s(t)s^{\mathrm{H}}(t)\} = \sigma_s^2 \mathbf{a}(\phi_0, \theta_0)\mathbf{a}^{\mathrm{H}}(\phi_0, \theta_0) \tag{3.16}$$

$$\mathbf{R_i} = \mathbf{E}\{(\mathbf{a}(\phi_1, \theta_1)s_1(t))\,(\mathbf{a}(\phi_1, \theta_1)s_1(t))^{\mathrm{H}}\} = \sigma_i^2 \mathbf{a}(\phi_1, \theta_1)\mathbf{a}^{\mathrm{H}}(\phi_1, \theta_1) \tag{3.17}$$

$$\mathbf{R_e} = \mathbf{E}\{\mathbf{e}(t)\mathbf{e}^{\mathrm{H}}(t)\} = \sigma_e^2 \mathbf{I_M} \tag{3.18}$$

$$\mathbf{E}\{s_0(t)\mathbf{e}^{\mathrm{H}}(t)\} = \mathbf{0_{1xM}} \tag{3.19}$$

$$\mathbf{E}\{s_1(t)\mathbf{e}^{\mathrm{H}}(t)\} = \mathbf{0_{1xM}} \tag{3.20}$$

$$\mathbf{E}\{\mathbf{e}(t)s_0^*(t)\} = \mathbf{0_{Mx1}} \tag{3.21}$$

$$\mathbf{E}\{\mathbf{e}(t)s_1^*(t)\} = \mathbf{0_{Mx1}} \tag{3.22}$$

$$\mathbf{R_n} = \mathbf{E}\{\mathbf{n}(t)\mathbf{n}^{\mathrm{H}}(t)\} = \mathbf{R_i} + \mathbf{R_e} \tag{3.23}$$

where $\mathbf{I_M}$ is the identity matrix of dimension M x M , $\mathbf{0_{1xM}}$ is the vector of dimension 1 x M with all zero elements and $\mathbf{0_{Mx1}}$ is the vector of dimension M x 1 with all zero elements. With these equations, covariance matrix of the received signal vector $\mathbf{y}(t)$ can be written as,

$$\mathbf{R_y} = \mathbf{E}\{\mathbf{y}(t)\mathbf{y}^{\mathrm{H}}(t)\} = \mathbf{R_s} + \mathbf{R_n} \tag{3.24}$$

By using 3.24, power of the beamformer output can be expressed as

$$P_{\mathbf{z}}(\phi, \theta) = \mathbf{w}^{\mathrm{H}}(\phi, \theta)\,\mathbf{R_y}\mathbf{w}(\phi, \theta)$$
$$= \mathbf{w}^{\mathrm{H}}(\phi, \theta)\,(\mathbf{R_s} + \mathbf{R_n})\,\mathbf{w}(\phi, \theta)$$
$$= \mathbf{w}^{\mathrm{H}}(\phi, \theta)\,\mathbf{R_s}\mathbf{w}(\phi, \theta) + \mathbf{w}^{\mathrm{H}}(\phi, \theta)\,\mathbf{R_n}\mathbf{w}(\phi, \theta) \tag{3.25}$$

Since the output power of the desired signal component is fixed for undistorted response in Equation 3.11 and 3.12, beamformer weight selection problems in Equation

3.14 and 3.15 can also be defined as,

$$\min_{\mathbf{w}} \quad \mathbf{w}^{\mathrm{H}} \mathbf{R_y} \mathbf{w}$$
$$\text{subject to} \quad \mathbf{w}^{\mathrm{H}} \mathbf{R_s} \mathbf{w} \quad = \quad 1 \tag{3.26}$$

$$\min_{\mathbf{w}} \quad \mathbf{w}^{\mathrm{H}} \mathbf{R_y} \mathbf{w}$$
$$\text{subject to} \quad \mathbf{w}^{\mathrm{H}} \mathbf{a}(\phi_0, \theta_0) \quad = \quad 1 \tag{3.27}$$

Different beamformer weights can be found by changing the cost function or constraints. Two of these methods will be explained in the following two subsections.

3.2.1 Bartlett Beamformer

Bartlett beamformer is an application of Fourier based spectral analysis [3] to the array processing [4]. It is also known as *conventional beamformer*. Sensor weights in this beamformer have a closed form expression and its computational complexity is low. Due to these properties, it is one of the most widely used techniques in practice. Sensor weight calculation is independent of the sensor data. Therefore, it does not give statistically optimum weights. Despite of the non-optimum results, it is also a robust method against the misplacement of the nulls in the beampattern. Since it is a data independent method, optimization problem for Bartlett beamformer is written by replacing the covariance matrix $\mathbf{R_y}$ with identity matrix $\mathbf{I_M}$ in Equation 3.27,

$$\min_{\mathbf{w}} \quad \mathbf{w}^{\mathrm{H}} \mathbf{w}$$
$$\text{subject to} \quad \mathbf{w}^{\mathrm{H}} \mathbf{a}(\phi_0, \theta_0) \quad = \quad 1 \tag{3.28}$$

Solution of the optimization problem in 3.28 can be found using the Lagrange multiplier technique,

$$\mathcal{L} = \left(\mathbf{w}^{\mathrm{H}} \mathbf{w} \right) + \lambda \left(1 - \mathbf{w}^{\mathrm{H}} \mathbf{a}(\phi_0, \theta_0) \right) + \lambda^* \left(1 - \mathbf{w}^{\mathrm{T}} \mathbf{a}^*(\phi_0, \theta_0) \right)$$
$$\frac{\partial \mathcal{L}}{\partial \mathbf{w}^{\mathrm{H}}} = \mathbf{w} - \lambda \mathbf{a}(\phi_0, \theta_0) = 0$$
$$\mathbf{w}^{\mathrm{H}} = \lambda \mathbf{a}^{\mathrm{H}}(\phi_0, \theta_0)$$
$$\mathbf{w}^{\mathrm{H}} \mathbf{a}(\phi_0, \theta_0) = \lambda \mathbf{a}^{\mathrm{H}}(\phi_0, \theta_0) \mathbf{a}(\phi_0, \theta_0) \tag{3.29}$$

Note that $\mathbf{w}^H \mathbf{a}(\phi_0, \theta_0) = 1$ as optimization constraint dictates.

$$\lambda = \frac{1}{\mathbf{a}^H(\phi_0, \theta_0)\mathbf{a}(\phi_0, \theta_0)}$$
$$\mathbf{w} = \frac{\mathbf{a}(\phi_0, \theta_0)}{\mathbf{a}^H(\phi_0, \theta_0)\mathbf{a}(\phi_0, \theta_0)} = \frac{\mathbf{a}(\phi_0, \theta_0)}{M} \tag{3.30}$$

Solution of the optimization problem in Equation 3.28 is the array manifold vector that is scaled by the number of sensors M. Spatial power spectrum for Bartlett beamformer can be found by putting 3.28 into 3.5,

$$P_{\mathbf{z}}(\phi, \theta) = \frac{\mathbf{a}^H(\phi, \theta)\,\hat{\mathbf{R}}_{\mathbf{y}}\mathbf{a}(\phi, \theta)}{M^2} \tag{3.31}$$

where $(\phi, \theta) \in \{(\phi_1, \theta_1), \cdots, (\phi_L, \theta_L)\}$ is the steering direction, $P_{\mathbf{z}}(\phi, \theta)$ is the power of the beamformer output for the direction (ϕ, θ), $\hat{\mathbf{R}}_{\mathbf{y}}$ is the sample covariance matrix which is calculated from the available received data snapshots, L is the number of steering angle pair and M is the number of sensors.

3.2.2 Capon Beamformer

Capon beamformer [5] is an adaptive beamforming technique. Adaptive beamformers update their solution for a minimization problem using estimated parameters from the most recent array data. In Capon beamformer, minimization of output power is aimed while having a unity gain in the steering direction (ϕ, θ). Optimization problem for Capon beamformer is as follows,

$$\begin{aligned} \min_{\mathbf{w}} \quad & \mathbf{w}^H \mathbf{R}_{\mathbf{y}} \mathbf{w} \\ \text{subject to} \quad & \mathbf{w}^H \mathbf{R}_{\mathbf{s}} \mathbf{w} = 1 \end{aligned} \tag{3.32}$$

MVDR (minimum variance distortionless) beamformer is another adaptive technique used in the beamforming. Minimization of output power due to noise and interference is aimed while having a unity gain in the steering direction (ϕ, θ). In [33], optimization problem for MVDR beamformer is written as,

$$\begin{aligned} \min_{\mathbf{w}} \quad & \mathbf{w}^H \mathbf{R}_{\mathbf{n}} \mathbf{w} \\ \text{subject to} \quad & \mathbf{w}^H \mathbf{R}_{\mathbf{s}} \mathbf{w} = 1 \end{aligned} \tag{3.33}$$

Since source and noise samples are uncorrelated in the array signal model, minimization of the array output power means minimization of the output power of noise and

interference as it is shown in Equation 3.25. Therefore, both optimization problems in 3.32 and 3.33 give the same result. Solution of the optimization problem in 3.32 can be found using the Lagrange multiplier technique,

$$\mathcal{L} = \left(\mathbf{w}^H \mathbf{R_y} \mathbf{w}\right) + \lambda \left(1 - \mathbf{w}^H \mathbf{R_s} \mathbf{w}\right) + \lambda^* \left(1 - \mathbf{w}^T \mathbf{R_s} \mathbf{w}^*\right)$$

$$\frac{\partial \mathcal{L}}{\partial \mathbf{w}^H} = \mathbf{R_y} \mathbf{w} - \lambda \mathbf{R_s} \mathbf{w} = 0$$

$$\mathbf{R_s} \mathbf{w} = \frac{1}{\lambda} \mathbf{R_y} \mathbf{w}$$

$$\mathbf{R_y}^{-1} \mathbf{R_s} \mathbf{w} = \frac{1}{\lambda} \mathbf{w} \tag{3.34}$$

Equation 3.34 is a generalized eigenvalue problem [34]. Solution of this problem is the eigenvector corresponding to the maximum eigenvalue of $\mathbf{R_y}^{-1} \mathbf{R_s}$. For a single source scenario, Capon optimization problem can be written by changing the constraint of 3.32,

$$\min_{\mathbf{w}} \quad \mathbf{w}^H \mathbf{R_y} \mathbf{w}$$
$$\text{subject to} \quad \mathbf{w}^H \mathbf{a}(\phi_0, \theta_0) = 1 \tag{3.35}$$

Solution of the optimization problem in 3.35 can also be found using the Lagrange multiplier technique,

$$\mathcal{L} = \left(\mathbf{w}^H \mathbf{R_y} \mathbf{w}\right) + \lambda \left(1 - \mathbf{w}^H \mathbf{a}(\phi_0, \theta_0)\right) + \lambda^* \left(1 - \mathbf{w}^T \mathbf{a}^*(\phi_0, \theta_0)\right)$$

$$\frac{\partial \mathcal{L}}{\partial \mathbf{w}^H} = \mathbf{R_y} \mathbf{w} - \lambda \mathbf{a}(\phi_0, \theta_0) = 0$$

$$\mathbf{R_y} \mathbf{w} = \lambda \mathbf{a}(\phi_0, \theta_0)$$

$$\mathbf{w} = \lambda \mathbf{R_y}^{-1} \mathbf{a}(\phi_0, \theta_0)$$

$$1 = \mathbf{w}^H \mathbf{a}(\phi_0, \theta_0)$$

$$1 = \lambda \mathbf{a}^H(\phi_0, \theta_0) \mathbf{R_y}^{-1} \mathbf{a}(\phi_0, \theta_0)$$

$$\lambda = \frac{1}{\mathbf{a}^H(\phi_0, \theta_0) \mathbf{R_y}^{-1} \mathbf{a}(\phi_0, \theta_0)}$$

$$\mathbf{w} = \frac{\mathbf{R_y}^{-1} \mathbf{a}(\phi_0, \theta_0)}{\mathbf{a}^H(\phi_0, \theta_0) \mathbf{R_y}^{-1} \mathbf{a}(\phi_0, \theta_0)} \tag{3.36}$$

Spatial power spectrum for Capon beamformer can be found by putting 3.36 into 3.5,

$$P_{\mathbf{z}}(\phi, \theta) = \frac{1}{\mathbf{a}^H(\phi, \theta) \mathbf{R_y}^{-1} \mathbf{a}(\phi, \theta)} \tag{3.37}$$

where $(\phi, \theta) \in \{(\phi_1, \theta_1), \cdots, (\phi_L, \theta_L)\}$ is the steering direction, $P_{\mathbf{z}}(\phi, \theta)$ is the power of the beamformer output for the direction (ϕ, θ), $\hat{\mathbf{R}}_{\mathbf{y}}$ is the sample covariance matrix

which is calculated from the available received data snapshots and L is the number of steering angle pair. Since covariance matrices $\mathbf{R_y}$, $\mathbf{R_s}$ and $\mathbf{R_n}$ are not available in practice, sample covariance matrix $\hat{\mathbf{R}}_\mathbf{y}$ is used for sensor weight calculation. This technique is known as *SMI (sample matrix inverse) beamformer.* Using sample co-variance matrix, 3.36 and 3.37 becomes,

$$\mathbf{w} = \frac{\hat{\mathbf{R}}_\mathbf{y}^{-1}\mathbf{a}(\phi_0,\theta_0)}{\mathbf{a}^{\mathrm{H}}(\phi_0,\theta_0)\hat{\mathbf{R}}_\mathbf{y}^{-1}\mathbf{a}(\phi_0,\theta_0)} \tag{3.38}$$

$$P_\mathbf{z}(\phi,\theta) = \frac{1}{\mathbf{a}^{H}(\phi,\theta)\,\hat{\mathbf{R}}_\mathbf{y}^{-1}\mathbf{a}(\phi,\theta)} \tag{3.39}$$

3.3 DOA Estimation with Subspace Based Methods

Another method for finding DOA angles of sources is forming a spatial spectrum with subspace methods. Most distinctive advantage of subspace techniques over the classical DOA methods is observed when there are more than two sources. Classical methods can resolve two targets which are separated by half of the null-to-null beamwidth. This limit was defined as Rayleigh resolution limit in Section 2.5. Subspace based methods are able to perform beyond this limit, and thus, they are called super-resolution methods [35].

3.3.1 MUSIC

MUSIC (MUltiple SIgnal Classification) is probably the most well known subspace technique used in DOA estimation [11]. This method divides the signal subspace and noise subspace using the covariance matrix and orthogonality assumptions. Covariance matrix of the received signal model in 2.23 can be written as,

$$\begin{aligned}\mathbf{R_y} &= \mathbf{E}\{\mathbf{y}(t)\mathbf{y}^{\mathrm{H}}(t)\} \\ &= \mathbf{A}\mathbf{E}\{\mathbf{S}\mathbf{S}^{\mathrm{H}}\}\mathbf{A}^{\mathrm{H}} + \mathbf{R_e} \\ &= \mathbf{A}\mathbf{C}\mathbf{A}^{\mathrm{H}} + \sigma_e^2\mathbf{I}\end{aligned} \tag{3.40}$$

where $\mathbf{A} = [\mathbf{a}(\phi_1,\theta_1),\mathbf{a}(\phi_2,\theta_2),\cdots,\mathbf{a}(\phi_{P-1},\theta_{P-1})]$ is the array manifold matrix, $\mathbf{C}$ is the source covariance matrix, σ_e^2 is the noise variance and P is the number of

sources. Manifold matrix $\mathbf{A}$ is assumed to have full rank if the array is unambiguous [4]. Number of sensors M should be greater than number of sources P for $\mathbf{A}$ having full column rank. $\mathbf{C}$ is of rank P when the sources are uncorrelated and number of snapshots N is larger than number of sensors M. Then, $\mathbf{ACA}^H$ has rank P. Eigenvectors and eigenvalues of the covariance matrix in 3.40 can be found with eigendecomposition,

$$\mathbf{R_y} = \mathbf{U\Sigma U^H} \tag{3.41}$$

where $\mathbf{\Sigma} = diag\{\lambda_1, \cdots, \lambda_M\}$ is the diagonal matrix with positive eigenvalues in a descending order. There are $M - P$ linearly independent eigenvectors with eigenvalues $(\lambda_{P+1} = \cdots = \lambda_M = \sigma_e^2)$ and these eigenvectors form *noise subspace* $\mathbf{U}_N$. Remaining P eigenvectors are also linearly independent and form *signal subspace* $\mathbf{U}_S$ with corresponding eigenvalues $(\lambda_1 \geq \cdots \geq \lambda_P > \sigma_e^2)$. Note that columns of noise subspace $\mathbf{U}_N$ is orthogonal to manifold matrix $\mathbf{A}$. This can be shown as,

$$\mathbf{R_y U}_N = \sigma_e^2 \mathbf{IU}_N$$

$$\mathbf{ACA^H U}_N + \sigma_e^2 \mathbf{U}_N = \sigma_e^2 \mathbf{U}_N$$

$$\mathbf{ACA^H U}_N = \mathbf{0_{Mx(M-P)}}$$

$$\mathbf{A^H U}_N = \mathbf{0_{Mx(M-P)}} \tag{3.42}$$

Range space spanned by array manifold matrix $\mathbf{A}$ is the same with the range space spanned by the source subspace $\mathbf{U}_S$ since $\mathbf{C}$ has full rank [4]. Therefore, eigendecomposition of covariance matrix in Equation 3.41 can be written as,

$$\mathbf{R_y} = \mathbf{U}_S \mathbf{\Sigma}_S \mathbf{U}_S^H + \mathbf{U}_N \mathbf{\Sigma}_N \mathbf{U}_N^H \tag{3.43}$$

where $\mathbf{\Sigma}_S = diag\{\lambda_1, \cdots, \lambda_P\}$ and $\mathbf{\Sigma}_N = diag\{\lambda_{P+1}, \cdots, \lambda_M\}$. By using the orthogonality between manifold matrix and noise subspace, DOA angles of the sources can be found by solving $\mathbf{a}^H(\phi, \theta) \mathbf{U}_N \mathbf{U}_N^H \mathbf{a}(\phi, \theta) = 0$. True DOA angles can be estimated from spatial MUSIC power spectrum that is calculated as,

$$P_{\mathbf{MUSIC}}(\phi, \theta) = \frac{1}{\mathbf{a}^H(\phi, \theta) \mathbf{U}_N \mathbf{U}_N^H \mathbf{a}(\phi, \theta)} \tag{3.44}$$

where $(\phi, \theta) \in \{(\phi_1, \theta_1), \cdots, (\phi_L, \theta_L)\}$ is the steering direction and L is the number of steering angle pair. Since covariance matrix $\mathbf{R_y}$ is not available in practice, sample covariance matrix $\hat{\mathbf{R}}_\mathbf{y}$ should be used for finding the noise subspace. MUSIC algorithm for DOA estimation is summarized in Algorithm 1. MUSIC is a statistically

28
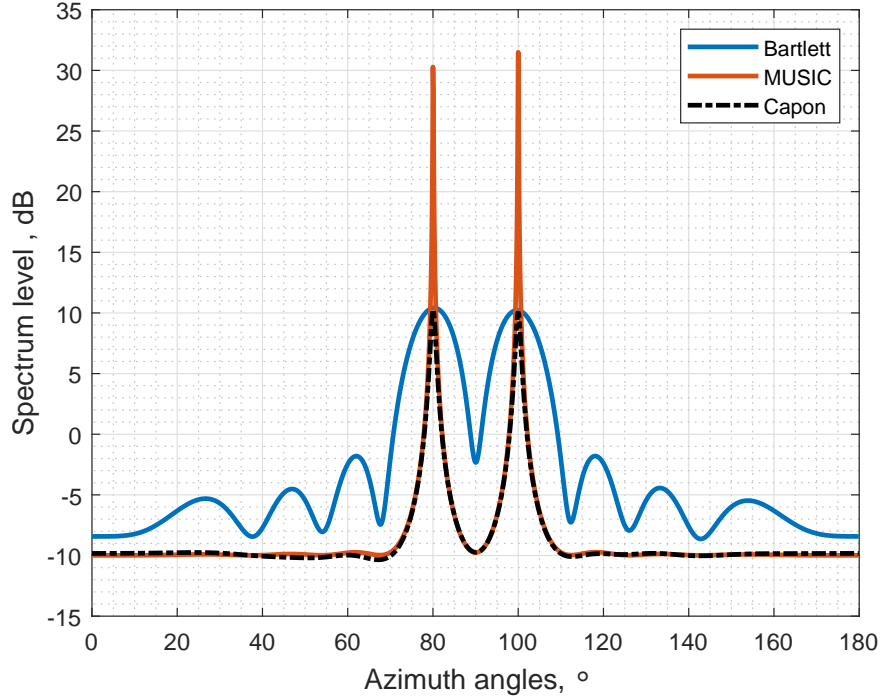
Figure 3.2: Spatial spectra using Bartlett, Capon and MUSIC methods on a *M = 10* element ULA with *N = 1000*, *P = 2*, *SNR = 10 dB*

efficient and consistent estimator [4]. Its performance attains Cramer-Rao Bound (CRB) and it estimates true value as the number of snapshots *N* goes to infinity. For coherent sources, this method does not work unless spatial smoothing is applied on the sample covariance matrix $\hat{\mathbf{R}}_{\mathbf{y}}$ [4].

An example of spatial spectra for Bartlett, Capon and MUSIC methods are illustrated in Figure 3.2. A uniform line array with $\lambda/2$ spacing and *M = 10* elements is used and the spatial spectrum is generated by using *N = 1000* snapshots. There are *P = 2* narrowband sources with SNR = *10 dB* and DOA angles of them are $\{80°, 100°\}$. Peaks in Capon and MUSIC spectrum is much sharper than the ones in Bartlett spectrum which results in better target separation for Capon and MUSIC techniques. Peak levels in Bartlett and Capon spectrum show true source levels at the sensor input, whereas peak levels at the MUSIC spectrum are greater. By using a covariance matrix that is calculated with infinite snapshots, peaks in the MUSIC spectrum tend to infinity since the manifold vectors corresponding to source DOA angles are orthogonal to noise space. Despite of performing beyond the Rayleigh limit, Capon and MUSIC methods suffer from coherent sources and cannot separate sources in that

Algorithm 1 MUSIC Algorithm

1: Compute manifold matrix for the array

$$\mathbf{A} = [\mathbf{a}(\phi_1), \cdots, \mathbf{a}(\phi_L)]$$

2: Compute sample covariance matrix

$$\hat{\mathbf{R}}_{\mathbf{y}} = \sum_{k=0}^{N-1} \mathbf{y}(kT)\mathbf{y}^{\mathrm{H}}(kT)$$

3: Perform eigendecomposition

$$\mathbf{R}_{\mathbf{y}} = \mathbf{U}\boldsymbol{\Sigma}\mathbf{U}^{\mathrm{H}}$$

4: Construct noise subspace matrix by choosing the eigenvectors belonging to the smallest M-P eigenvalues

$$\boldsymbol{\Sigma}_N = diag\{\lambda_{P+1}, \cdots, \lambda_M\}$$
$$\mathbf{U}_N = [\mathbf{u}_{P+1}, \cdots, \mathbf{u}_M]$$

5: **for** $(\phi, \theta) = \{(\phi_1, \theta_1), \cdots, (\phi_L, \theta_L)\}$ **do**

6:     Compute spatial spectrum for direction (ϕ, θ)

$$P_{\mathbf{MUSIC}}(\phi, \theta) = \frac{1}{\mathbf{a}^{\mathrm{H}}(\phi,\theta)\mathbf{U}_N\mathbf{U}_N^{\mathrm{H}}\mathbf{a}(\phi,\theta)}$$

7: **end for**

8: Find the DOA angle estimates by finding P highest peaks in the spectrum

---

case. This is also valid for Bartlett method. To solve the coherent source problem, spatial smoothing method is applied onto the sensor data before using DOA estimation methods. Details of spatial smoothing is given in Section 3.5

3.4 DOA Estimation with Dual Apodization

Beamwidth and PSL of an array (using Bartlett beamformer) are inversely proportional to each other. Advantages of narrow beamwidth and low PSL can be brought together by using dual apodization method. In [9], concept of nonlinear apodization is proposed to control the sidelobe levels for frequency estimation. It generates a spectrum by selecting the minimum of outputs of the multiple windows. There is a duality between DFT operation and beamforming for linear arrays. By using this idea, dual apodization technique is applied on the sensor arrays in [10]. In order to apply this method, two different subarrays are selected and Bartlett beamformer weights are

used as the sensor weights. Then,

$$w_{S1,k}\left(\phi\right) = e^{j\frac{2\pi}{\lambda}d_{S1,k}\cos(\phi)} \quad k = 1,\cdots,M_{S1}$$

$$w_{S2,k}\left(\phi\right) = e^{j\frac{2\pi}{\lambda}d_{S2,k}\cos(\phi)} \quad k = 1,\cdots,M_{S2}$$

$$\mathbf{w}_{S1}\left(\phi\right) = \left[w_{S1,1}\left(\phi\right),\cdots,w_{S1,M_{S1}}\left(\phi\right)\right]^{\mathrm{T}} \tag{3.45}$$

$$\mathbf{w}_{S2}\left(\phi\right) = \left[w_{S2,1}\left(\phi\right),\cdots,w_{S2,M_{S2}}\left(\phi\right)\right]^{\mathrm{T}} \tag{3.46}$$

where ϕ is the steering direction, $w_{S1,k}\left(\phi\right)$ is the weight for k^{th} sensor in the subarray-1, $w_{S2,k}\left(\phi\right)$ is the weight for k^{th} sensor in the subarray-2, $\mathbf{w}_{S1}\left(\phi\right)$ is the weight vector for the subarray-1, $\mathbf{w}_{S2}\left(\phi\right)$ is the weight vector for the subarray-2, M_{S1} is the number of sensors in the subarray-1 and M_{S2} is the number of sensors in the subarray-2. After calculating the weight vectors for both subarrays, spatial spectrums are generated as

$$P_{\mathbf{S1}}\left(\phi\right) = \mathbf{w}_{S1}^{\mathrm{H}}\left(\phi\right)\hat{\mathbf{R}}_{\mathbf{y}}\mathbf{w}_{S1}\left(\phi\right) \quad \phi = 0°,\cdots,\phi_L \tag{3.47}$$

$$P_{\mathbf{S2}}\left(\phi\right) = \mathbf{w}_{S2}^{\mathrm{H}}\left(\phi\right)\hat{\mathbf{R}}_{\mathbf{y}}\mathbf{w}_{S2}\left(\phi\right) \quad \phi = 0°,\cdots,\phi_L \tag{3.48}$$

where $\hat{\mathbf{R}}_{\mathbf{y}}$ is the sample covariance matrix, ϕ_L is the upper limit for the steering angle, $P_{\mathbf{S1}}\left(\phi\right)$ and $P_{\mathbf{S2}}\left(\phi\right)$ are the spatial spectrums of subarray-1 and subarray-2. Output of the dual apodization spectrum is found by selecting the minimum value for each angle.

$$P_{\mathbf{DA}}\left(\phi\right) = \min\left\{P_{\mathbf{S1}}\left(\phi\right),P_{\mathbf{S2}}\left(\phi\right)\right\} \quad \phi = 0°,\cdots,\phi_L \tag{3.49}$$

3.5 Spatial Smoothing

Signals have many reflections from physical objects in the environment. In addition to these multipath components, interference signals can be transmitted for jamming purposes. Multipath and jamming signals are coherent which causes a rank deficiency in the source covariance matrix $\mathbf{C}$. As a result, eigenvector corresponding to coherent source is a column vector in the noise subspace $\mathbf{U}_N$ instead of signal subspace $\mathbf{U}_S$. Then, $\mathbf{U}_N^{\mathrm{H}}\mathbf{a}\left(\phi,\theta\right) \neq \mathbf{0}$ and MUSIC algorithm will fail. In general, targets close to each other will not be separated in case of high correlation for the DOA estimation methods presented in this chapter. To restore the rank deficiency problem in the source covariance matrix, spatial smoothing method is proposed in [36] for DOA estimation problem. In this method, uniform line array is divided into some overlapping

subarrays. Since these subarrays are identical, manifold vectors of them can also be assumed to be identical. This method is based on averaging covariance matrices of all subarrays. Coherent signals are decorrelated with the random phase modulation due to the averaging process [4]. Spatially smoothed covariance matrix can be calculated as

$$\tilde{\mathbf{R}}_{\mathbf{y}} = \frac{1}{K} \sum_{k=1}^{K} \mathbf{Z_k} \mathbf{R_y} \mathbf{Z_k}^{\mathrm{T}} \tag{3.50}$$

where $\mathbf{Z_k} = \begin{bmatrix} \mathbf{0_{Lx(k-1)}} & \mathbf{I_L} & \mathbf{0_{Lx(M-L-k+1)}} \end{bmatrix}$, L is the number of sensors in the subarray, M is the number of sensors in the array and $K = M - L + 1$ is the number of subarrays. Rank of the spatially smoothed covariance matrix $\tilde{\mathbf{R}}_{\mathbf{y}}$ increases by $K - 1$ with K subarray until $\tilde{\mathbf{R}}_{\mathbf{y}}$ becomes full rank [37]. Main disadvantage of spatial smoothing technique is decreased aperture size since the aperture of the subarray is smaller than the aperture of the original array. Despite of this problem, it solves the coherent source problem for subspace based DOA estimators which requires less computations than the parametric DOA estimators such as deterministic maximum likelihood (DML) and stochastic maximum likelihood (SML). Spatial smoothing can only be applied on translational invariant arrays such as uniform line or uniform rectangular arrays. For other arrays, some transformation on the sensor data should be made in order to use spatial smoothing. In terms of the parameters, spatial smoothing requires

$$M \geq 2P \tag{3.51}$$

$$L > P \tag{3.52}$$

$$K \geq P \tag{3.53}$$

CHAPTER 4

DOA ESTIMATION WITH DIFFERENCE COARRAY

With classical DOA estimation methods (Bartlett beamformer, MVDR beamformer and MUSIC) presented in Chapter 3 the maximum number of resolvable sources is *M-1*, where *M* is the number of sensors. Hence with these methods the degree of freedom (DOF) of an *M* element array is *M*. Sparse linear arrays were proposed with coarray processing algorithms to overcome this limitation. It is possible to reach $O\left(M^2\right)$ DOF with $O\left(M\right)$ sensors with second-order statistics. By using the data obtained from real sensors, sensor signals of a virtual array with an increased DOF can be obtained.

In this chapter, concept of difference coarray will be explained with related parameters and sparse array types that are mainly used in difference coarray processing. In addition, spatially smoothed MVDR (SS MVDR) beamformer and spatially smoothed MUSIC (SS MUSIC) methods will be given as coarray DOA estimation methods.

4.1 Coarray Parameters

Sensor locations in a linear array can be defined as integer multiples of half wavelength of the narrowband sources such that $\mathbb{S} \triangleq \{n\lambda/2 \mid n \in \mathbb{Z}\}$. Sensor array will be denoted by the integer set $\mathbb{S}$ throughout this chapter. As an example, sensor positions of a uniform linear array of 5 sensors with $\lambda/2$ spacing can be represented with $\mathbb{S} = \{0, 1, 2, 3, 4\}$. In this section, most common parameters for difference coarrays will be given.

4.1.1 Difference Coarray

Difference coarray of the array $\mathbb{S}$ is denoted by $\mathbb{D}$ and can be defined as

$$\mathbb{D} \triangleq \{n_1 - n_2 \mid n_1, n_2 \in \mathbb{S}\} \tag{4.1}$$

Difference coarray set $\mathbb{D}$ in 4.1 includes only unique values of sensor position differences $n_1 - n_2$. Virtual sensor positions given by $\mathbb{D}$ are used in coarray DOA estimation methods. As an example, difference coarray of a uniform linear array with 5 sensors can be shown as $\mathbb{D} = \{-4, -3, -2, -1, 0, 1, 2, 3, 4\}$.

4.1.2 Weight Function

Weight function gives the number of occurrences of same position difference for a given difference coarray $\mathbb{D}$. Weight function of array $\mathbb{S}$ can be defined as

$$w[m] \triangleq \left| \{(n_1, n_2) \in \mathbb{S}^2 \mid n_1 - n_2 = m, \quad m \in \mathbb{D}\} \right| \tag{4.2}$$

Weight function of difference coarray $\mathbb{D}$ can be computed as autocorrelation of function $c[m]$ which can be defined as

$$c[m] = \begin{cases} 1 & \text{if there is a sensor at } m\lambda/2 \\ 0 & \text{otherwise} \end{cases} \tag{4.3}$$

$$w[m] = c[m] \circledast c[-m] \tag{4.4}$$

where $\circledast$ is the convolution operator. In [16], properties of weight function for an M sensor array are listed as

1. $w[0] = M$

2. $1 \leq w[m] \leq M - 1 \quad \forall m \in \mathbb{D} \setminus \{0\}$

3. $w[m] = w[-m] \quad \forall m \in \mathbb{D}$

4. $\sum_{m \in \mathbb{D} \setminus \{0\}} w[m] = M(M-1)$

As an example, weight function of a uniform linear array with 5 sensors can be shown as $w[0] = 5$, $w[\pm 1] = 4$, $w[\pm 2] = 3$, $w[\pm 3] = 2$, $w[\pm 4] = 1$.

34

4.1.3 Coarray Holes

Value of the weight function at any lag may not be a positive integer. For an M element array, largest value in $\mathbb{D}$ is $M - 1$. Holes are the set of numbers which are the zero weight lag values of $\mathbb{D}$ and can take value between $-M + 2$ and $M + 2$. Holes of an coarray can be defined as

$$\mathbb{H} \triangleq \{n \mid w[n] = 0, \quad -M + 1 < n < M - 1\} \tag{4.5}$$

4.1.4 Central ULA Segment

Central ULA segment of the array $\mathbb{S}$ is the largest subset of $\mathbb{D}$ such that there are no holes in it. It can be defined as

$$\mathbb{U} \triangleq \{0, \pm 1, \cdots, \pm m \mid m \in \mathbb{D}\} \tag{4.6}$$

where m is the largest consecutive integer in $\mathbb{D}$. Target separation performance of coarray DOA estimators such as SS MUSIC is limited by central ULA segment since aperture of the virtual array depends on it [16]. When there is no hole in $\mathbb{D}$, $\mathbb{U} = \mathbb{D}$. This is the case for ULA since $|\mathbb{H}| = 0$ where $|\mathbb{H}|$ is the cardinality of $\mathbb{H}$. In our case, cardinality operator $|.|$ gives the number of elements in $\mathbb{H}$.

4.1.5 Redundancy

Redundancy of the array $\mathbb{S}$ is a measure of central ULA segment $\mathbb{U}$ with respect to the number of sensors M. In [13], redundancy is defined as

$$R \triangleq \frac{M(M-1)}{|\mathbb{U}| - 1} \tag{4.7}$$

where $|\mathbb{U}|$ is the number of integers in central ULA segment $\mathbb{U}$ (cardinality of $\mathbb{U}$). ULA is the maximum redundancy array configuration for a fixed sensor number.

4.1.6 Fragility

Fragility is a measure of robustness of difference coarray against broken sensors [15]. If the sensor at n in $\mathbb{S}$ is broken and the difference coarray $\mathbb{D}$ does not change, it

is called an *inessential* sensor. Otherwise, it can be named as an *essential* sensor. In [15], fragility is defined as

$$F \triangleq \frac{M_{essential}}{M} \tag{4.8}$$

where M is the number of sensors and $M_{essential}$ is the number of essential sensors in the array $\mathbb{S}$. Fragility of an array can take values between $2/M$ and 1 for $M \geq 4$. Minimum fragility value $2/M$ is obtained for ULA and maximum fragility value 1 is obtained for minimum redundancy arrays (MRA), minimum hole arrays (MHA) and nested arrays [15]. Robustness of an array against sensor failure increases as the fragility value decreases.

4.2 Sparse Linear Array Types for Coarray DOA Estimation

Number of detectable sources for an array depends on the size of the difference coarray and central ULA segment. Main target for designing a sparse linear array with coarray methods is to obtain $\mathbb{D}$ or $\mathbb{U}$ which have larger number of elements with desired number of real sensors. There are many different sparse array configurations which are available in the literature. Among those solutions, perfect array, non-redundant array, nested array, minimum redundancy array and robust minimum redundancy array will be explained in this section.

4.2.1 Perfect Array

Perfect array is the most efficient array type in terms of spatial sampling. There is no hole in its difference coarray and $\mathbb{D} = \mathbb{U}$ is obtained. Its weight function satisfies

$$w[m] = 1 \quad \forall m \in \mathbb{D} \setminus \{0\} \tag{4.9}$$

Because of having unity value in its weight function except for $m = 0$, perfect array has the largest aperture among other types of sparse arrays without having a hole in its difference coarray. Despite having redundancy value of 1, perfect array exists for $M \leq 4$ [13]. As an example, array geometry of 4-sensor perfect array, non-negative part of its difference coarray and its weight function values corresponding to non-negative lags are shown in Figure 4.1.

Figure 4.1: Sensor locations, non-negative part of the difference coarray and weight function values corresponding to non-negative lags for perfect array with $M = 4, \mathbb{D} = \{0, \pm 1, \cdots, \pm 6\}$, $\mathbb{U} = \{0, \pm 1, \cdots, \pm 6\}$, $R = 1$, $F = 1$

4.2.2 Minimum Hole Array

Another type of efficient sparse linear array is minimum hole array (MHA) which is also called non-redundant array, Golomb array or minimum gap array [14]. Some holes exist in its difference coarray $\mathbb{D}$ when its weight function satisfies

$$w[m] \leq 1 \quad \forall m \in \mathbb{D} \setminus \{0\} \tag{4.10}$$

Main aim of using a MHA is to obtain minimum number of holes and distinct lag values in the difference coarray. Since it is a partially augmentable array, maximum number of detectable sources is limited by $|\mathbb{U}|$ with DOA estimation methods used for fully augmentable arrays [38]. Array configurations of MHA for $M \leq 4$ is the same with perfect arrays. As an example, array geometry of 6-sensor MHA, non-negative part of its difference coarray and its weight function values corresponding to non-negative lags are shown in Figure 4.2.
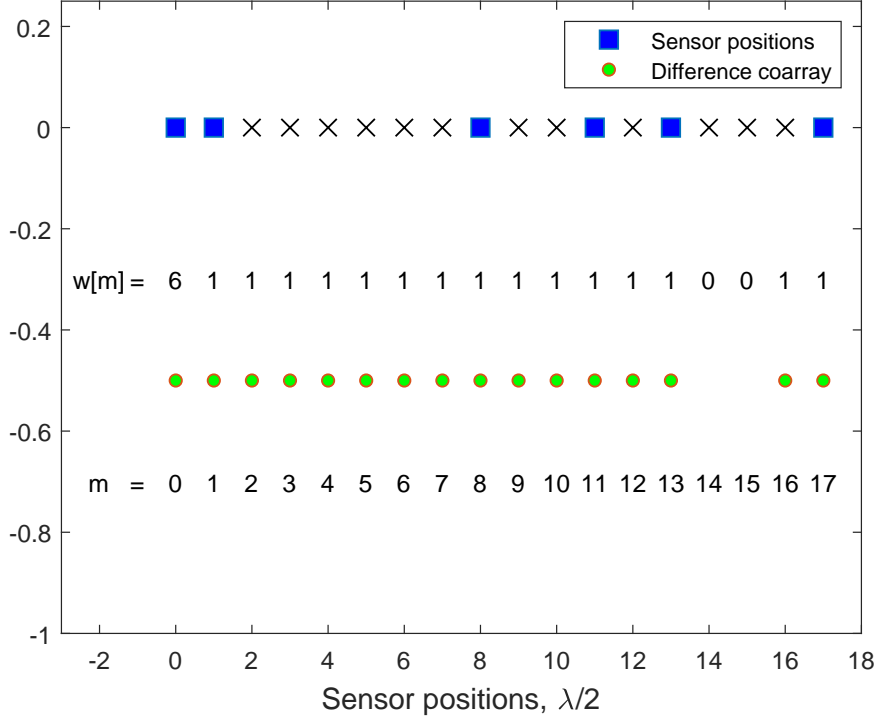
Figure 4.2: Sensor locations, non-negative part of the difference coarray and weight function values corresponding to non-negative lags for MHA with $M = 6$, $\mathbb{D} = \{0, \pm 1, \cdots, \pm 13, \pm 16, \pm 17\}$, $\mathbb{U} = \{0, \pm 1, \cdots, \pm 13\}$, $R = 1.1538$, $F = 1$

4.2.3 Minimum Redundancy Array

Minimum redundancy array (MRA) has the maximum array aperture with a hole-free difference coarray which has the minimum redundancy for a fixed number of sensors [13]. Redundancy of an array can be calculated using Equation 4.7. For a fixed number of sensors, minimizing redundancy R increases the central ULA length $|\mathbb{U}|$ which affects the angular resolution of DOA estimation methods such as SS-MVDR and SS-MUSIC. As number of elements in the central ULA segment $\mathbb{U}$ increases, beamwidth of the difference coarray $\mathbb{D}$ decreases. Since largest central ULA segment with fixed number of sensors is obtained with MRA, it has higher DOF than other sparse linear arrays. In addition, it gives smaller DOA error with DOA estimation methods for fully augmentable arrays. As an example, array geometry of 6-sensor MRA, non-negative part of its difference coarray and its weight function values corresponding to non-negative lags are shown in Figure 4.3.

38
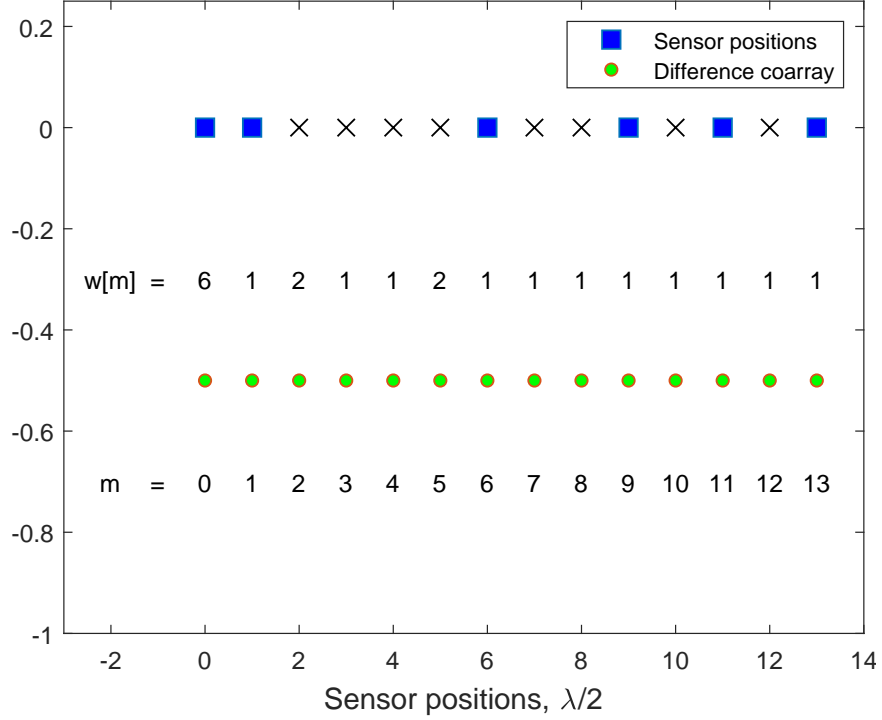
Figure 4.3: Sensor locations, non-negative part of the difference coarray and weight function values corresponding to non-negative lags for MRA with $M = 6$, $\mathbb{D} = \{0, \pm 1, \cdots, \pm 13\}$, $\mathbb{U} = \{0, \pm 1, \cdots, \pm 13\}$, $R = 1.1538$, $F = 1$

4.2.4 Robust Minimum Redundancy Array

MRA is not robust against sensor failure since its difference coarray changes and length of central ULA segment shrinks. Fragility is used as a measure of an array's robustness against sensor failure. Fragility of MRA is calculated as 1 by using Equation 4.8. On the other hand, ULA is one of the robust arrays against sensor failure. Its fragility is $2/M$ since the only essential sensors of ULA is first and last ones. There is a compromise between redundancy R and fragility F. Robust minimum redundancy array (RMRA) is proposed in [15] as a solution to this problem. RMRA is as robust as ULA since its fragility is $2/M$. Its aperture and length of central ULA segment is smaller than MRA with the same number of sensors as a result of decrease in fragility. RMRA is suitable for SS-MVDR and SS-MUSIC methods since there is no hole in its difference coarray. As an example, array geometry of 6-sensor RMRA, non-negative part of its difference coarray and its weight function values corresponding to non-negative lags are shown in Figure 4.4.

39
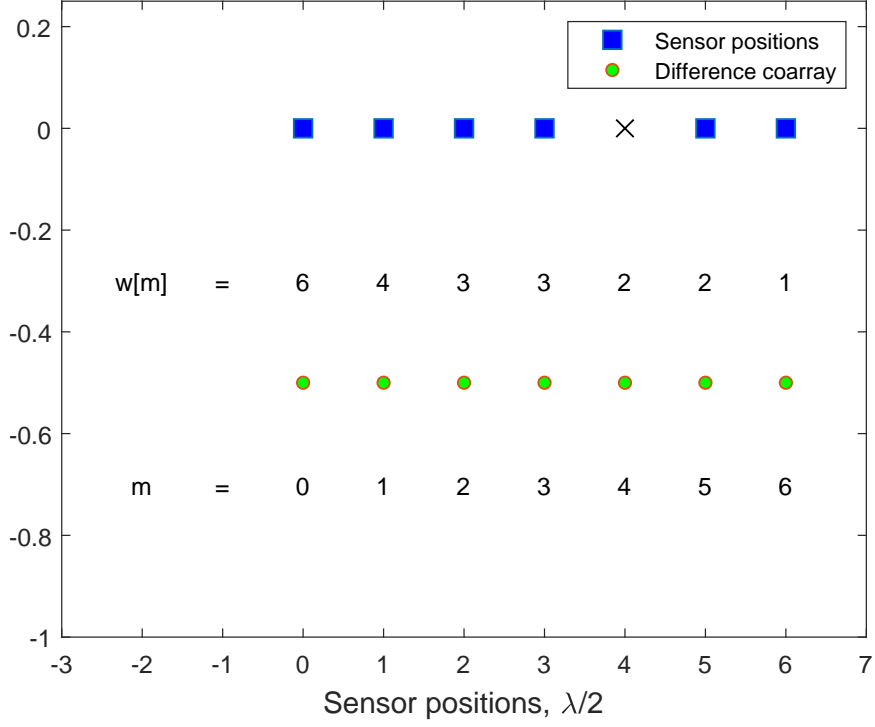
Figure 4.4: Sensor locations, non-negative part of the difference coarray and weight function values corresponding to non-negative lags for RMRA with $M = 6$, $\mathbb{D} = \{0, \pm 1, \cdots, \pm 6\}$, $\mathbb{U} = \{0, \pm 1, \cdots, \pm 6\}$, $R = 2.5$, $F = 0.333$

4.2.5 Nested Array

Nested array is formed by concatenation of multiple uniform line arrays. It has a simple array geometry and closed-form expression for sensor positions unlike perfect array, MHA, MRA and RMRA. Array design with large number of sensors is easier for nested arrays due to closed-form expressions, whereas it requires a combinatorial search for other sparse arrays (4.2.1, 4.2.2, 4.2.3, 4.2.4) mentioned in this section. According to [16], sensor positions of a nested array with 'K-level' can be expressed as

$$\mathbb{S} = \cup_{i=1}^{K} \mathbb{S}_i \tag{4.11}$$

$$\mathbb{S}_i = \left\{ -d + nd \prod_{j=1}^{i-1} (M_j + 1), \quad n = 1, 2, \cdots, M_i \right\} \quad i = 2, \cdots, K \tag{4.12}$$

$$\mathbb{S}_1 = \{ (n-1) d, \quad n = 1, 2, \cdots, M_1 \} \tag{4.13}$$

40

where M_i is the number of sensors for i^{th} level ULA, d is the element spacing of first level ULA and $K, M_1, \cdots, M_K \in \mathbb{N}^+$. Equation 4.12 means that element spacing of ith level ULA is $(M_{i-1} + 1)$ times the spacing of $(i-1)^{th}$ level ULA. Having no hole in the difference coarray is important for DOA estimation methods such as SS-MVDR and SS-MUSIC. Holes exist in the difference coarray of nested array with $K > 2$ levels. Therefore, two-level nested arrays are used for obtaining hole-free coarray. As an example, array geometry of 6-sensor nested array, non-negative part of its difference coarray and its weight function values corresponding to non-negative lags are shown in Figure 4.5.

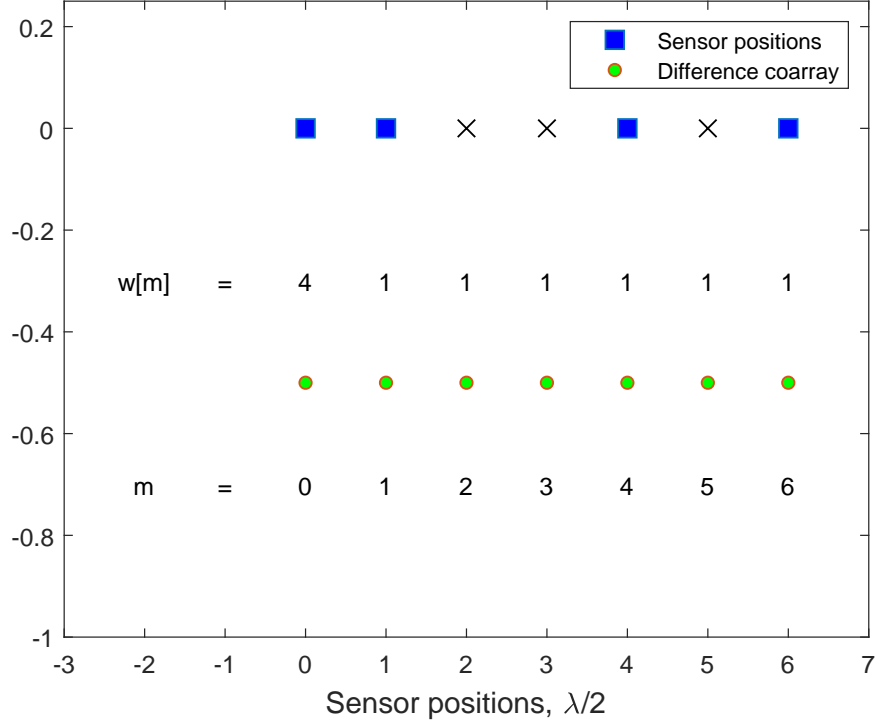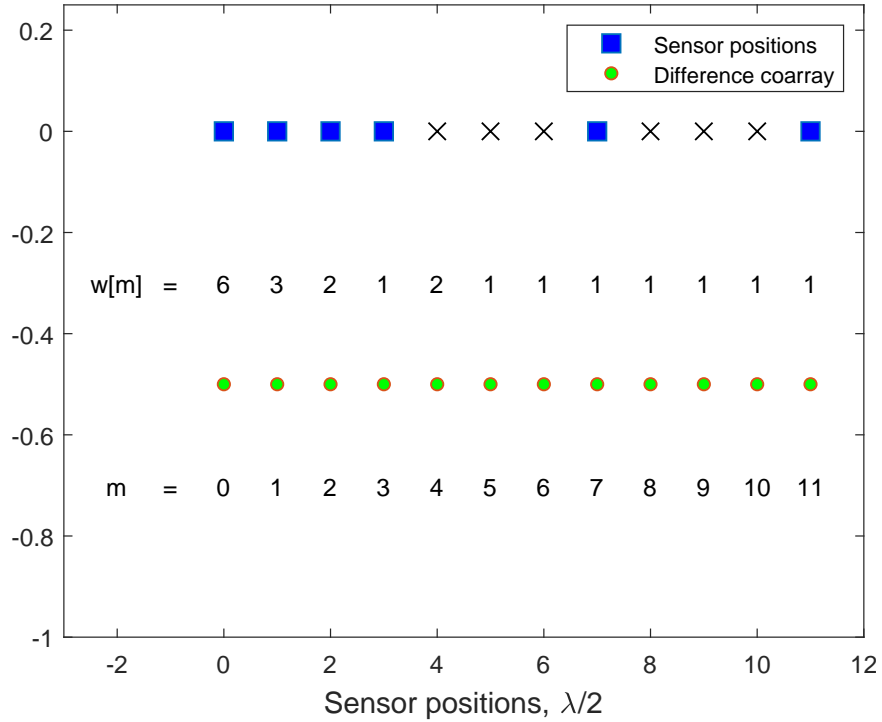Figure 4.5: Sensor locations, non-negative part of the difference coarray and weight function values corresponding to non-negative lags for nested array with $M = 6, \mathbb{D} = \{0, \pm 1, \cdots, \pm 11\}, \mathbb{U} = \{0, \pm 1, \cdots, \pm 11\}, R = 1.364, F = 1$

4.3 Coarray Processing Methods for DOA Estimation

Difference coarray concept is used for increasing the DOF that can be obtained with a sensor array. $O(M^2)$ DOF is reached by using M sensors with wider aperture as a

result of using difference coarray. Hole-free central ULA segment $\mathbb{U}$ of the difference coarray $\mathbb{D}$ gives the virtual sensor locations for coarray processing methods. In section 2.2, narrowband signal model for an M-sensor array is given in Equation 2.23. For P narrowband sources whose DOA angles are $\{\phi_1, \cdots, \phi_P\}$, covariance matrix of the data received by the sensors can be written as

$$
\begin{aligned}
\mathbf{R_y} &= \mathbf{E}\{\mathbf{y}\mathbf{y}^{\mathrm{H}}\} \\
&= \mathbf{A} \begin{bmatrix} \sigma_1^2 & & \\ & \ddots & \\ & & \sigma_P^2 \end{bmatrix} \mathbf{A}^{\mathrm{H}} + \sigma_e^2 \mathbf{I_M}
\end{aligned}
\tag{4.14}
$$

where $\mathbf{y} \in \mathbb{C}^{M \times N}$ is the sensor data matrix, $\{\sigma_1^2, \cdots, \sigma_P^2\}$ are powers of uncorrelated sources and σ_e^2 is the noise power. By vectorizing the covariance matrix, data vector for the difference coarray is expressed in [16].

$$
\begin{aligned}
\mathbf{y_V} &= \mathrm{vec}\,(\mathbf{R_y}) \\
&= \mathrm{vec}\left(\sum_{k=1}^{P} \sigma_k^2 \mathbf{a}(\phi_k)\mathbf{a}^{\mathrm{H}}(\phi_k) \right) + \sigma_e^2 \vec{\mathbf{1}}_e \\
&= (\mathbf{A}^* \odot \mathbf{A})\,\mathbf{v} + \sigma_e^2 \vec{\mathbf{1}}_e
\end{aligned}
\tag{4.15}
$$

where $\mathbf{v} = [\sigma_1^2, \cdots, \sigma_P^2]^T$, $\vec{\mathbf{1}}_e = \left[e_1^T, \cdots, e_P^T \right]^T$ and e_k is a column vector where its kth element is 1 with remaining ones being 0. $\mathbf{v}$ denotes the source signal vector for the difference coarray. Sign $\odot$ denotes Khatri-Rao product which can be defined as the column-wise Kronecker product of two matrices. $\mathbf{A}^* \odot \mathbf{A}$ represents the manifold matrix of the difference coarray which can be defined as

$$
\mathbf{A}^* \odot \mathbf{A} = [\mathbf{a}^*(\phi_1) \otimes \mathbf{a}(\phi_1), \cdots, \mathbf{a}^*(\phi_P) \otimes \mathbf{a}(\phi_P)]
\tag{4.16}
$$

where $\otimes$ denotes the Kronecker product. There are $w\,[k]$ repeated rows in $\mathbf{A}^* \odot \mathbf{A}$ which correspond to lag k. Size of $\mathbf{A}^* \odot \mathbf{A}$ is $M^2 \times P$ but some of its rows are exact replicas of each other when $w\,[k] > 1$ and it has $|\mathbb{D}|$ unique rows. To reduce the number of computations for generating the spatial spectrum, rows of the coarray sensor data $\mathbf{y}_{\mathbb{D}}$ corresponding to the repeated rows of manifold matrix $\mathbf{A}^* \odot \mathbf{A}$ can be removed and remaining rows can be sorted in an increasing order of coarray lags. Then, the data vector for the difference coarray becomes

$$
\mathbf{y}_{\mathbb{D}} = \mathbf{A}_{\mathbb{D}}\mathbf{v} + \sigma_e^2 \bar{\mathbf{1}}_e
\tag{4.17}
$$

where $\mathbf{A}_\mathbb{D} = [\mathbf{a}_\mathbb{D}(\phi_1), \cdots, \mathbf{a}_\mathbb{D}(\phi_P)]$ is the array manifold matrix of unique elements of the difference coarray and $\bar{\mathbf{1}}_e \in \mathbb{R}^{|\mathbb{D}| \times 1}$ is the noise vector whose $((|\mathbb{D}| + 1)/2)$th element is 1 and the others are 0. Covariance matrix that will be used for coarray DOA estimation methods can be calculated as

$$\mathbf{R}_{\mathbf{y}_\mathbb{D}} \triangleq \mathbf{y}_\mathbb{D}\mathbf{y}_\mathbb{D}^{\mathrm{H}} \tag{4.18}$$

For DOA estimation using coarrays, covariance matrix augmentation and its variants were studied in the earlier works despite of some disadvantages. Not obtaining a positive semi-definite covariance matrix with limited number of snapshots [39, 40] and requiring use of minimum redundancy arrays [41, 42] are some drawbacks of augmented covariance matrix method. In recent studies, new DOA estimation methods are shown by combining subspace techniques with Khatri-Rao product without having any problem caused by covariance matrix augmentation [16, 17]. In this section, these methods are explained in detail.

4.3.1 Classical Coarray Beamforming

Classical beamforming for the difference coarray [16] is similar to the Bartlett beamformer which is explained in 3.2.1. It differs from Bartlett beamformer by using signal powers instead of signal amplitudes due to the signal model difference between Equation 2.22 and 4.17. By using the weight $\mathbf{w}$, beamformer output can be found as

$$\begin{aligned}
z_\mathbb{D} &= \mathbf{w}^{\mathrm{H}}\mathbf{y}_\mathbb{D} \\
&= \sum_{k=1}^{P} \mathbf{w}^{\mathrm{H}}\mathbf{a}_\mathbb{D}(\phi_k)\sigma_k^2 + \sigma_e^2\mathbf{w}^{\mathrm{H}}\bar{\mathbf{1}}_e \\
&= \sum_{k=1}^{P} B_\mathbb{D}(\phi_k)\sigma_k^2 + \sigma_e^2\mathbf{w}^{\mathrm{H}}\bar{\mathbf{1}}_e
\end{aligned} \tag{4.19}$$

where $B_\mathbb{D}(\phi)$ is defined as the beampattern of difference coarray $\mathbb{D}$. It is a nonlinear beamformer since it uses the autocorrelation of the data received by the sensors. Beamformer output $z_\mathbb{D}$ is formed by weighted sum of the source powers with respect to $B_\mathbb{D}(\phi_k)$ and scaled noise variance. Weight vector of direction ϕ_k is the normalized array manifold matrix for undistorted response.

$$\mathbf{w} = \frac{\mathbf{a}_\mathbb{D}(\phi_k)}{|\mathbb{D}|} \tag{4.20}$$

Spatial spectrum obtained with classical coarray beamformer can be found by putting Equation 4.20 and 4.18 into 3.4.

$$P_{z_{\mathbb{D}}}(\phi) = \frac{\mathbf{a}_{\mathbb{D}}^{\mathrm{H}}(\phi)\,\mathbf{R}_{\mathbf{y}_{\mathbb{D}}}\mathbf{a}_{\mathbb{D}}(\phi)}{|\mathbb{D}|^2} \tag{4.21}$$

where $\phi \in \{\phi_k,\ k = 1, \cdots, L\}$ is the steering direction, $P_{z_{\mathbb{D}}}(\phi)$ is the power of the beamformer output for the direction ϕ, L is the number of steering angles and $|\mathbb{D}|$ is the number of elements in the difference coarray.

4.3.2   Spatially Smoothed Covariance Matrix

After vectorizing the covariance matrix, source and noise vectors become deterministic in the coarray signal model in Equation 4.17. In other words, elements of source vector are equal to source signal variances which are constant for Gaussian signals. Elements of the noise vector also take constant values of one and zeros. To increase the rank of the covariance matrix $\mathbf{R}_{\mathbf{y}_{\mathbb{D}}}$, spatial smoothing technique shown in 3.5 is applied onto it. Since the hole free difference coarray is a ULA and the manifold matrix $\mathbf{A}_{\mathbb{D}}$ has the Vandermonde structure, this technique is suitable for hole-free sparse arrays such as perfect arrays, MRA and nested arrays. To appy spatial smoothing, the difference coarray is divided into $(|\mathbb{D}|+1)/2$ overlapping subarrays. Each subarray has $(|\mathbb{D}|+1)/2$ elements and overlap size is $(|\mathbb{D}|-1)/2$. Sensor positions of kth subarray can be written as

$$\mathbb{S}_{sub,k} = \left\{ \left(k + n - \frac{(|\mathbb{D}|+1)}{2}\right)\lambda/2, \quad n = 0, 1, \cdots, \frac{|\mathbb{D}|-1}{2} \right\} \tag{4.22}$$

Data vector of kth subarray is denoted by $y_{sub,k}$ and equals to the row k to the row $(k + (|\mathbb{D}|-1)/2)$ of the coarray data vector $\mathbf{y}_{\mathbb{D}}$.

$$\mathbf{y_{sub,k}} = \mathbf{A_{sub,k}}\mathbf{v} + \sigma_e^2\bar{\mathbf{1}}_{sub,k} \tag{4.23}$$

where $\mathbf{A_{sub,k}} = [\mathbf{a_{sub,k}}(\phi_1), \cdots, \mathbf{a_{sub,k}}(\phi_P)]$ is the array manifold matrix of the kth subarray and $\bar{\mathbf{1}}_{sub,k}$ is the noise vector whose $(-k + (|\mathbb{D}|+3)/2)$th element is 1 and the others are 0. $\mathbf{A_{sub,k}}$ corresponds to the kth to $(k + (|\mathbb{D}|-1)/2)^{th}$ rows of $\mathbf{A}_{\mathbb{D}}$. Covariance matrix of the kth subarray can be calculated as

$$\mathbf{R_{sub,k}} \triangleq \mathbf{y_{sub,k}}\mathbf{y}_{\mathbf{sub,k}}^{\mathrm{H}} \tag{4.24}$$

After calculating the covariance matrices for each subarray, spatially smoothed covariance matrix for difference coarray can be found as

$$\mathbf{R_{ss}} \triangleq \frac{1}{\frac{|\mathbb{D}|+1}{2}} \sum_{k=1}^{(|\mathbb{D}|+1)/2} \mathbf{R_{sub,k}} \qquad (4.25)$$

By using spatially smoothed covariance matrix $\mathbf{R_{ss}}$, DOA angles of $O\left(M^2\right)$ sources can be estimated with M sensors for DOA estimation methods such as SS MVDR and SS MUSIC. Despite of reaching highest attainable number of rank for the covariance matrix, DOF is reduced from $|\mathbb{D}|$ to $(|\mathbb{D}| + 1)/2$ as a result of data smoothing. Since spatial smoothing technique requires the coarray as a filled ULA, it can not be used with the sparse arrays whose coarrays have holes.

4.3.3 SS MVDR

MVDR beamformer [33] in 3.2.2 could be utilized for DOA estimation problem using difference coarray. It is possible for MVDR beamformer to place nulls towards the interference directions and have a unity gain at the steering direction. Rank of covariance matrix of the difference coarray $\mathbf{R_{y_\mathbb{D}}}$ is 1 since source and noise signals are represented by deterministic power vectors $\mathbf{v}$ and $\bar{\mathbf{1}}_e$. MVDR beamformer is not capable of separating fully coherent sources . By using spatial smoothing, full column rank is reached for the covariance matrix. SS MVDR beamformer is a variant of MVDR beamformer with a spatially smoothed covariance matrix [16]. SS MVDR weight for steering direction ϕ can be calculated by inserting $\mathbf{R_{ss}}$ instead of $\hat{\mathbf{R}}_\mathbf{y}^{-1}$ into the classical MVDR equation in 3.38. Then, SS MVDR weigth and spatial spectrum equations can be written as

$$\mathbf{w} = \frac{\mathbf{R_{ss}^{-1}a_{ss}}(\phi)}{\mathbf{a_{ss}}^\mathrm{H}(\phi)\mathbf{R_{ss}^{-1}a_{ss}}(\phi)} \qquad (4.26)$$

$$P_\mathbf{z}\left(\phi\right) = \frac{1}{\mathbf{a_{ss}}^\mathrm{H}\left(\phi\right)\mathbf{R_{ss}^{-1}a_{ss}}\left(\phi\right)} \qquad (4.27)$$

where $\mathbf{a_{ss}}\left(\phi\right)$ is the reference subarray manifold vector for steering direction $\phi \in \{\phi_k,\ k = 1,\cdots,L\}$, $P_{z_\mathbb{D}}\left(\phi\right)$ is the power of the beamformer output for the direction ϕ and L is the number of steering angles. $\mathbf{a_{ss}}$ corresponds to the $\left(\left(|\mathbb{D}| + 1\right)/2\right)^{th}$ subarray whose sensors are located at $\left\{n\lambda/2,\quad n = 0, 1,\cdots, \frac{|\mathbb{D}|-1}{2}\right\}$.

4.3.4 SS MUSIC

Utilizing subspace techniques such as MUSIC is another DOA estimation method that can be used for difference coarrays [16]. Number of sources should be known or estimated in order to find the noise subspace correctly. It can be estimated using eigenvalue based techniques such as Akaike information criterion (AIC) and minimum description length (MDL). However, rank of the covariance matrix of difference coarray $\mathbf{R}_{\mathbf{y}_\mathbb{D}}$ is 1 due to the deterministic source and noise vectors in the data model. Rank of the covariance matrix can be restored using spatial smoothing. SS MUSIC is a variant of MUSIC technique with a spatially smoothed covariance matrix. Spatial spectrum of SS MUSIC is obtained by applying eigen decomposition on $\mathbf{R}_{\mathbf{ss}}$ instead of $\mathbf{R}_{\mathbf{y}}$. Then, SS MUSIC spectrum can be written as

$$P_{\mathbf{SS-MUSIC}}\left(\phi\right) = \frac{1}{\mathbf{a_{ss}}^{\mathrm{H}}\left(\phi\right)\mathbf{U}_{N,ss}\mathbf{U}_{N,ss}^{\mathrm{H}}\mathbf{a_{ss}}\left(\phi\right)} \tag{4.28}$$

where $\mathbf{U}_{N,ss}$ is the noise subspace formed by the eigenvectors of $\mathbf{R}_{\mathbf{ss}}$ with smallest $M - P$ eigenvalues $\{\lambda_{P+1}, \cdots, \lambda_M\}$. $\mathbf{a_{ss}}$ is the manifold matrix of reference subarray which corresponds to the $\left(\left(|\mathbb{D}| + 1\right)/2\right)^{th}$ subarray with sensors located at $\left\{n\lambda/2, \quad n = 0, 1, \cdots, \frac{|\mathbb{D}|-1}{2}\right\}$. SS MUSIC algorithm for DOA estimation is summarized in Algorithm 2. An example of spatial spectra for classical coarray beamforming, SS MVDR and SS MUSIC methods are illustrated in Figure 4.6. A two level nested array with $M_1 = M_2 = 5$ is used and these spectra are generated by using *N = 100000* snapshots. There are *P = 2* narrowband sources with *SNR = 10 dB* and DOA angles of them are $\{80°, 100°\}$. Peaks in SS MVDR and SS MUSIC spectrum is much sharper than the ones in classical beamforming spectrum which results in better target separation for SS MVDR and SS MUSIC techniques. Peak levels in classical beamforming and SS MVDR spectrum show true source levels at the sensor input, whereas peak levels at the SS MUSIC spectrum are greater.
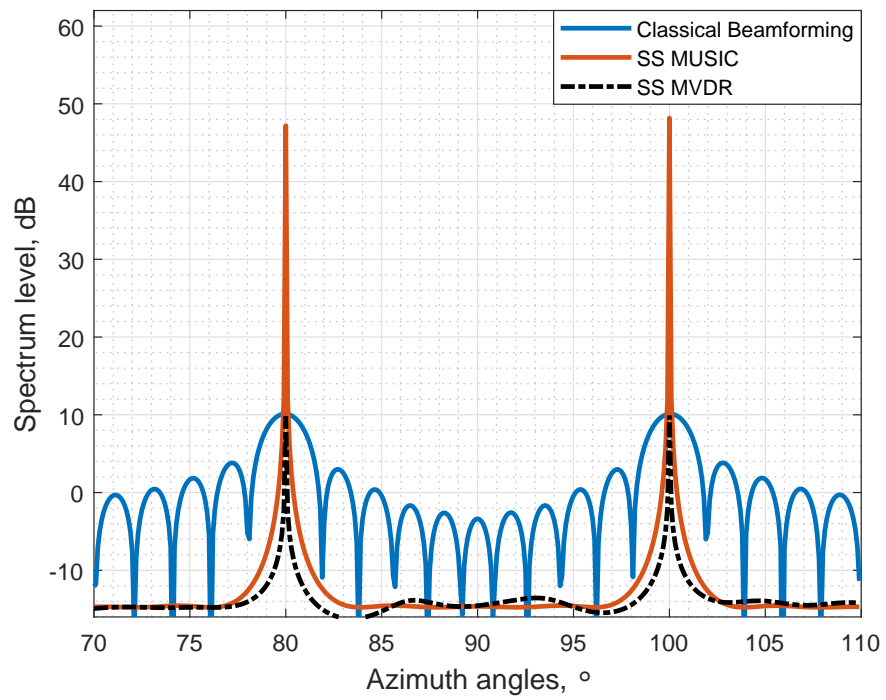
Figure 4.6: Spatial spectra using classical coarray beamforming, SS MVDR and SS MUSIC methods on a two level nested array with $M_1 = M_2 = 5$, $N = 100000$, $P = 2$, $\mathrm{SNR} = 10$ dB

Algorithm 2 SS MUSIC Algorithm

1: Compute manifold matrix for the physical array

   $$\mathbf{A} = [\mathbf{a}(\phi_1), \cdots, \mathbf{a}(\phi_L)]$$

2: Compute distances between each sensors

   $$d_{mn} = x_m - x_n \quad m = 1, \cdots, M \quad n = 1, \cdots, M$$

3: Find unique distances and corresponding element indices in d_{mn}

4: Compute manifold matrix $\mathbf{A}^* \odot \mathbf{A}$ of the difference coarray

5: Find $\mathbf{A}_\mathbb{D}$ by deleting repeated rows of $\mathbf{A}^* \odot \mathbf{A}$ and sort them according to the corresponding d_{mn}

6: Find manifold matrix $\mathbf{A_{ss}}$ for the reference subarray by selecting last $(|\mathbb{D}| + 1)/2$ rows of $\mathbf{A}_\mathbb{D}$

7: Compute sample covariance matrix

   $$\mathbf{R_y} = \sum_{k=0}^{N-1} \mathbf{y}(kT)\mathbf{y}^{\mathrm{H}}(kT)$$

8: Vectorize $\mathbf{R_y}$ to obtain the data vector of the difference coarray

   $$\mathbf{y_V} = \mathrm{vec}\,(\mathbf{R_y})$$

9: Delete the rows of $\mathbf{y_V}$ which corresponds to the repeated values of d_{mn} and sort them with the same order as $\mathbf{A}_\mathbb{D}$ to obtain $\mathbf{y}_\mathbb{D}$

10: Compute the spatially smoothed covariance matrix $\mathbf{R_{ss}}$ from $\mathbf{y}_\mathbb{D}$

   $$\mathbf{y_{sub,k}} = \left[\mathbf{y_{\mathbb{D},k}}, \cdots, \mathbf{y_{\mathbb{D},k+(|\mathbb{D}|-1)/2}}\right]^T$$
   $$\mathbf{R_{ss}} \triangleq \frac{1}{\frac{|\mathbb{D}|+1}{2}} \sum_{k=1}^{(|\mathbb{D}|+1)/2} \mathbf{y_{sub,k}}\mathbf{y_{sub,k}^H}$$

11: Perform eigendecomposition

   $$\mathbf{R_{ss}} = \mathbf{U}_{ss}\mathbf{\Sigma}\mathbf{U}_{ss}^{\mathrm{H}}$$

12: Construct noise subspace matrix by choosing the eigenvectors belonging to the smallest M-P eigenvalues

   $$\mathbf{\Sigma}_N = diag\,\{\lambda_{P+1}, \cdots, \lambda_M\}$$
   $$\mathbf{U}_{N,ss} = [\mathbf{u}_{P+1}, \cdots, \mathbf{u}_M]$$

13: **for** $(\phi, \theta) = \{(\phi_1, \theta_1), \cdots, (\phi_L, \theta_L)\}$ **do**

14:    Compute spatial spectrum for direction (ϕ)

   $$P_{\mathbf{SS-MUSIC}}(\phi) = \frac{1}{\mathbf{a_{ss}}^{\mathrm{H}}(\phi)\mathbf{U}_{N,ss}\mathbf{U}_{N,ss}^{\mathrm{H}}\mathbf{a_{ss}}(\phi)}$$

15: **end for**

16: Find the DOA angle estimates by finding P highest peaks in the spectrum

---

CHAPTER 5

ARRAY LAYOUT OPTIMIZATION BY USING GENETIC ALGORITHM

Using all of the sensors in a large sparse array brings many disadvantages in terms of array performance. Depending on the sparsity level of the array, high sidelobe levels, grating lobes and unnecessary power consumption [24] can be obtained for a sparse array unless less number of sensors are used. Selection of an array from the elements of a large array is an optimization problem when the optimum solution does not have a closed form expression. Without using optimization, 2^M different combinations are tried for finding a solution for an array with M sensors. In the literature, this problem is also named as *array thinning*. As the number of sensors increases, solution space for the optimization problem becomes larger. It is hard to find an optimum solution for a large solution space. Most of the well-known optimization methods such as conjugate gradient and down-hill simplex are used for continuous parameters [22]. However, array layout optimization requires discrete parameters and a bit string as a solution. Evolutionary algorithms such as genetic algorithm and particle swarm optimization are suitable for this problem despite of slow convergence to a solution [43]. In the context of this thesis study, genetic algorithm is selected for the array layout optimization in this thesis. Detailed information about genetic algoritm with its important parameters and different cost function parameters for the optimization will be given throughout this chapter.

5.1 Genetic Algorithm

Genetic algorithm is a search method which is developed by John Holland [18]. It is based on the application of the ideas in genetics and natural selection. Aim of the
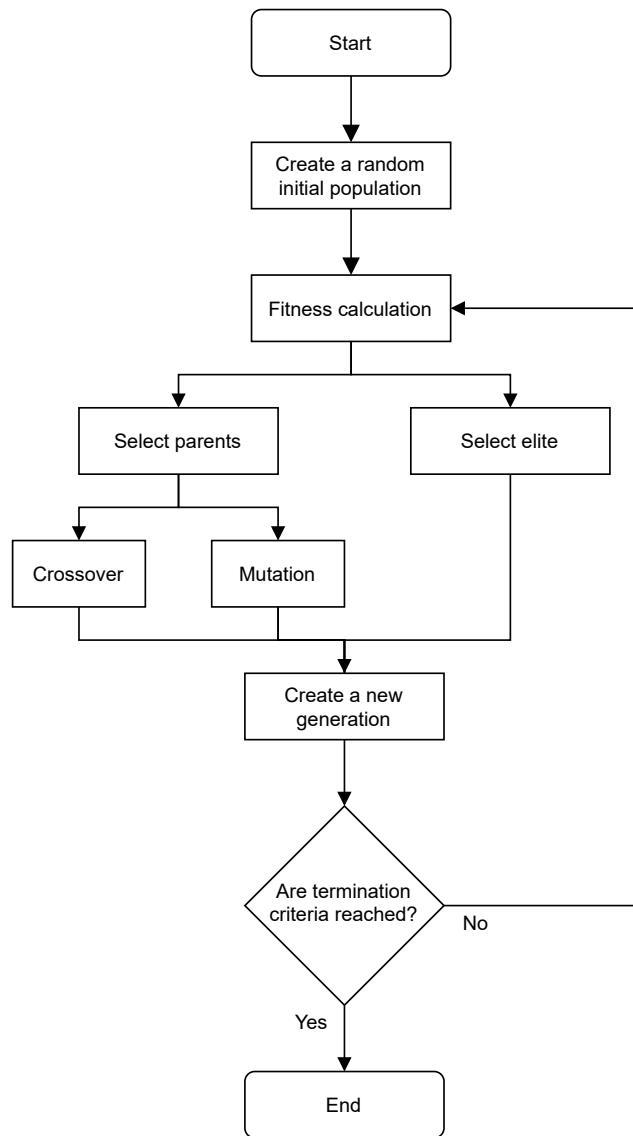
Figure 5.1: Flowchart of the Genetic Algorithm

algorithm is to obtain an optimum solution that gives the minimum value for the selected cost function. It has distinctive properties different from the other optimization methods [19]. It uses a coding of parameters instead of the parameters themselves. Multiple points are used for searching and derivatives are not used. Optimization parameters are encoded in the form of bit strings. Each of these strings is called an *individiual*. Optimization process is made over multiple individiuals, which as a group is called a *population*. Each individual is evaluated using a *cost function* and a *fitness value* is obtained. All individuals that exist in an iteration is named as a *generation*. Nature inspired processes such as *crossover* and *mutation* is applied on

the current generation and fittest individuals that have the lowest fitness values are survived into the next generation. Some of the fittest individuals are separated as an *elit*. Members of the elite is directly passed into the next generation. These processed are repeated until one of the termination criteria is reached. These criteria could be a fitness value limit, maximum number of generation and an average relative change limit. After one of these criteria is met, fittest individiaul in the last generation is reported as the result of the optimization. Flowchart of the genetic algorithm is shown in Figure 5.1. In the following subsections, detailed information about main steps of the algorithm will be given.

5.1.1   Creation of Initial Population

First step of the genetic algorithm is to create an initial population. Every individual in the population is represented by M bits. Bits of all individuals in the initial population are generated randomly. In MATLAB, these bits are created with uniform distribution as the default option. Size of the initial population affects the performance of the algorithm. Large population size has a higher possibility of finding a global minimum point with a slower convergence. In the array layout optimization problem, selected (ON) elements are shown with 1 and remaining (OFF) elements are shown with 0. For example, a selected subarray $\mathbb{S} = \{0, 1, 3, 5\}$ from a 6 element ULA is represented by the bit string 110101 where 3rd and 5th sensors are OFF elements. Number of ON elements for an individual is half of the total number of elements in average when the initial population is generated with uniform distribution.

5.1.2   Selection of Parents

Individuals of the current generation are evaluated using a selected cost function and a fitness value is assigned to each one. A fraction of the individuals with the lowest fitness values are assigned as *elite* and they are automatically selected for the next generation. Remaining individuals are selected as *parents* by using different selection methods. In general, selection methods favor the fittest individuals to create childrens with lower fitness values. In [44], selection methods are divided into 2 groups which

51

are fitness proportionate selection and ordinal selection methods.

Stochastic uniform [20] and roulette-wheel selection [19] can be classified into the fitness proportionate section. In stochastic uniform selection, each individual is represented with a line section whose length is proportional to the fitness value. As the algorithm samples the line by moving with equal steps, parents are selected at the sampling points. In roulette-wheel selection, each individual is represented with a slot whose size is proportional to the fitness value. Fittest individuals have a bigger slot size which increases the possiblity to select as a parent.

Tournament selection [19] can be classified into the ordinal selection method. In this method, n individuals are selected randomly into a tournament and the one with the lowest fitness value is selected as a parent. This method is used to select the parents for the optimizations whose results are presented in this thesis.

5.1.3 Reproduction of Current Generation

After selecting the parents, crossover and mutation operations are performed and the new generation is created. Most of the parents reproduce with crossover which can be done with different methods. Matched parents exchange parts of their bits and these new bits are assigned to the children. Uniform [45], scattered, k-point and laplace crossover [46] are some of the algorithms that are used for the crossover.

In uniform crossover, every bit is swapped between the parents with a swapping probability p_e. Bit of interest is changed when the generated random number is greater than p_e. In scattered crossover, a vector with random binary elements is created. Bits of the first parent goes to the first child when bits of the random vector are 1. In case of 0 bits in the random vector, bits of the second parent goes to the first child. Opposite rules are valid for the second children. When the first parent is 10101, the second parent is 00111 and the binary vector is 11100, first and second children becomes 10111 and 00101 respectively. In k-point crossover, every bit sequence of the parents are divided into $k + 1$ parts and parts of the first parent are swapped with second parent. When the first parent is 11100, the second parent is 00101 and the crossover point is 2, first and second children becomes 10101 and 00111 respectively for the

52

1-point crossover. In laplace crossover [46], bits of the children are generated as

$$c_k^1 = p_k^1 + \beta_k \left| p_k^1 - p_k^2 \right|$$
$$c_k^2 = p_k^2 + \beta_k \left| p_k^1 - p_k^2 \right|$$

where p_k^1 and p_k^2 are the kth bits of the parents, c_k^1 and c_k^2 are the kth bits of the children and β_k is a random number generated with Laplace distribution. When the first parent is 11100, the second parent is 00101 and $\beta = \{0, 1, -1, 1, 1\}$, first and second children becomes 11101 and 01101 respectively for the laplace crossover. This crossover method is the default option for integer genetic algorithm optimizaion in MATLAB and it is used in the all optimizations given in this thesis.

Crossover operation may lead the optimization to stuck at a local minimum point since the solution space is bounded by the bits of the parents. In addition, children have the same bit values if the parents has the same bit string. To increase the search space and bring diversity to the existing parents, mutation operation is used in the genetic algorithm. Small ratio of the parents are selected for the mutation to prevent late convergence. Uniform, gaussian and power mutation [46] are some of the algorithms that are used for the mutation. In uniform method, each member of the bit string of a parent can be flipped with a mutation probability which takes low values in general. Some parts of the parent are mutated by changing zeros with ones or ones with zeros. In gaussian method, each element of a parent is modified by adding a random number with zero-mean Gaussian distribution. As the generation number increases, standard deviation of the Gaussian distribution shrinks. In power mutation, a mutation child is created as

$$c_k = \begin{cases} p_k - s \left(p_k - p_k^l \right), & t_k < r \\ p_k + s \left(p_k^u - p_k \right), & t_k \geq r \end{cases} \tag{5.1}$$

where c_k is k^{th} component of the child, p_k is k^{th} component of the parent, p_k^l is the lower bound on the value of kth component, p_k^u is the upper bound on the value of kth component, s is a random number with power distribution, $t_k = \left(p_k - p_k^l \right) / \left(p_k^u - p_k \right)$ and r is a random number with uniform distribution between 0 and 1. This mutataion method is the default option for integer genetic algorithm optimization in MATLAB and it is used in the all optimizations given in this thesis.

Childrens are generated with crossover and mutation operations. Crossover and mu-

tation childrens with elite individuals form the population of the new generation. Fitness calculation, elite and parent selection, crossover and mutation steps are repeated until one of the termination criteria are reached. Termination criteria might be chosen as limits of generation number, time, fitness value and average fitness change.

5.2 Cost Function Parameters for Array Layout Optimization

Aim of the optimization problems is to minimize the fitness value which is evaluated by using a cost function. Different cost functions could be used for the array layout optimization problem. Since the individuals in the genetic algorithm is encoded as bit strings, these strings cannot be used in the cost function directly. Firstly, sensor positions are obtained by selecting the sensors which are shown with 1 in the bit string. Then, array parameters are calculated with the selected sensors and fitness values are computed for the desired cost function. In this section, five different cost functions will be explained for the array layout optimization problem. These cost functions are peak-to-sidelobe level, bayesian CRB, bayesian MIE , redundancy and fragility. In chapter 6, array layouts obtained by using these cost functions and their combinations will be shown and their performances will be compared.

5.2.1 Peak-to-sidelobe Level (PSL)

Peak-to-sidelobe level is the maximum level difference between the mainlobe and the sidelobes. It depends on the sensor positions $\{p_k, \quad k = 1, \cdots, M\}$, steering angle ϕ_m and operating frequency f_c. After calculating the beampattern steered to ϕ_m, PSL can be computed as

$$\text{PSL}_\phi = \max\left\{B_p\left(\phi_m\right) + B_p\left(\phi_l\right)\right\}, \quad l = 1, \cdots, N_{sidelobes} \qquad (5.2)$$

where ϕ_m is mainlobe angle, $\{\phi_l, l = 1, \cdots, N_{sidelobes}\}$ are sidelobe angles, $N_{sidelobes}$ is number of sidelobes and $B_p\left(\phi\right)$ is the beampattern value in dB for the direction ϕ. Equation 2.30 is used for calculating the beampattern. If the weight vector $\mathbf{w}$ is scaled for undistorted response $\mathbf{w}^{\text{H}}\mathbf{a}(\phi) = 1$, beampattern value at mainlobe angle

becomes 0 dB. Then, Equation 5.2 becomes

$$\text{PSL}_\phi = \max\left\{B_p\left(\phi_l\right)\right\}, \quad l = 1, \cdots, N_{sidelobes} \tag{5.3}$$

Sidelobe levels affect the detection performance of the array. False targets appear in the spatial spectrum when the sidelobe levels at the source directions are high except for the target of interest. In addition, grating lobes appear if the Nyquist criteria is not satisifed in the array. Minimizing the sidelobe levels is an option for overcoming these problems. However, there is a tradeoff between minimizing the sidelobe levels and maximizing the beamwidth. Beamwidth increases as the sidelobe levels decrease. As a result, resolution of the array to separate two close sources decreases. PSL is one of the most used cost functions in the array thinning literature [23, 24] due to its calculation simplicity. In this thesis, Bartlett beamformer which is given in 3.2.1 will be used for the PSL calculations.

5.2.2 Bayesian Cramer Rao Bound

Cramer Rao bound is a lower bound for the covariance of any unbiased estimator [26]. It can be used as a lower bound on the variance of DOA angle estimation error for any array. It sets a benchmark for the DOA angle estimation methods. Since it is algorithm independent, it is a suitable metric for comparison of the different arrays and array layout optimization. According to [47], deterministic CRB of an array for DOA estimation can be written as

$$\mathbf{C}_{\text{CRB}}\left(\phi\right) = \frac{\sigma_e^2}{2N}\left\{Re\left[\left[\mathbf{R}_s\mathbf{A}^H\mathbf{R}_y^{-1}\mathbf{A}\mathbf{R}_s\right] \circ \left[\mathbf{D}^H\mathbf{\Pi}_\mathbf{A}^\perp\mathbf{D}\right]^T\right]\right\}^{-1} \tag{5.4}$$

where $\mathbf{D} = [\mathbf{d}_1, \cdots, \mathbf{d}_P]$, $\mathbf{d}_k = \frac{\partial \mathbf{a}(\phi_k)}{\partial \phi_k}$, $\mathbf{A} = [\mathbf{a}\left(\phi_1\right), \cdots, \mathbf{a}\left(\phi_P\right)]$, $\mathbf{\Pi}_\mathbf{A}^\perp = \mathbf{I} - \mathbf{A}\left(\mathbf{A}^H\mathbf{A}\right)^{-1}\mathbf{A}^H$, $\mathbf{R}_s$ is the signal covariance matrix, σ_e^2 is the variance of the noise, N is the number of snapshots, P is the number of sources and $\circ$ denotes the Hadamard product.

CRB is a tight bound for DOA estimators under high SNR. However, RMSE curve diverges from the CRB and it increases rapidly as the SNR decreases. This phenomenon is called *threshold effect* in MSE performance curves [48]. A typical RMSE curve for an efficient estimator is shown in Figure 5.2 together with the CRB curve.

55

RMSE curve can be divided into three different regions; namely asymptotic region, threshold region and no information region [27]. In asymptotic region, RMSE values converge to CRB curve and DOA angle estimation errors are driven by mainlobe errors. The starting point where the RMSE values and CRB curve take different values is called threshold SNR and denoted by SNR_{TH}. As SNR value drops below SNR_{TH}, RMSE values increase due to the gross errors caused by the high sidelobe levels. RMSE values become stationary after some point. This point is called no information SNR and denoted by SNR_{NI}. The region between SNR_{NI} and SNR_{TH} is named as threshold region and region corresponding to $\text{SNR} < \text{SNR}_{NI}$ is called no information region.
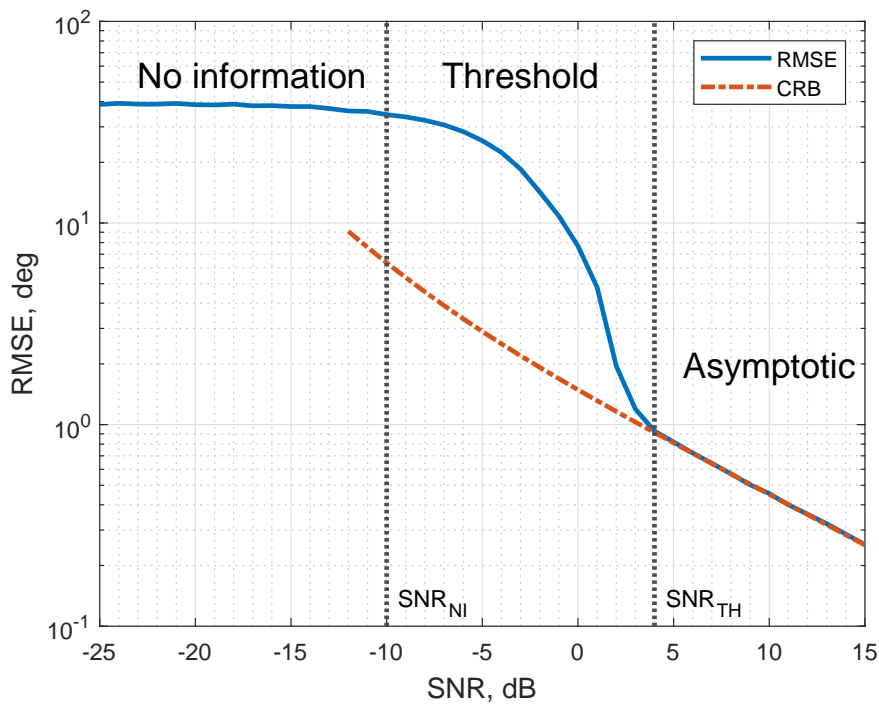
Figure 5.2: RMSE and CRB curves for DOA estimation of single source using deterministic signal model with 10 element ULA, $N = 1$, $N_{\text{MTC}} = 10000$, $\phi = 90°$

Decreasing SNR_{TH} is desired in the array design for most of the DOA estimation applications. In practice, SNR of the sources can be low and error in the angle estimation could be high if the SNR of interest is below the threshold SNR. By using CRB as the cost function in the genetic algorithm, a subarray can be selected with

lower SNR_{TH}. However, deterministic CRB is an angle dependent array parameter. Source could be available at any angle and the deterministic CRB must be calculated for a number of different angle values, if it is to be used as a cost function. Calculating deterministic CRB for different angles (covering the interval of interest with a certain resolution) and taking a weighted average (weighting with the apriori density of target DOA) of the results is actually equivalent to calculating the Bayesian CRB. Bayesian CRB derivation involves a similar approach assuming that apriori probability density of the source distribution is known. In [28], the Fisher information matrix (FIM) is written as

$$\mathbf{J}_B = \mathbf{J}_D + \mathbf{J}_P \tag{5.5}$$

where $\mathbf{J}_D$ is the FIM due to the data and $\mathbf{J}_P$ is the FIM due to the distribution of the source which can be calculated as

$$[\mathbf{J}_P]_{ij} = -E\left[\frac{\partial^2 \ln p_\phi(\phi)}{\partial \phi_i \partial \phi_j}\right] \tag{5.6}$$

If the source has a uniform distribution between ϕ_l and ϕ_r, then the probability density function of the source becomes $p_\phi(\phi) = 1/|\phi_l - \phi_r|$. Since the distribution is independent of ϕ, $[\mathbf{J}_P]_{ij} = 0$. For a single source, FIM due to the data can be calculated as

$$\mathbf{J}_D = \int_{\phi_l}^{\phi_r} \mathbf{C}_{\text{CRB}}^{-1}(\phi) \, p_\phi(\phi) \, d\phi$$

$$= \frac{1}{|\phi_l - \phi_r|} \int_{\phi_l}^{\phi_r} \mathbf{C}_{\text{CRB}}^{-1}(\phi) \, d\phi \tag{5.7}$$

Bayesian FIM for a single source with uniform distribution can be found by putting Equations 5.6 and 5.7 into Equation 5.5

$$\mathbf{J}_B = \frac{1}{|\phi_l - \phi_r|} \int_{\phi_l}^{\phi_r} \mathbf{C}_{\text{CRB}}^{-1}(\phi) \, d\phi \tag{5.8}$$

Equation 5.8 means that Bayesian FIM for a uniform source distribution is the mean FIM of angles $\phi_l \leq \phi \leq \phi_r$. Bayesian CRB can be approximately found with finite number of angles by taking the mean value of the FIM values of those angles as follows,

$$\mathbf{C}_{\text{BCRB}} \approx \frac{1}{\frac{1}{L}\sum_{k=1}^{L} \mathbf{C}_{\text{CRB}}^{-1}(\phi_k)} \tag{5.9}$$

where L is the number of angles, $\phi_l = \phi_1$ is the lower bound and $\phi_r = \phi_L$ is the upper bound on the source angle distribution. Bayesian CRB given in Equation 5.9 is

a bound on the variance of error in the angle estimation. Square root of the Bayesian CRB which can be denoted as $\mathrm{CRB_{Bayesian}}$ will be used in the optimization problems in Chapter 6 to be able to compare with RMSE curves. $\mathrm{CRB_{Bayesian}}$ can be found as,

$$\begin{aligned}\mathrm{CRB_{Bayesian}} &= \sqrt{\mathbf{C}_{\mathrm{BCRB}}} \\ &= \frac{1}{\sqrt{\frac{1}{L}\sum_{k=1}^{L}\mathbf{C}_{\mathrm{CRB}}^{-1}(\phi_k)}}\end{aligned} \tag{5.10}$$

After calculating Bayesian CRB for different SNR values, threshold SNR of the array can be found by searching the lowest SNR point where RMSE values and Bayesian CRB curve overlap.

5.2.3 Bayesian Method of Interval Errors

Finding the threshold SNR requires computation of the RMSE values for the DOA estimator. In order to obtain a smooth curve, large number of Monte Carlo simulations are needed with longer simulation time. Instead of excessive simulations, MSE can be approximated with method of interval errors (MIE) for maximum likelihood estimator (MLE) [27]. CRB brings a good approximation to only the asymptotic region of MSE, whereas MIE could approximate the asymptotic region and the threshold region around the threshold SNR. MIE approximates MSE by dividing it into two parts. First part is for the global errors and it is estimated by using the interval error probabilities corresponding to the sidelobe angles. Second part is for the local errors and it is approximated by using CRB since MSE of ML converges to the CRB in the asymptotic region. In [27], pairwise error probabilities for deterministic signal model are given by

$$\begin{aligned}P_n =& Q\left(\sqrt{\frac{S}{2}\left(1-\sqrt{1-r_n^2}\right)}, \sqrt{\frac{S}{2}\left(1+\sqrt{1-r_n^2}\right)}\right) \\ &- e^{-\frac{S}{2}}\left\{I_0\left(\frac{r_kS}{2}\right) - \frac{1}{2^{2N-1}}I_0\left(\frac{r_nS}{2}\right)\sum_{m=0}^{N-1}\binom{2N-1}{m}\right. \\ &- \frac{1}{2^{2N-1}}\sum_{m=1}^{N-1}I_m\left(\frac{r_nS}{2}\right)\left[\left(\frac{1+\sqrt{1-r_n^2}}{r_n}\right)^m - \left(\frac{1-\sqrt{1-r_n^2}}{r_n}\right)^m\right] \\ &\left.\times \sum_{k=0}^{N-1-m}\binom{2N-1}{k}\right\}\end{aligned} \tag{5.11}$$

where $r_n = \left| \mathbf{a}^H(\phi_m)\,\mathbf{a}(\phi_n) \right| / M$ is the relative level of nth sidelobe,

$$S = \left(M/\sigma_e^2\right) \sum_{t=1}^{N} |s(t)|^2 \tag{5.12}$$

is the SNR, $I_m(\cdot)$ is the modified Bessel function of the first kind with order m and $Q(\cdot, \cdot)$ is the Marcum's Q function which is given by

$$Q(\alpha, \beta) = \int_{\beta}^{\infty} t e^{-\frac{\left(t^2 + \alpha^2\right)}{2}} I_0(\alpha t)\, dt \tag{5.13}$$

After finding the pairwise error probabilities, approximate MSE can be calculated as

$$\mathbf{C}_{\mathrm{MIE}}(\phi) = \left(1 - \sum_{k=1}^{N_s} P_k\right) \mathbf{C}_{\mathrm{CRB}}(\phi) + \sum_{k=1}^{N_s} P_k \left(\phi_k - \phi_m\right)^2 \tag{5.14}$$

where ϕ_m is the mainlobe angle, ϕ_k is the angle of kth sidelobe and N_s is the number of sidelobes. MIE is an MSE prediction method for MLE. For single source case, MLE reduces to the following expression,

$$\hat{\phi} \triangleq \arg\max_{\phi} \quad \mathbf{a}^H(\phi)\, \mathbf{R_y} \mathbf{a}(\phi) \tag{5.15}$$

which is equivalent to making a search over ϕ using Bartlett Beamformer spectrum.

A typical RMSE curve is shown in Figure 5.3 with the MIE curve. Maximum likelihood (ML) method is used as the DOA estimation method and sensor data is generated with the deterministic signal model with a single source.
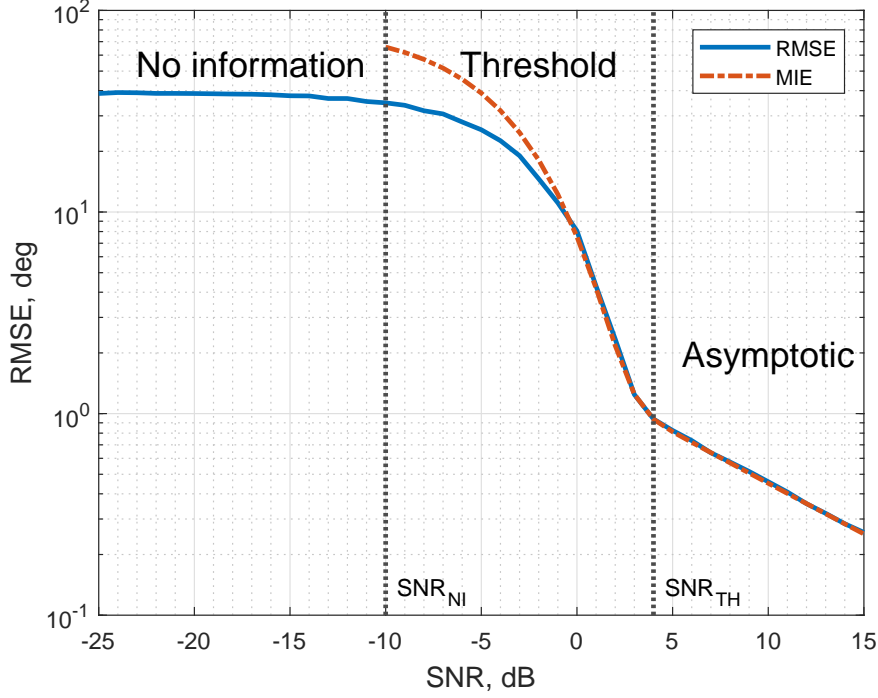
Figure 5.3: RMSE and CRB curves for DOA estimation of single source using deterministic signal model with 10 element ULA, $N = 1$, $N_{\mathrm{MTC}} = 10000$, $\phi = 90°$

$\mathbf{C}_{\mathrm{MIE}}(\phi)$ is also angle dependent as it is an approximate MSE for a deterministic parameter estimator (MLE). Bayesian approach that is used for CRB could also be applied to MIE. Bayesian MIE for a single source that has a uniform distribution $\mathrm{U}(\phi_l, \phi_r)$ is found as

$$\mathbf{C}_{\mathrm{BMIE}} = \frac{1}{\frac{1}{L} \sum_{k=1}^{L} \mathbf{C}_{\mathrm{MIE}}^{-1}(\phi_k)} \tag{5.16}$$

where L is the number of angles, $\phi_l = \phi_1$ is the lower bound and $\phi_r = \phi_L$ is the upper bound on the source angle distribution. Note that (5.16) is an MSE approximation for maximum aposteriori estimator (MAP) with a uniform prior distribution (which in turn is equivalent to MLE). Square root of the Bayesian MIE which can be denoted as $\mathrm{MIE}_{\mathrm{Bayesian}}$ will be used in the optimization problems in Chapter 6 to be able to compare with RMSE curves. $\mathrm{MIE}_{\mathrm{Bayesian}}$ can be found as

$$\begin{aligned} \mathrm{MIE}_{\mathrm{Bayesian}} &= \sqrt{\mathbf{C}_{\mathrm{BMIE}}} \\ &= \frac{1}{\sqrt{\frac{1}{L} \sum_{k=1}^{L} \mathbf{C}_{\mathrm{MIE}}^{-1}(\phi_k)}} \end{aligned} \tag{5.17}$$

5.2.4 Redundancy

Redundancy could be used as the cost function for array layout optimization. According to the definitions in 4.2.3 and 4.2.4, MRA and RMRA are obtained when the redundacy calculated with Equation 4.7 and used as the fitness value of the genetic algorithm. In addition to spatial efficiency in the difference coarray, larger aperture size is reached with minimum redundancy.

5.2.5 Fragility

Fragility could be used in the constraint function for array layout optimization. According to the definition in 4.2.4, RMRA is obtained when the fragility calculated with Equation 4.8 and used in the genetic algorithm. Fragility value should be equal to $2/M$ for RMRA layout optimization.

CHAPTER 6

SUBARRAY SELECTION OPTIMIZATION RESULTS

In this chapter, performance of different subarray layouts which are obtained with cost functions presented in Chapter 5 are compared. Angle accuracy in DOA estimation, detection and target separation performances are evaluated after finding 6 different subarrays (corresponding to each optimization problem with different cost functions) with the genetic algorithm. Results of the optimization for 16 sensors are given with optimum subarray layouts and performance graphs. Then, same procedure is repeated for subarrays that have more than 16 sensors. After presenting single subarrays, double subarray selections are shown with dual apodization being the DOA estimation method.

6.1 Three Octave Array

Octave array is a combination of multiple central nested ULAs with different element spacings [2]. It is mainly used in towed sonars that are designed for low frequency passive wideband processing. Desired operating frequency range is divided into multiple octaves and a different ULA is designed for upper frequency of the each octave. By central nesting the arrays for different design frequencies, some of the sensors are aligned with each other. Therefore, total number of sensors is less than sum of the sensors for each octave array. Number of octaves in the array can be decided by specifying the operating frequency range. As an example, the Five Octave Research Array (FORA) which is built by L-3 Chesapeake Sciences Corporation is designed to work between 50 - 3750 Hz [2]. In this thesis, a three octave array which is shown in Figure 6.1 is selected for the subarray layout optimization. There are three differ-

ent ULAs with cutoff design frequencies of 1, 2 and 4 kHz. There are 16 sensors in each of the octaves. As a result, total number of sensors in the whole array is 32. According to the classical DOA algorithms, only the *octave 3* is used for 4 kHz band as a narrowband processing. Aim of the array layout optimization whose results are shown in this chapter is to select sensors among all 32 sensors. Selection of sensors outside the *octave 3* increases the array aperture which narrows the beamwidth. A higher array gain could be obtained when the number of selected sensors is greater than 16 for high frequency band. Note that using more than 16 sensors of *octave 1* will not increase the directivity index in *octave 1* design frequency, since the aperture is critically sampled by this 16 sensors at this frequency. Three octave array is denoted by *TOA* throughout this chapter.
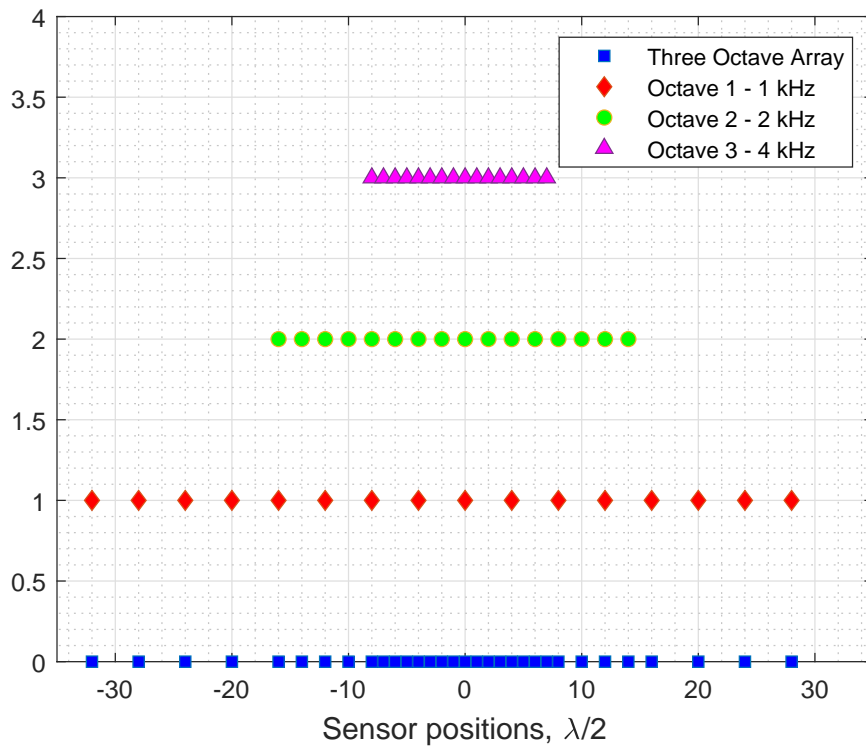
Figure 6.1: Sensor positions of three octave array

6.2 Performance Metrics For Optimization Results

Different subarray selections are shown in section 6.4 by using different cost functions in the genetic algorithm. In order to compare their performances, several Monte Carlo

(MTC) simulations are run and three different performance metrics are calculated; namely, RMS error (RMSE), probability of detection of all sources and probability of resolution.

Deterministic signal model is used in the MTC simulations for RMSE calculations. On the other hand, stochastic signal model is used for probability of detection and resolution calculations which require uncorrelated sources for DOA estimation methods. In deterministic case, source signal s takes constant value of $10^{\mathrm{SNR}/20}$ where SNR is the input signal to noise ratio in decibels (dB) and number of sources is 1. Since SNR defines the signal to noise ratio at each sensor, it is independent of the number of sensors and number of snapshots. In stochastic case, source signal s takes random value from Gaussian distribution $\mathcal{N}\left(0, 10^{\mathrm{SNR}/10}\right)$ and there are more than multiple uncorrelated sources. Noise signal in both cases takes values from a zero mean unit variance complex Gaussian distribution $\mathcal{CN}\left(0, 1\right) = \mathcal{N}\left(0, 1/\sqrt{2}\right) + j\mathcal{N}\left(0, 1/\sqrt{2}\right)$.

First performance metric is RMSE for angle estimation which can be defined as

$$\mathrm{RMSE} = \sqrt{\frac{1}{N_{\mathrm{MTC}}} \sum_{k=1}^{N_{\mathrm{MTC}}} \left(\phi_k - \hat{\phi}_k\right)^2} \tag{6.1}$$

where ϕ_k is the true source DOA, $\hat{\phi}_k$ is the estimated source DOA at k^{th} MTC simulation and N_{MTC} is the number of MTC simulations. Source DOA is estimated using MLE which reduces to the following expression for single source case,

$$\hat{\phi} \triangleq \arg\max_{\phi} \quad \mathbf{a}^{\mathrm{H}}\left(\phi\right) \mathbf{R_y} \mathbf{a}\left(\phi\right) \tag{6.2}$$

which is equivalent to making a search over ϕ using Bartlett Beamformer spectrum. For dual apodization method, source DOA is estimated in two steps. First step is finding the maximum point of dual apodization spectrum. Second step is finding the peak within a beamwidth of previously found DOA by searching the spectrum of subarray with larger aperture. Source DOA estimation for dual apodization can be shown as

$$\tilde{\phi} = \arg\max_{\phi} P_{\mathbf{DA}}\left(\phi\right)$$

$$\hat{\phi} = \arg\max_{\phi} P_{\mathbf{S1}}\left(\phi\right) \quad \phi \in \left[\tilde{\phi} - \phi_{hp}/2, \tilde{\phi} + \phi_{hp}/2\right] \tag{6.3}$$

where $P_{\mathbf{DA}}$ is the dual apodization spectrum, $P_{\mathbf{S1}}$ is the spectrum of subarray with larger aperture using Bartlett beamformer and ϕ_{hp} is the half-power beamwidth. Aim of this method is reducing the gross error detection rate caused by the high sidelobe levels. Second performance metric is the probability of detection which is calculated as

$$\mathrm{Pr}_d = \frac{1}{N_{\mathrm{MTC}}} \sum_{k=1}^{N_{\mathrm{MTC}}} d_k, \quad d_k = \begin{cases} 1 & \hat{P}_k = P \\ 0 & \hat{P}_k \neq P \end{cases} \tag{6.4}$$

where P is the true number of sources, $\hat{P}_k$ is the estimated number of sources at k^{th} MTC simulation and d_k is the success of detecting all sources. Method of Minimum description length (MDL) proposed in [49] is used for estimating the number of sources. It finds the number of sources by evaluating an eigenvalue dependent cost function with additional penalty term. In [28], MDL formula is given as

$$L(p) = N(M-p)\ln\left\{ \frac{\frac{1}{M-p}\sum_{k=p+1}^{M}\lambda_k}{\prod_{k=p+1}^{M}\lambda_k^{\frac{1}{M-p}}} \right\}$$
$$\hat{P}_{\mathrm{MDL}} = \arg\min_p \left\{ L(p) + \frac{1}{2}(p(2M-p)+1)\ln N \right\} \tag{6.5}$$

where $L(p)$ is the cost function, N is the number of snapshots, M is the number of sensors and $(\lambda_1 > \cdots > \lambda_P > \lambda_{P+1} = \cdots \lambda_M)$ are the eigenvalues of the sample covariance matrix. This method is applicable when DOA estimation is made over a single spatial spectrum such as Bartlett, MUSIC and SS-MUSIC. However, DOA estimation with dual apodization requires taking minimum of two spatial spectrums. It is not possible to estimate the number of sources from the sample covariance matrix in dual apodization method. Therefore, number of peaks can be estimated over the dual apodization spectrum by using Algorithm 3.

Algorithm 3 Number of source estimation algorithm for dual apodization method

---

1: Find all peaks in the spatial spectrum

2: Discard peaks outside the region $\bigcup_{k=1}^{P}(\phi_k + [-\phi_{hp}/2, \phi_{hp}/2])$ where ϕ_k is the true DOA of kth source, P is the number of sources and ϕ_{hp} is the half-power beamwidth

3: Discard peaks with a level smaller than $\mathrm{SNR} - 3$ dB

4: Number of remaining peaks is the source number estimation $\hat{P}_k$

Third performance metric is probability of resolution which is found as

$$\Pr_r = \frac{1}{N_{\text{MTC}}} \sum_{k=1}^{N_{\text{MTC}}} r_k, \quad r_k = \begin{cases} 1 & \hat{P}_k = 2 \\ 0 & \hat{P}_k \neq 2 \end{cases} \tag{6.6}$$

where $\hat{P}_k$ is the estimated number of sources at k^{th} MTC simulation using Algorithm 3 and r_k is the success of separating two close sources.

6.3 Computation Time Comparison

Bartlett beamformer, MUSIC, SS-MUSIC and dual apodization techniques are used as DOA estimation methods for comparing different optimum array layouts in this chapter. Computational complexity of a DOA estimator is an important criteria for many application areas such as radar and sonar systems. To operate in real-time without any delay, low cost methods are preferred due to the hardware specifications of the system. Computational complexity of a method could be defined in terms of the number of floating point operations (FLOP). A complex multiplication or a complex summation is counted as 1 FLOP [50]. In [51], it is stated that Bartlett beamformer requires $M^2(N+2) + M + 4PL$ FLOPs and MUSIC requires $\frac{5}{3}M^3 + M^2(N+P+1) + 4PL$ FLOPs. As a result, Bartlett beamformer has $O(M^2)$ and MUSIC has $O(M^3)$ complexity. Eigenvalue decomposition increases the order of complexity for MUSIC. A computation time comparison for Bartlett beamformer, MUSIC, SS-MUSIC and dual apodization methods are shown in Figure 6.2. Computation time is found by averaging the time measurements of 100000 MTC simulations using MATLAB R2020a under the environment of Intel Xenon E5-2620 CPU with the processor frequency 2.40 GHz and 64 GB RAM. Two different dual apodization configurations are used with $M_1 = M_2 = M$ and $M_1 = M$, $M_2 = 32$. Bartlett beamformer has the lowest complexity, whereas SS-MUSIC has the highest computation time since it uses $O(M^2)$ virtual elements instead of $O(M)$ sensors. Computation time required for dual apodization technique is approximately twice of the time for Bartlett beamformer. It requires less computation for $M > 18$ when it is compared with MUSIC and SS-MUSIC.
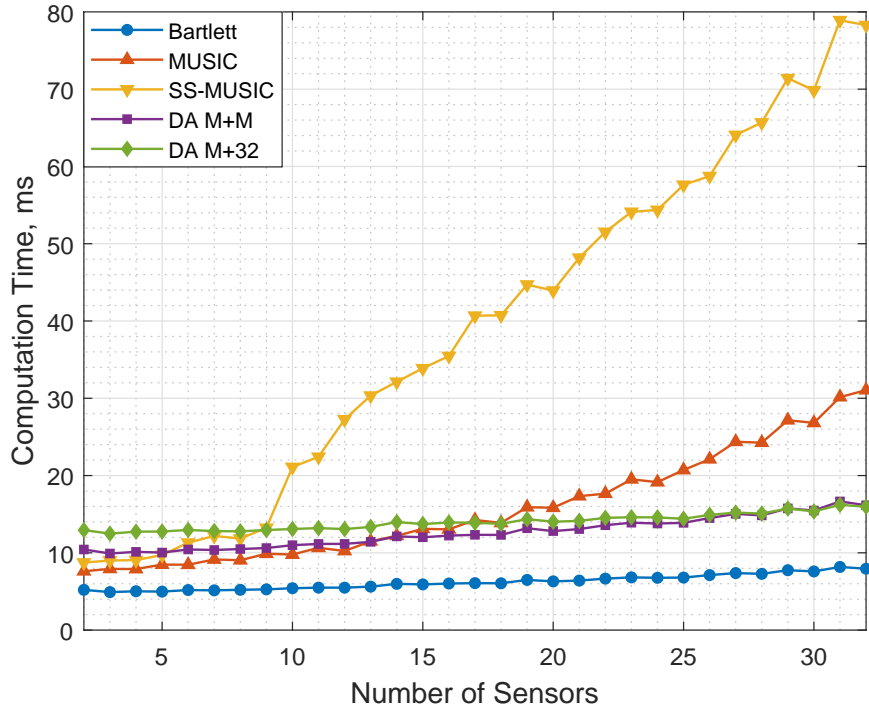
Figure 6.2: Computation times for Bartlett, MUSIC, SS-MUSIC and dual apodization methods with $P = 1$, $N = 1$, $N_{\mathrm{MTC}} = 100000$

6.4 Array Layout Optimization Results For 16 Sensors

In classical octave array processing, only 16 sensor *octave 3* in TOA is used for an operating frequency of 4 kHz. Number of sensors for DOA estimation might be limited to 16 sensors as a system design criteria for not exceeding a pre-determined computation time. By considering the fixed number of sensor constraint, optimization problems with different cost functions are proposed for selecting 16 sensors across the TOA. Layouts obtained as a result of the optimizations are shown and selected sensor positions are compared with the TOA. In addition, some of the array properties such as beampatterns, PSL values for different steering angles, RMSE curves and coarray weights are given.

68

6.4.1 PSL Optimization

Obtaining PSLs for different steering angles below a selected level is the first optimization problem for selecting 16 sensors. For linear arrays, sidelobe levels are increasing when the array is steered towards the end points which are called end fires. End fire angles are chosen as $0°$ and $180°$ in this thesis. In Figure 6.3c, PSL values for different angles are shown for ULA with 16 sensors. PSL increases rapidly for $\phi < 25°$ and $\phi > 155°$. Selecting different layouts for a linear array does not change this behaviour significantly. Therefore, optimization of PSL values are restricted for steering angles between $\phi_l = 30°$ and $\phi_r = 150°$. Main aim is to minimize the maximum PSL for steering angles $\phi_l \leq \phi \leq \phi_r$. This minimax optimization problem could be constructed as

$$
\begin{aligned}
\mathbb{S}_{\text{PSL}} &\triangleq \arg \min_{\mathbb{S}} \max \quad \text{PSL}_\phi \\
\text{s.t.} \quad |\mathbb{S}| &= M \\
\phi &\in [\phi_l, \phi_r]
\end{aligned}
\tag{6.7}
$$

where PSL_ϕ is calculated by using Equation 5.3. There are two ways for minimizing PSL values. One option is selecting a layout with narrower aperture. As a result of having narrower aperture, larger beamwidth is obtained. However, minimum aperture is obtained with 16 sensor ULA when the number of desired sensor is 16. Since it is the default layout for the highest frequency band, no improvement could be obtained in terms of PSL values. Second option is selecting a sparse layout whose aperture is larger than 16 sensor ULA. First sidelobes of ULA have the highest sidelobe levels which are around -13,5 dB. In order to minimize PSL, levels of first sidelobes should be minimized when the remaining sidelobe levels are less than or equal to the first sidelobe levels. By choosing elements outside the ULA at the center, levels of first sidelobes which are PSL levels could be minimized.

In Figure 6.3a, sensor positions of selected array layout are shown with red markers in addition to the TOA with blue markers. Selected array layout is similar to the ULA except for its rightmost elements. Beampatterns for the selected layout and 16 sensor ULA are shown for the steering angle $\phi_0 = 90°$ in Figure 6.3b. Maximum sidelobe levels are obtained at the first sidelobes around the mainobe. It is seen that maximum sidelobe level decreases from -13 dB to around -16 dB. However, other sidelobe levels

are higher than the ones in ULA.

In Figure 6.3c, PSL values for steering angles $0° \leq \phi \leq 180°$ are shown for the selected layout with red dash-dot line. Maximum sidelobe levels for $30° \leq \phi_0 \leq 150°$ are around -16 dB. Although levels seem to be constant between $30°$ and $150°$, decimal differences exist between the values for different steering angles. With this optimization, lower sidelobe levels are obtained for different steering angles while preserving the beamwidth.
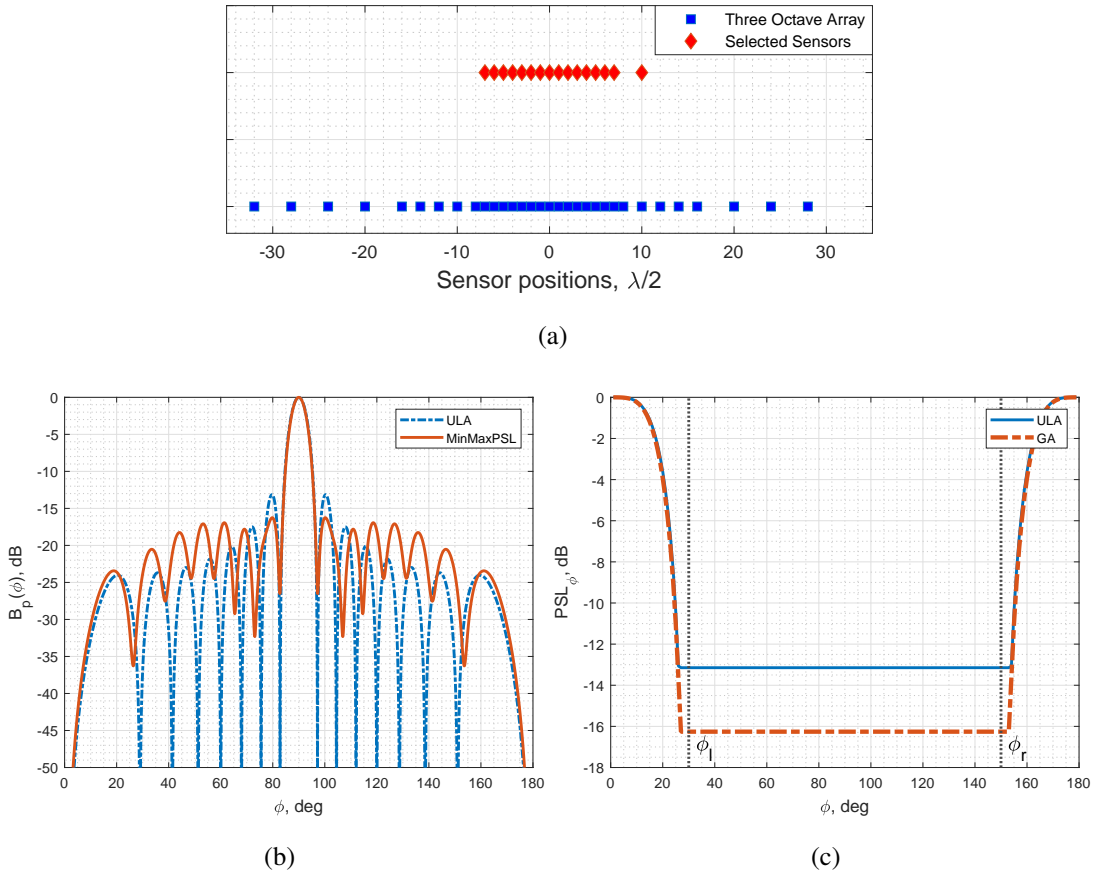

(a)

(b)

(c)

Figure 6.3: (a) Selected sensor positions for minimax PSL optimization, (b) beam-pattern for ULA and MinMaxPSL, (c) PSL levels for different steering angles with $M = 16$, $\phi_l = 30°$, $\phi_r = 150°$

6.4.2 Bayesian CRB Optimization

Minimizing the Bayesian CRB for a selected SNR value is the second optimization problem for selecting 16 sensors. As it is mentioned in 5.2.2, lower threshold SNR is a desired property for DOA estimation since source SNR might be low in practice. By selecting a layout with lower sidelobe levels, ambiguity due to the gross errors could be minimized. Lower threshold can be obtained as a result of reduced gross errors. In Figure 6.4b, RMSE curve of 16 sensor ULA is shown with blue markers and threshold SNR is 2 dB. To obtain a lower threshold SNR, bayesian CRB optimization is made for $\mathrm{SNR} = 0$ dB. Then, the optimization problem for minimum Bayesian CRB can be stated as

$$
\begin{aligned}
\mathbb{S}_{\mathrm{CRB}} &\triangleq \arg\min_{\mathbb{S}} \quad \mathrm{CRB}_{\mathrm{Bayesian}}\left(\mathrm{SNR}\right) \\
\text{s.t.} \quad |\mathbb{S}| &= M \\
\mathrm{SNR} &= \mathrm{SNR}_{\mathrm{opt}} \\
\phi &\sim U\left[\phi_l, \phi_r\right]
\end{aligned}
\tag{6.8}
$$

where $\mathrm{SNR}_{\mathrm{opt}} = 0$ dB, $\phi_l = 30°$, $\phi_r = 150°$ and $\mathrm{CRB}_{\mathrm{Bayesian}}$ is calculated by using Equation 5.10. In Figure 6.4a, sensor positions of selected array layout are shown with red markers in addition to the TOA with blue markers. Minimum CRB is obtained with larger array aperture. As the aperture increases, beamwidth of the array gets narrower and the RMS error in the asymptotic region decreases as a result of increased resolution. With the fixed number of sensors constraint, the optimization chooses the outermost elements among the all sensors. Using the outermost elements and having an empty region at the center result in grating lobes in the beampattern (using Bartlett beamformer) because of the sparsity. Having grating lobes in the beampattern increases the gross errors and threshold SNR is not minimized as a result.

In Figure 6.4b, beampatterns of the 16 sensor ULA and the selected array for $\phi_0 = 90°$ are shown. Grating lobes and high sidelobe levels can be observed for the selected layout. RMSE and Bayesian CRB curves are shown in Figure 6.4c. Because of the grating lobes, two peaks with the same level are observed in the spatial spectrum for the selected array. DOA estimation algorithm that is used for generating the RMSE curve selects the first peak with the same level in cas eof more than one peak. First

peak appears near the end fire angles $0°$ - $180°$ due to the grating lobes. However, true source DOA can be between $\phi_l = 30°$ and $\phi_r = 150°$. Therefore, RMS errors for the selected array stay nearly the constant for the whole SNR region in Figure 6.4c.

(a)

(b)

(c)
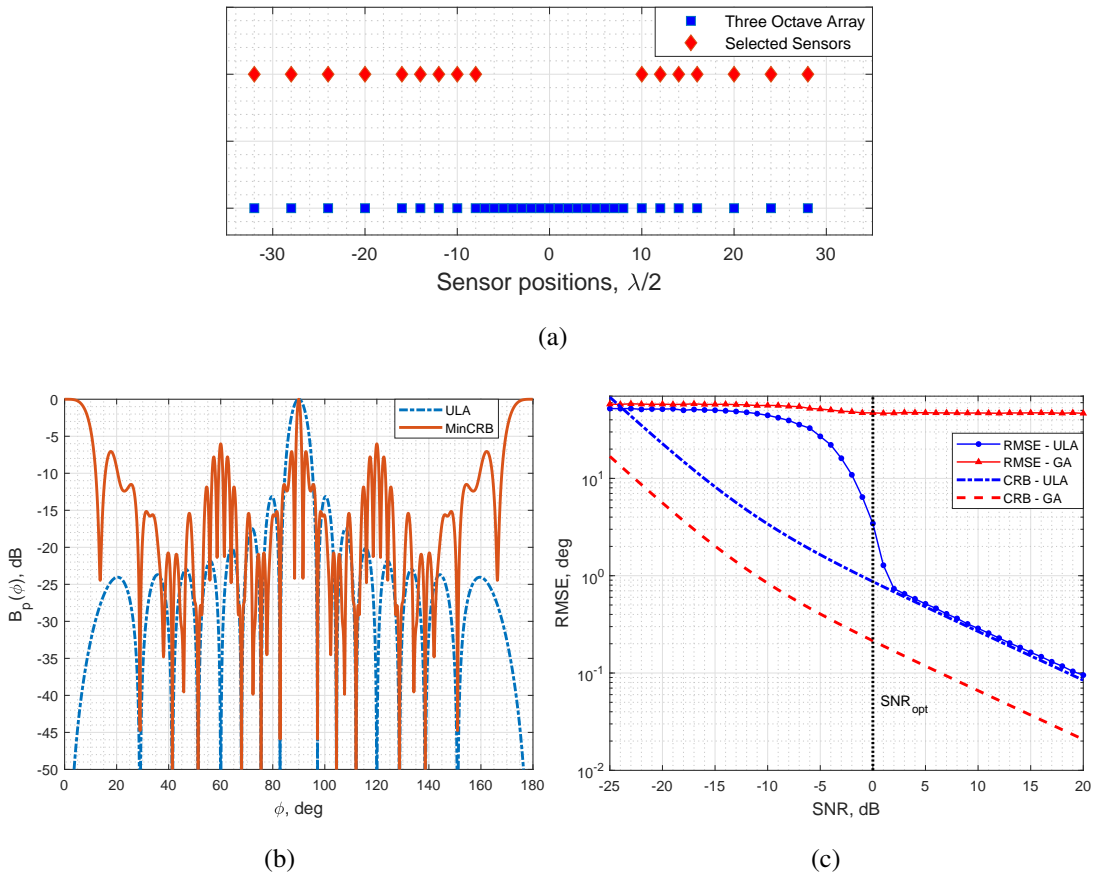
Figure 6.4: (a) Selected sensor positions for minimum Bayesian CRB optimization, (b) beampattern for ULA and MinCRB, (c) RMSE - SNR for Bartlett method using ULA and array selected by GA (min CRB) with $M = 16$, $\mathrm{SNR_{opt}} = 0$ dB, $P = 1$, $N = 1$, $N_{\mathrm{MTC}} = 10000$, $\phi_l = 30°$, $\phi_r = 150°$. Note that RMSE of GA selected array does not converge to its CRB. The reason for this is the fact that the GA selected array has grating lobes (see Figure 6.4b). This in turn results in gross errors and causes a bias even in high SNR region. Consequently our estimator is biased hence deterministic CRB is not reached.

6.4.3 Bayesian CRB Optimization with PSL Constraint

In previous subsection 6.4.2, it is found that minimizing Bayesian CRB with a fixed number of sensors causes grating lobes in the array beampattern. To solve this issue, a PSL constraint is added into the Bayesian CRB optimization problem. Main target is preventing the grating lobes by selecting an array whose sidelobes are below the threshold point. Then, the optimization problem for obtaining minimum Bayesian CRB with PSL constraint can be stated as

$$
\begin{aligned}
\mathbb{S}_{\mathrm{CRB}} &\triangleq \arg\min_{\mathbb{S}} \quad \mathrm{CRB}_{\mathrm{Bayesian}} \\
\text{s.t.} \quad |\mathbb{S}| &= M \\
\mathrm{SNR} &= \mathrm{SNR}_{\mathrm{opt}} \\
\max\left(\mathrm{PSL}_\phi\right) &\leq \mathrm{PSL}_{\mathrm{max}} \\
\phi &\in [\phi_l, \phi_r]
\end{aligned}
\tag{6.9}
$$

where $\mathrm{SNR}_{\mathrm{opt}} = 0$ dB, $\mathrm{PSL}_{max} = -13$ dB, $\phi_l = 30°$, $\phi_r = 150°$, $\mathrm{CRB}_{\mathrm{Bayesian}}$ and PSL_ϕ are calculated by using Equation 5.10 and 5.3 respectively. This optimization problem can be viewed as a combination of the problems in Equation 6.7 and 6.8. $\mathrm{PSL}_{\mathrm{max}}$ is selected as -13 dB to obtain the PSL of a ULA in the worst case. Without PSL constraint, optimization tries to select outermost 16 elements to minimize beamwidth of the selected layout. By having a narrower beamwidth, local errors are minimized due to the mainlobe. Having a PSL constraint forces the optimization to select a narrower aperture to reduce sidelobe levels and wider beamwidth is obtained as a result. Minimization of CRB with a PSL contraint results in a new layout with narrower aperture than MinCRB and wider aperture than ULA.

In Figure 6.5a, sensor positions of selected array layout are shown with red markers in addition to the TOA with blue markers. With the PSL constraint, outermost elements are not selected. In comparison to ULA, a wider aperture is obtained. In Figure 6.5b, beampatterns of the 16 sensor ULA and the selected array for $\phi_0 = 90°$ are shown. A narrower beamwidth is obtained with the sidelobe levels around -13 dB. In Figure 6.5c, PSL values for steering angles $0° \leq \phi \leq 180°$ are shown for the selected layout with red dash-dot line. Maximum sidelobe levels for $30° \leq \phi_0 \leq 150°$ are around -13 dB with decimal differences between the values for different steering angles. RMSE and Bayesian CRB curves are shown in Figure 6.5d. In comparison with ULA, both

73

threshold SNR and the Bayesian CRB at 0 dB are not minimized despite of having less RMS errors in the asymptotic region.

(a)

(b)

(c)

(d)
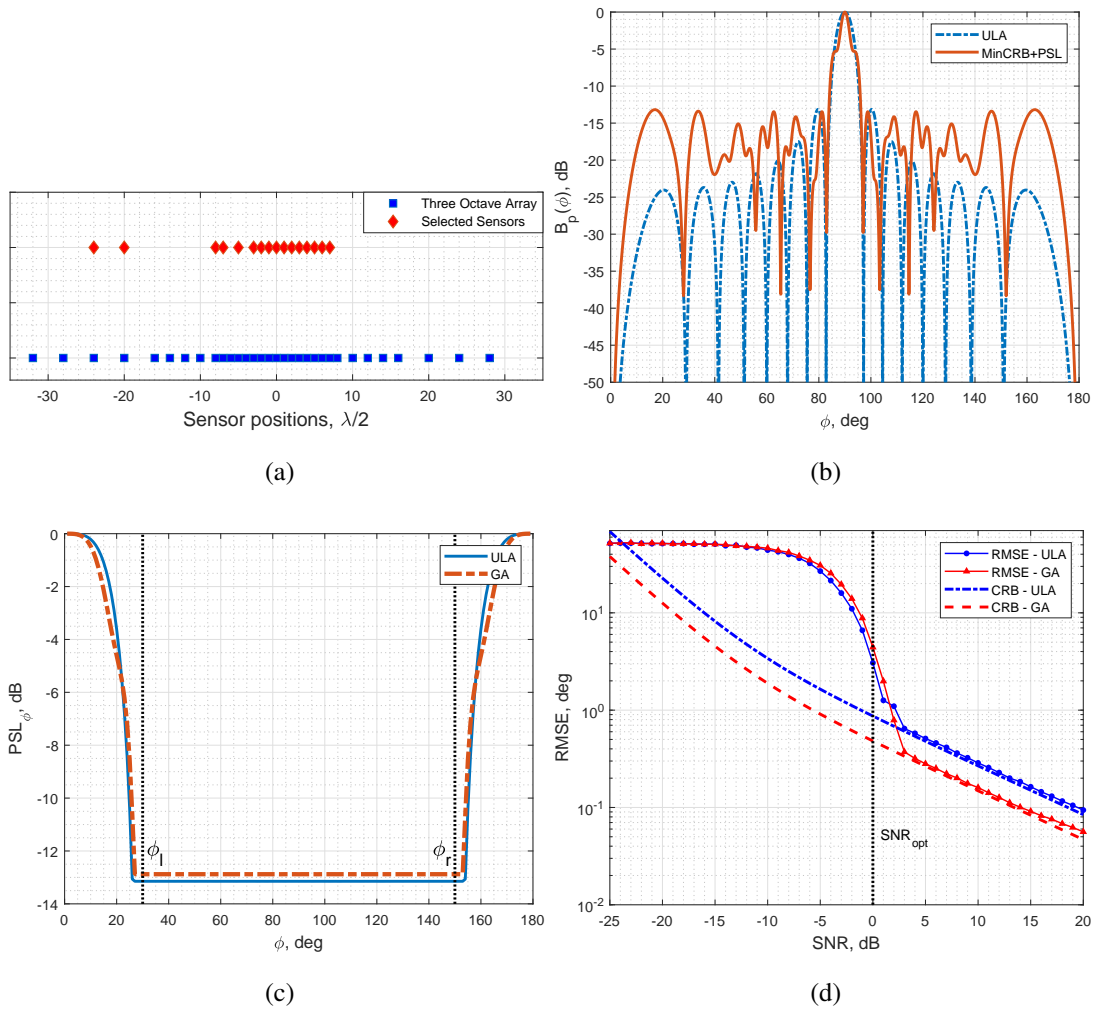
Figure 6.5: (a) Selected sensor positions for minimum Bayesian CRB optimization with PSL constraint, (b) beampattern for ULA and MinCRB+PSL, (b) PSL levels for minimum Bayesian CRB optimization with PSL constraint, (d) RMSE - SNR for Bartlett method using ULA and array selected by GA (min CRB with PSL constraint) with $M = 16$, $\text{SNR}_{\text{opt}} = 0\,\text{dB}$, $P = 1$, $N = 1$, $N_{\text{MTC}} = 10000$, $\phi_l = 30°$, $\phi_r = 150°$, $\text{PSL}_{\text{max}} = -13\,\text{dB}$

74

6.4.4 Bayesian MIE Optimization

Minimizing the Bayesian MIE for a selected SNR value is the fourth optimization problem for selecting 16 sensors. As it is mentioned in 5.2.3, RMSE curve can be approximated with MIE. Then, the optimization problem for minimum Bayesian MIE can be stated as

$$
\begin{aligned}
\mathbb{S}_{\mathrm{MIE}} &\triangleq \arg\min_{\mathbb{S}} \quad \mathrm{MIE}_{\mathrm{Bayesian}}\,(\mathrm{SNR}) \\
\text{s.t.} \quad |\mathbb{S}| &= M \\
\mathrm{SNR} &= \mathrm{SNR}_{\mathrm{opt}} \\
\phi &\sim U\,[\phi_l, \phi_r]
\end{aligned}
\tag{6.10}
$$

where $\mathrm{SNR}_{\mathrm{opt}} = 0$ dB, $\phi_l = 30°$, $\phi_r = 150°$ and $\mathrm{MIE}_{\mathrm{Bayesian}}$ is calculated by using Equation 5.17. Minimization of MIE at 0 dB corresponds to minimization of gross errors caused by sidelobes since selected SNR value lies within the threshold region of RMSE curve. MIE approximates threshold region with interval error probabilities P_n which can be calculated using Eqaution 5.11. Interval error probability P_n could be minimized by minimizing relative sidelobe levels r_n. Highest RMS errors are obtained for first sidelobes since they are the nearest sidelobes to the mainlobe. Therefore, optimization tries to select a layout with lower sidelobe levels.

In Figure 6.6a, sensor positions of selected array layout are shown with red markers in addition to the TOA with blue markers. Selected array layout is similar to the ULA except for the double Nyquist distance between its fourth and fifth elements. Beampatterns for the selected layout and 16 sensor ULA are shown for the steering angle $\phi_0 = 90°$ in Figure 6.6b. Beamwidth of the selected array is similar to the one in the ULA due to layout similarity. First sidelobes of the selected layout is less than the ULA although there is not any significant difference. Since the available sensor positions are fixed, optimization makes a selection similar to ULA. In Figure 6.6c, RMSE, Bayesian CRB and Bayesian MIE curves are shown for the selected array and 16 sensor ULA. There is not any meaningful difference between the RMSE and Bayesian MIE curves. Because of the similarities between two layouts, their RMSE - SNR performances are indistinguishable.
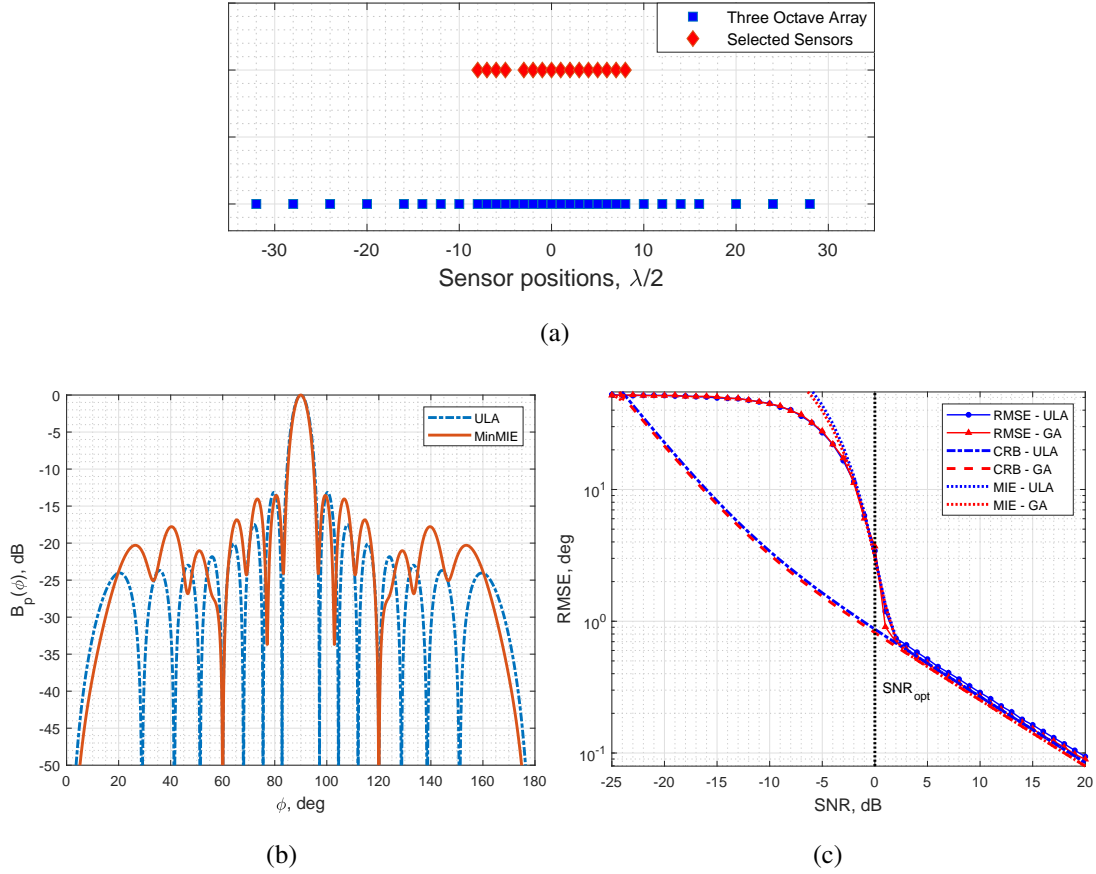
Figure 6.6: (a) Selected sensor positions for minimum Bayesian MIE optimization, (b) beampattern for ULA and MinMIE, (c) RMSE - SNR for Bartlett method using ULA and array selected by GA (min MIE) with $M = 16$, $\text{SNR}_{\text{opt}} = 0$ dB, $P = 1$, $N = 1$, $N_{\text{MTC}} = 10000$, $\phi_l = 30°$, $\phi_r = 150°$

6.4.5 Minimum Redundancy Optimization

Minimizing the redundancy is the fifth optimization problem for selecting 16 sensors. Unlike previous optimization problems, it is independent of the beampattern and the beamwidth. Main aim is to reduce the number of same distances between the array elements. In [15], the optimization problem for minimum redundancy is given as

$$
\begin{aligned}
\mathbb{S}_{MRA} &\triangleq \arg\min_{\mathbb{S}} \quad R \\
\text{s.t.} \quad |\mathbb{S}| &= M \\
\mathbb{D} &= \mathbb{U}
\end{aligned}
\tag{6.11}
$$

where R is calculated by using Equation 4.7 and $\mathbb{D} = \mathbb{U}$ means that difference coarray $\mathbb{D}$ is hole-free. When the number of sensors is fixed, central ULA length $|\mathbb{U}|$ in the difference coarray increases as the redundancy decreases according to Equation 4.7. With this information, optimization problem in Equation 6.11 can be reconstructed as

$$
\begin{aligned}
\mathbb{S}_{MRA} &\triangleq \arg\max_{\mathbb{S}} \quad |\mathbb{U}| \\
\text{s.t.} \quad |\mathbb{S}| &= M
\end{aligned}
\tag{6.12}
$$

Aim of minimum redundancy optimization is selecting a layout with maximum spatial efficiency of sensor placement. Difference coarray weight function for three octave array is shown in Figure 6.8b. Central ULA segment of the difference coarray is between $-40\lambda/2$ and $40\lambda/2$. Therefore, maximum obtainable aperture length is $40\lambda/2$ for minimum redundancy array selection. As a result, optimization tries to select 16 sensors with an aperture of $40\lambda/2$.

In Figure 6.7a, sensor positions of selected array layout are shown with red markers in addition to the TOA with blue markers. Leftmost element of the TOA is selected in the new array layout to increase the aperture. Difference coarray weight functions for 16 sensor ULA, three octave array and the selected array are shown in Figure 6.8a, 6.8b and 6.7c respectively. Redundancy of ULA is 8 and central ULA length $|\mathbb{U}|$ is 31. Redundancy of three octave array is 12,4 and central ULA length $|\mathbb{U}|$ is 81. Redundancy of the selected layout is 3 and central ULA length $|\mathbb{U}|$ is 81. It is seen that redundancy of the selected array is less than redundancies of ULA and three octave array and maximum possible central ULA length is obtained.

In Figure 6.7b, beampatterns for MRA obtained with the optimization are shown when the array is steered to $90°$. Beampattern using Bartlett beamformer is plotted with blue dash-dots and the one for spatially smoothed difference coarray is plotted with red line. Lower sidelobe levels are observed with the PSL being -13 dB since the beamforming is done by using the coarray elements.

Figure 6.7: (a) Selected sensor positions for minimum redundancy optimization, (b) beampattern using Bartlett and Spatially Smoothed Coarray for MRA, (c) weight function of difference coarray for MRA with $M = 16$
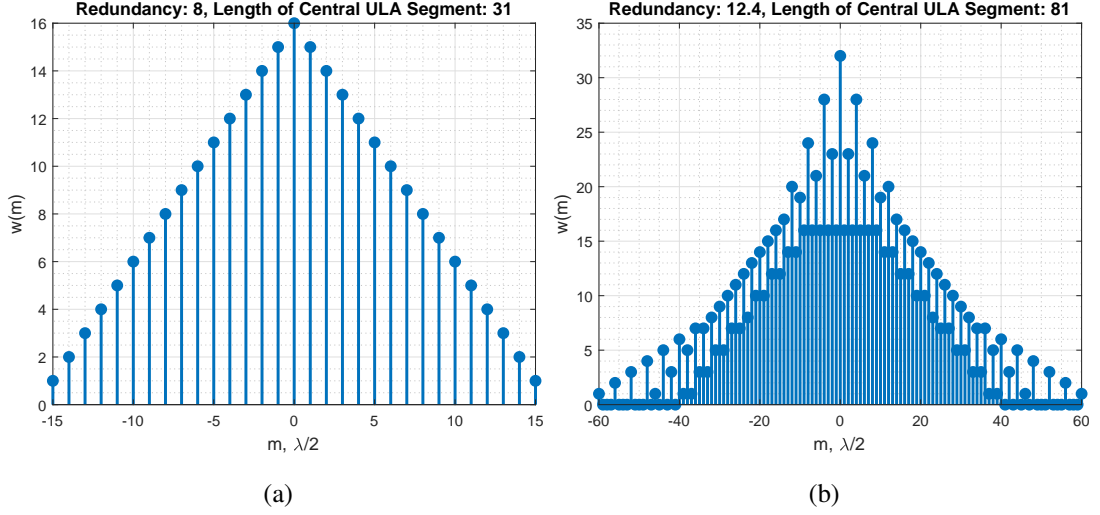
Figure 6.8: Weight function of difference coarray for (a) ULA with $M = 16$ and (b) three octave array (TOA)

Optimization problem in Equation 6.12 becomes computationally difficult as the number of sensors increase. One option might be searching a point using only half of the TOA for reducing the search area since it is symmetric around the origin. Then, the optimization problem can be written as

$$
\begin{aligned}
\bar{\mathbb{S}}_{MRA} &\triangleq \arg\max_{\bar{\mathbb{S}}} \quad |\mathbb{U}| \\
\text{s.t.} \quad |\bar{\mathbb{S}}| &= \frac{M}{2} \\
\mathbb{S} &= \left\{ \bar{\mathbb{S}}\left[\frac{M}{2} : -1 : 1\right], \bar{\mathbb{S}}\left[1 : 1 : \frac{M}{2}\right] \right\}
\end{aligned}
\tag{6.13}
$$

In Figure 6.9a, sensor positions of selected array layout are shown with red markers in addition to the TOA with blue markers. Aperture of the new layout is smaller than the one shown in Figure 6.7a. Difference coarray weight function for the new array is shown in Figure 6.9b. Redundancy of the new array is higher and the central ULA length is smaller. According to this result, symmetrical element layout assumption does not provide a better solution in terms of redundancy and central ULA length. Searching an optimum point by using all TOA elements gives a better solution despite of slower convergence and high computational cost.

(a)   (b)
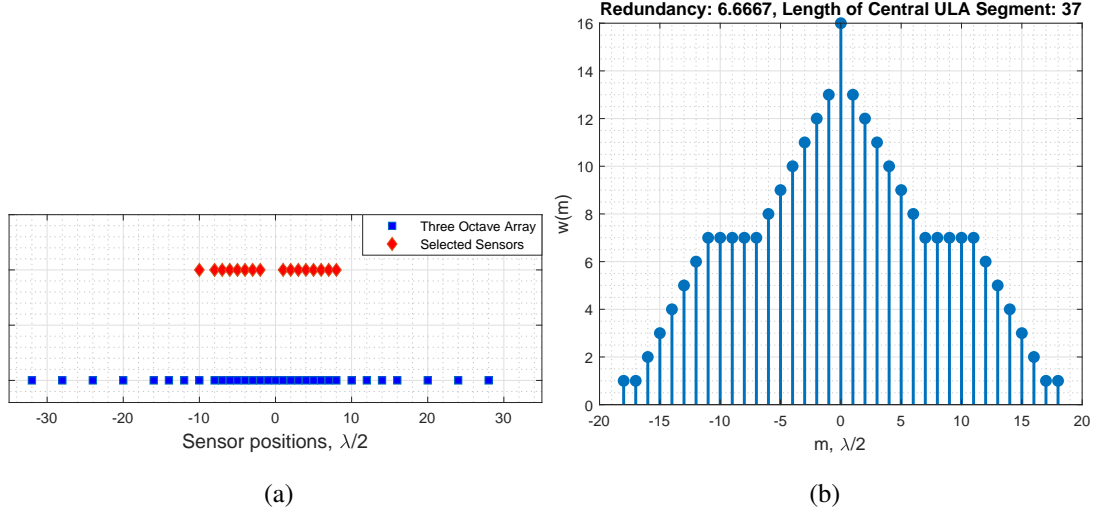
Figure 6.9: (a) Selected sensor positions for minimum redundancy optimization with reduced dimension, (b) weight function of difference coarray for 16 element MRA selected with reduced dimension optimization

6.4.6 Robust Minimum Redundancy Optimization

Robust minimum redundancy is the fifth optimization problem for selecting 16 sensors. In addition to the minimum redundancy optimization in Equation 6.11, there is a fragility constraint that forces the selected array as robust as ULA against sensor failure. In [15], the optimization problem for robust minimum redundancy is given as

$$
\begin{aligned}
\mathbb{S}_{RMRA} \triangleq \underset{\mathbb{S}}{\arg\min} \quad & R \\
\text{s.t.} \quad |\mathbb{S}| &= M \\
\mathbb{D} &= \mathbb{U} \\
F &= \tfrac{2}{M} \\
M &\geq 4
\end{aligned}
\tag{6.14}
$$

where R is calculated by using Equation 4.7, F is calculated by using Equation 4.8 and $\mathbb{D} = \mathbb{U}$ means that difference coarray $\mathbb{D}$ is hole-free. There is a tradeoff between central ULA length of difference coarray and robustness against sensor failure. Using the constraint of having two essential sensors and fixed sensor positions forces the optimization to select a layout similar to ULA.
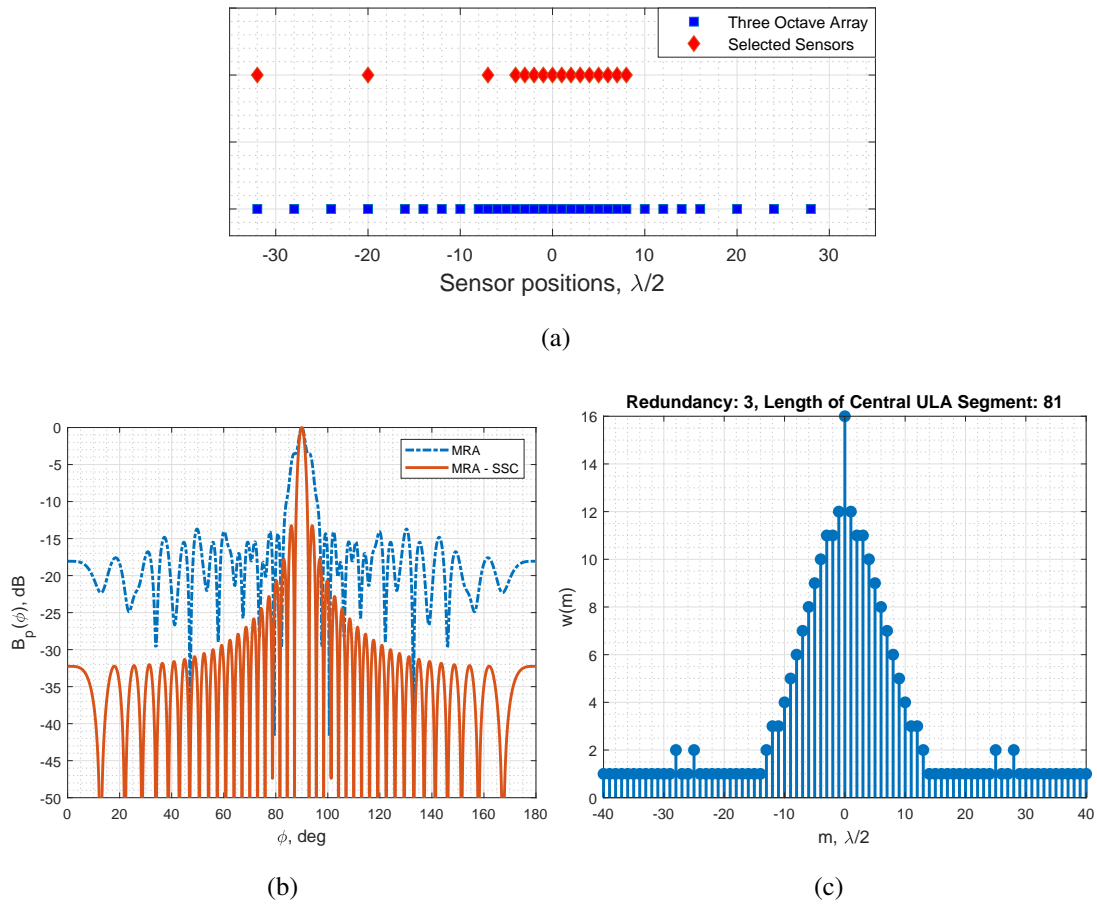
80
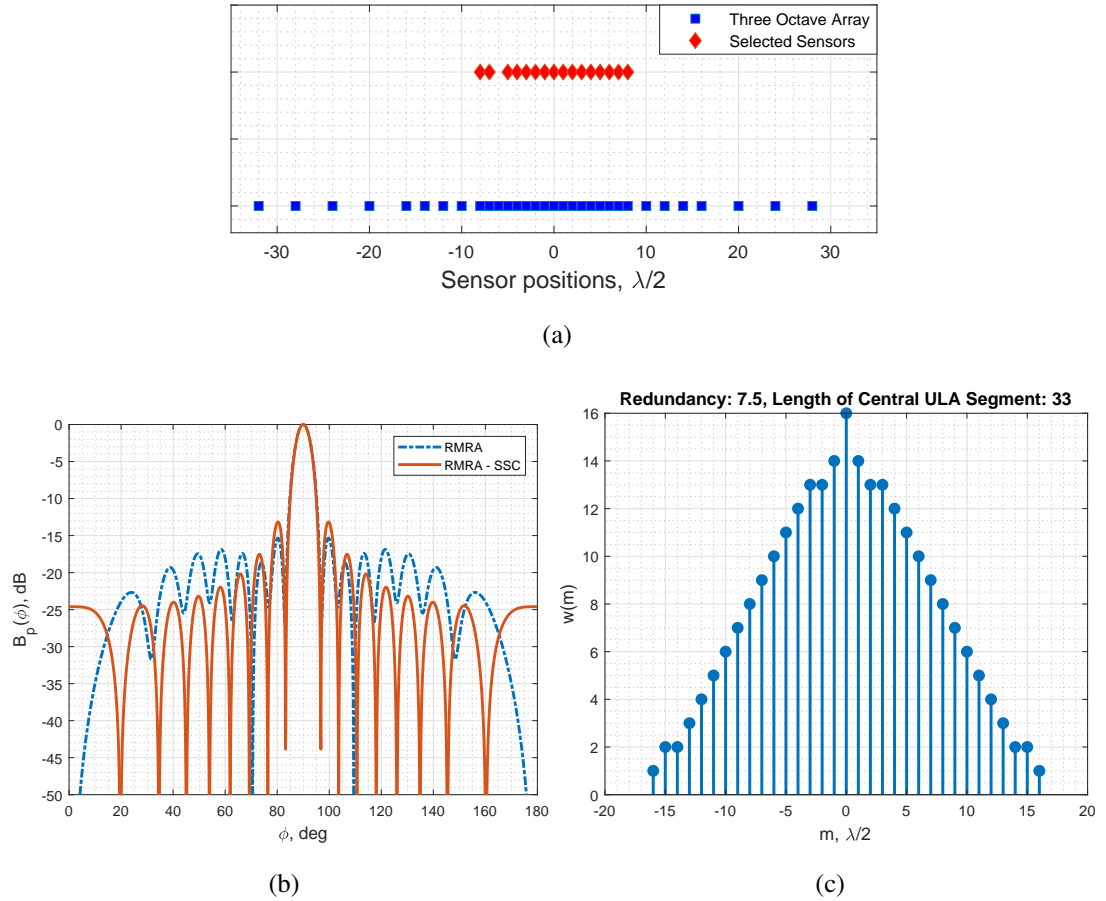
Figure 6.10: (a) Selected sensor positions for robust minimum redundancy optimization, (b) beampattern using Bartlett and Spatially Smoothed Coarray for RMRA, (c) weight function of difference coarray for RMRA with $M = 16$

In Figure 6.10a, sensor positions of selected array layout are shown with red markers in addition to the TOA with blue markers. Resultant array is very similar to 16 sensor ULA except for the gap between second and third elements. Difference coarray weight function for the selected array are shown in Figure 6.10c. Redundancy of the selected layout is 7,5 and central ULA length $|\mathbb{U}|$ is 33. By comparing with 16 sensor ULA, there is a little improvement in terms of redundancy and central ULA length. In Figure 6.10b, beampatterns for RMRA obtained with the optimization are shown when the array is steered to $90°$. Beampattern using Bartlett beamformer is plotted with blue dash-dots and the one for spatially smoothed difference coarray is plotted with red line. PSL of the spatially smoothed coarray is higher than PSL of

81

the beampattern generated with Bartlett method, whereas the beamwidths are close to each other.

6.5   Performance Comparison of the Arrays Found by Optimization (M=16)

Array layout optimization results with 16 sensors for different cost functions are provided in section 6.4. Proposed array layouts and 16 sensor ULA are compared in terms of DOA estimation method, DOF and aperture length in Table 6.1. Bartlett beamformer is used for DOA estimation for all of the arrays in the table except for MRA and RMRA. SS-MUSIC is preferred for MRA and RMRA to use the advantages of coarray processing.

Table 6.1: Number of sensors (M), DOA estimation methods, DOFs and aperture lengths and computation times for different arrays with 16 sensors

Array Type	M	Method	DOF	Aperture ($\lambda/2$)	Time (ms)
ULA	16	Bartlett	16	15	6,03
MinMaxPSL	16	Bartlett	16	17	6,03
MinCRB	16	Bartlett	16	60	6,03
MinCRB + PSL	16	Bartlett	16	31	6,03
MinMIE	16	Bartlett	16	16	6,03
MRA	16	SS-MUSIC	41	20	35,47
RMRA	16	SS-MUSIC	17	8	35,47

With classical techniques such as Bartlett, DOF of an array is equal to the number of sensors. Therefore, DOF of arrays except for MRA and RMRA is 16 and these arrays can detect up to 15 sources. It is expected that arrays which use coarray techniques have more DOFs such as MRA and RMRA. DOFs of MRA and RMRA are 81 and 33 in the coarray domain. However, spatial smoothing is applied for SS-MUSIC and the DOFs are reduced to 41 and 17 as a result of the size reduction in the difference coarrays. Aperture lengths in the table are given as a multiple of Nyquist distance $\lambda/2$ for 4 kHz. Apertures of MRA and RMRA are 40 and 16 according to Figures 6.7a and

6.10a. But, they are reduced to 20 and 8 after smoothing the array for SS-MUSIC. Minimum aperture in Table 6.1 is 8 and belongs to RMRA, whereas maximum aperture is 60 for the array obtained with minimum CRB optimization. Throughout this section, arrays obtained in 6.4.1, 6.4.2, 6.4.3, 6.4.4, 6.4.5, 6.4.6 are denoted by Min-MaxPSL, MinCRB, MinCRB+PSL, MinMIE, MRA and RMRA respectively.
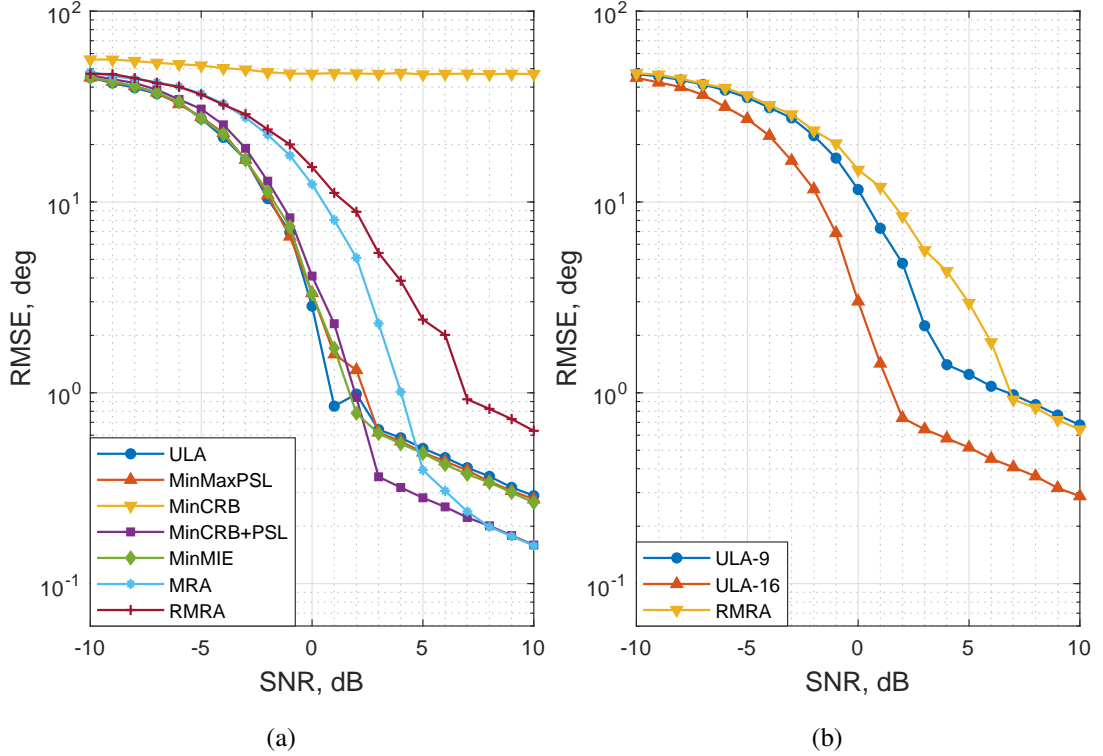
Figure 6.11: RMSE - SNR for (a) ULA and arrays selected by GA with $M = 16$, (b) 16 sensor RMRA and ULAs using 9 and 16 sensors with $P = 1$, $N = 1$, $N_{\mathrm{MTC}} = 10000$, $\phi_l = 30°$, $\phi_r = 150°$

In Figure 6.11a, array layouts with 16 sensors are compared by calculating RMSE of the angle estimations as a function of SNR for $N = 1$ snapshot, $P = 1$ source, averaged over $N_{\mathrm{MTC}} = 10000$ simulations using deterministic signal model. In each MTC simulation, source DOA is selected randomly from uniform distribution between $\phi_l = 30°$ and $\phi_r = 150°$. MinCRB+PSL and MRA have the best performances in the asymptotic region, whereas RMRA and MinCRB have the worse performances according to their RMSE values. Since MinCRB has an empty area in the middle, errors due to the grating lobes make the RMSE values high for all SNR regions. DOA

estimation errors in the asymptotic region are caused by the errors due to the main-lobe. As the array aperture increases, beamwidth of the array narrows and errors due to the mainlobe decreases. Thus, it is expected to see less RMSE in DOA estimation with the arrays with large aperture. Because of having the minimum aperture length, RMRA has a poor performance when it is compared with other arrays. Min-MaxPSL, MinMIE and ULA have similar performances due to close aperture lengths. Minimum threshold SNR is obtained with MinCRB+PSL and its value is 3 dB. Min-CRB+PSL is the optimum selection among all arrays with lower RMS errors and ability to work at lower SNR values.

Aperture of RMRA can be found as 16 by looking at Figure 6.10a. Also, its number of elements in its difference coarray is 33. However, spatial smoothing halves these values. It is known that RMRA can detect upto 16 sources when SS-MUSIC technique is used. But, aperture of the array is not increased with using coarray based DOA estimation techniques. In Figure 6.11b, RMSE-SNR performance of RMRA is compared with ULAs using 9 and 16 sensors. It is seen that RMSE values of RMRA is similar to the results for 9 sensor ULA whose aperture length is 8. Since the virtual aperture of the difference coarray does not affect the real aperture and the physical aperture is halved after spatial smoothing, aperture length of RMRA is also 8.

In Figure 6.12a, probability of detection is estimated as a function of SNR for given arrays using $N = 1000$ snapshots and stochastic signal model. There are $P = 9$ sources at $\{30°, 45°, 60°, 75°, 90°, 105°, 120°, 135°, 150°\}$. Equation 6.4 is used for estimating the probability of detection with source number estimation using MDL method. Probabilities are calculated by averaging the results of $N_{\mathrm{MTC}} = 10000$ simulations. Detection performances of all arrays increase with increasing SNR and equal to 1 after some point. MRA has the best detection performance because it can operate at lower SNR values with high probabiliy of detection. MinMIE performs relatively worse than the others since it can reach probability of 1 when the SNR is 0 dB.

Figure 6.12: Probability of detection of all sources as a function of SNR for ULA and arrays selected by GA using $M = 16$, $N = 1000$, $N_{\mathrm{MTC}} = 10000$ for (a) $P = 9$ sources with DOA Angles $= \{30°, 45°, 60°, 75°, 90°, 105°, 120°, 135°, 150°\}$, (b) $P = 16$ sources with DOA Angles $= \{30°, 40°, 50°, 60°, 67°, 74°, 80°, 86°, 94°, 100°, 106°, 113°, 120°, 130°, 140°, 150°\}$

In Figure 6.13a, probability of detection is estimated as a function of snapshots for given arrays using $\mathrm{SNR} = 0$ dB and the remaining simulation parameters are same with the ones used for Figure 6.12a. Detection performances of all arrays increase rapidly with increasing number of snapshots. MRA and RMRA have lower probability of detection when the number of snapshots is below 150 because SS-MUSIC requires more snapshots than classical methods such as Bartlett beamformer. Despite of rapid increase at the beginning, detection performance of MinMIE converges to unit probability slower than other arrays. ULA, MinMaxPSL and MinCRB+PSL perform similar to each other. Due to the empty region at the center, MinCRB fails to detect all sources for all snapshot values.

DOFs of MRA and RMRA are higher than the other arrays whose DOFs are 16. According to Table 6.1, arrays other than MRA and RMRA can detect upto 15 sources. For the case of 16 sources, only MRA and RMRA are capable of detect all sources. In Figures 6.12b and 6.13b, probability of detecting 16 sources are given as a function of SNR and number of snapshots, respectively. Sources are placed at $\{30°, 40°, 50°, 60°, 67°, 74°, 80°, 86°, 94°, 100°, 106°, 113°, 120°, 130°, 140°, 150°\}$ and probabilites are calculated by using $N_{\mathrm{MTC}} = 10000$ simulations. As observed, only MRA and RMRA can detect 16 sources due to their DOFs.

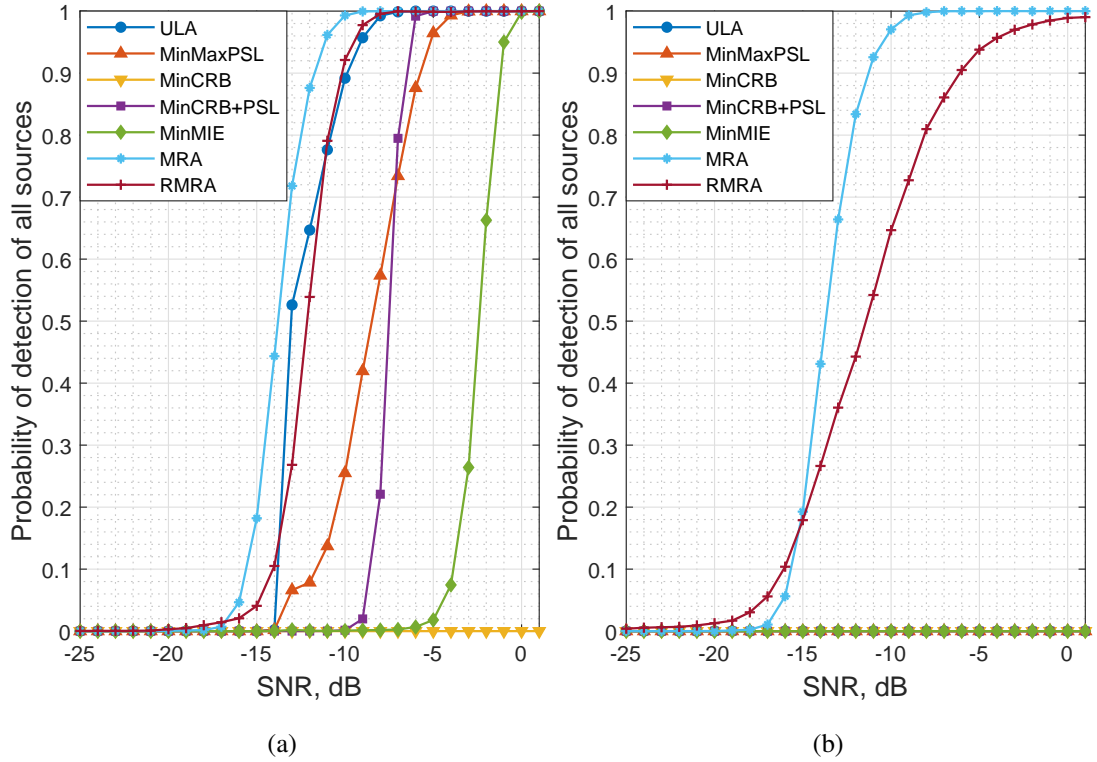(a)   (b)

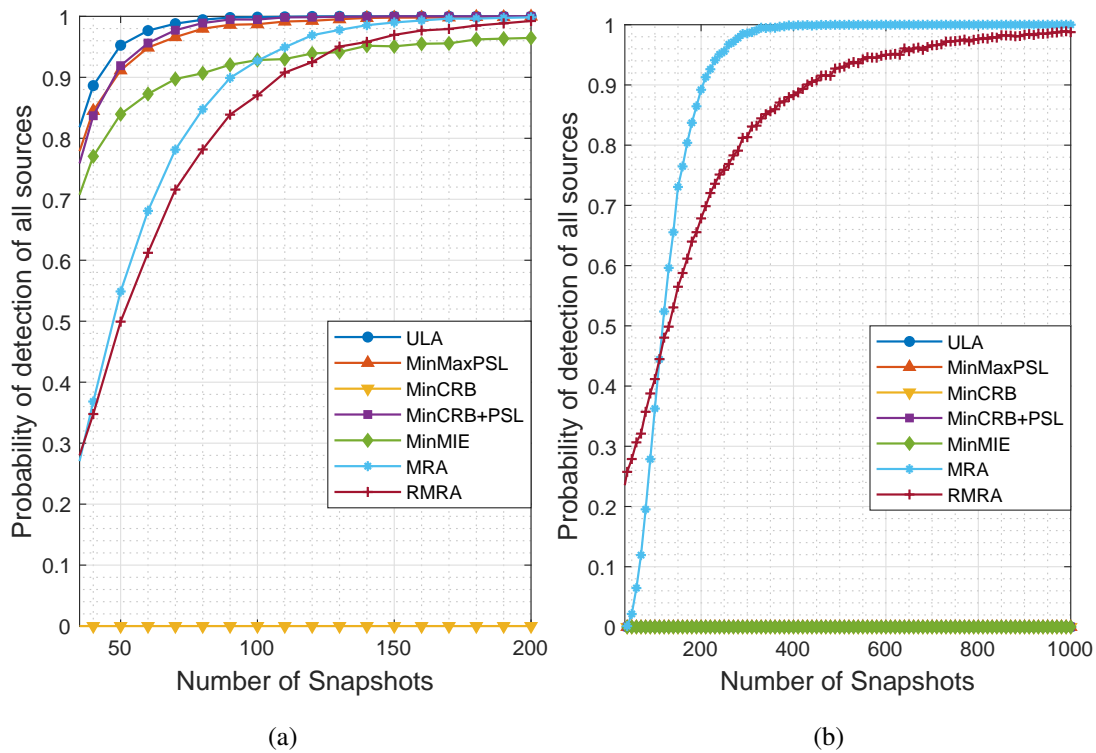Figure 6.13: Probability of detection of all sources as a function of number of snapshots for ULA and arrays selected by GA using $M = 16$, SNR $= 0$ dB, $N_{\mathrm{MTC}} = 10000$ for (a) $P = 9$ sources with DOA Angles $= \{30°, 45°, 60°, 75°, 90°, 105°, 120°, 135°, 150°\}$, (b) $P = 16$ sources with DOA Angles $= \{30°, 40°, 50°, 60°, 67°, 74°, 80°, 86°, 94°, 100°, 106°, 113°, 120°, 130°, 140°, 150°\}$

86
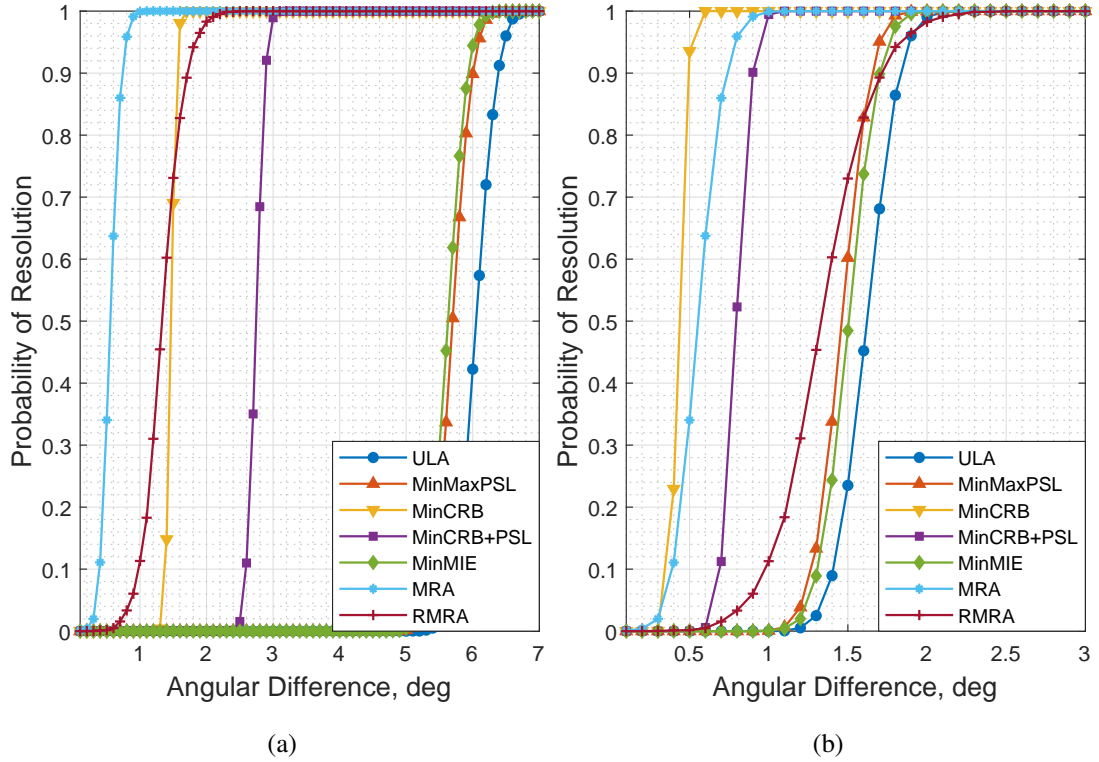
Figure 6.14: Probability of resolving two sources for ULA and arrays selected by GA with $M = 16$, $P = 2$, $N = 100$, $\text{SNR} = 10$ dB, $N_{\text{MTC}} = 10000$ when subarrays other than MRA and RMRA using (a) Bartlett beamformer and (b) MUSIC

In Figure 6.14a, probability of resolving two sources is shown as a function of angular difference between DOAs of the sources using stochastic source model. Equation 6.6 is used for calculating the probability of resolution with $\text{SNR} = 10$ dB, $N = 100$ snapshots and $N_{\text{MTC}} = 10000$ simulations. Longer aperture increases resolution of an array to separate closed sources. As a consequence of similar aperture lengths, resolution performances of ULA, MinMaxPSL and MinMIE are close to each other. Because of using whole aperture of the TOA, MinCRB has a good resolution performance. MinCRB+PSL has an average performance of resolving two closed sources. MRA shows the best performance with the ability to detect two sources with $1°$ angular difference. MRA and RMRA are used with SS-MUSIC method which is a superresolution DOA estimation algorithm. Superresolution techniques are capable of detecting two sources with an angular difference lower than the beamwidth. Despite of having an aperture length of 31, MinCRB+PSL performs worse than RMRA

whose physical aperture length is 16. In Figure 6.14b, MUSIC technique is used as a DOA estimation method for the arrays other than MRA and RMRA. In this case, MinCRB+PSL outperforms RMRA due to having longer aperture.

According to results presented in this section, MRA outperforms other arrays with lower RMS error, detection of low SNR sources and higher resolution for target separation. Drawbacks of this array is requiring more snapshots and higher computational cost. MinCRB+PSL is also an optimum solution when Bartlett beamformer is used as the DOA estimation method. MinCRB is the worst array layout because of the grating lobe related problems.

6.6 Array Layout Optimization Results For More Than 16 Sensors

In section 6.4, number of sensors is restricted to 16 for array layout optimizations. Data from more than 16 sensors can be processed unless there is a limit on the computation time or the hardware. Array gain increases when more sensors are selected by the optimization since it is proportionate to the number of used sensors. In this section ,optimization problems in section 6.4 are modified for selecting $M > 16$ sensors and the obtained layouts are shown. In addition, some of the array properties such as beampatterns, PSL values for different steering angles, RMSE curves and coarray weights are given.

6.6.1 PSL Optimization

In order to find an optimum array for more than 16 sensors, number of sensors constraint in optimization problem given by Equation 6.7 is replaced with $|\mathbb{S}| > M$. Then, minimax optimization problem with the new constraint could be constructed as

$$
\begin{aligned}
\mathbb{S}_{\mathrm{PSL}} &\triangleq \arg \min_{\mathbb{S}} \max \quad \mathrm{PSL}_{\phi} \\
\text{s.t.} \quad |\mathbb{S}| &> M \\
\phi &\in [\phi_l, \phi_r]
\end{aligned}
\tag{6.15}
$$

where $M = 16$, $\phi_l = 30°$, $\phi_r = 150°$ and PSL_{ϕ} is calculated by using Equation 5.3. PSL values could be minimized by selecting a layout with narrower aperture and

88

lower first sidelobe levels.

In Figure 6.15a, sensor positions of selected array layout are shown with red markers in addition to the TOA with blue markers. Selected array layout resembles ULA for including 16 sensor ULA at the center. In order to select narrower aperture, 18 sensors at the center are selected. Beampatterns for the selected layout and 16 sensor ULA are shown for the steering angle $\phi_0 = 90°$ in Figure 6.15b. It is seen that maximum sidelobe level decreases from -13 dB to around -16,5 dB. However, sidelobe levels located at $\phi < 64°$ and $\phi > 116°$ are higher than the ones in ULA. Gaps at the leftmost and rightmost parts of the layout reduces the first sidelobe levels and increases remaining sidelobe levels.
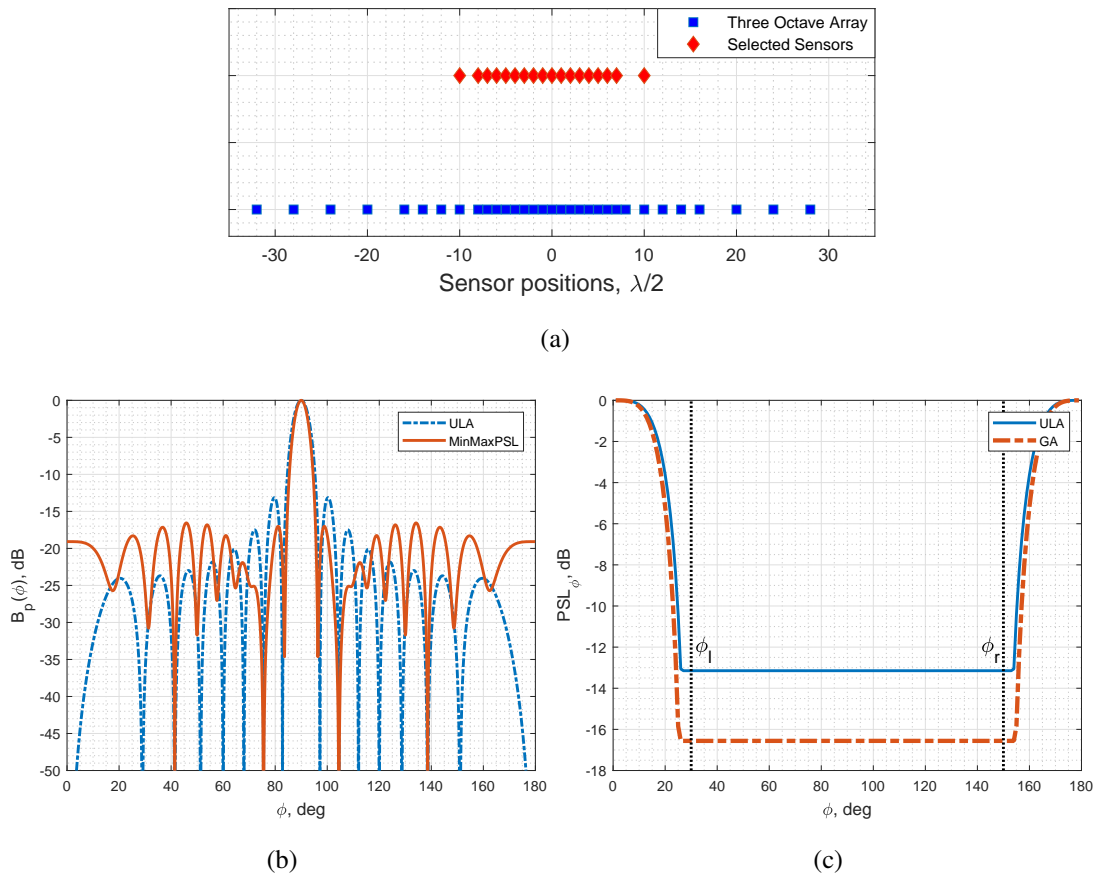

(a)

(b)

(c)

Figure 6.15: (a) Selected sensor positions for minimax PSL optimization, (b) beampattern for ULA with $M = 16$ and MinMaxPSL with $M = 18$, (c) PSL levels for different steering angles with $\phi_l = 30°$, $\phi_r = 150°$

In Figure 6.15c, PSL values for steering angles $0° \leq \phi \leq 180°$ are shown for the selected layout with red dash-dot line. Maximum sidelobe levels for $30° \leq \phi_0 \leq 150°$ are around -16,5 dB. Although levels seem to be constant between $30°$ and $150°$, decimal differences exist between the values for different steering angles. With this optimization, lower sidelobe levels are obtained for different steering angles using 18 sensors. Selecting more than 18 sensors increases the sparsity of the layout, which will increase the sidelobe levels.

6.6.2   Bayesian CRB Optimization

In order to find an optimum array for more than 16 sensors by minimizing Bayesian CRB, number of sensors constraint in optimization problem given by Equation 6.8 is replaced with $|\mathbb{S}| > M$. Then, minimum Bayesian CRB optimization problem with the new constraint can be stated as

$$
\begin{aligned}
\mathbb{S}_{\text{CRB}} &\triangleq \arg\min_{\mathbb{S}} \quad \text{CRB}_{\text{Bayesian}}\left(\text{SNR}\right) \\
&\text{s.t.} \quad |\mathbb{S}| \ > \ M \\
&\qquad\ \text{SNR} \ = \ \text{SNR}_{\text{opt}} \\
&\qquad\quad\ \phi \ \sim \ U\left[\phi_l, \phi_r\right]
\end{aligned}
\tag{6.16}
$$

where $M = 16$, $\text{SNR}_{\text{opt}} = 0$ dB, $\phi_l = 30°$, $\phi_r = 150°$ and $\text{CRB}_{\text{Bayesian}}$ is calculated by using Equation 5.10. Aim of this optimization is obtaining a lower threshold SNR to be able to work at lower SNR values. Threshold SNR can be minimized by maximizing array gain which is proportional to the number of sensors. In Figure 6.16a, sensor positions of selected array layout are shown with red markers in addition to the TOA with blue markers. As a result of relaxing the fixed number of sensors constraint, optimization chooses all elements of the TOA. By choosing all elements, maximum aperture length is reached and array gain is maximized.

Figure 6.16: (a) Selected sensor positions for minimum Bayesian CRB optimization, (b) beampattern for ULA with $M = 16$ and MinCRB with $M = 32$, (c) RMSE - SNR for Bartlett method using 16 sensor ULA and 32 sensor MinCRB with $\mathrm{SNR_{opt}} = 0$ dB, $P = 1$, $N = 1$, $N_{\mathrm{MTC}} = 10000$, $\phi_l = 30°$, $\phi_r = 150°$

In Figure 6.16b, beampatterns of the 16 sensor ULA and the selected array for $\phi_0 = 90°$ are shown. High sidelobes are observed for the selected layout as a result of being a sparse array. RMSE and Bayesian CRB curves are shown in Figure 6.16c. Using an aperture length of 60 decreases the RMS errors in the asymptotic region. Also, threshold SNR of the selected array layout is 1 dB less than the one for 16 sensor ULA.

6.6.3 Bayesian CRB Optimization with PSL Constraint

In order to find an optimum array for more than 16 sensors by minimizing Bayesian CRB with a given PSL, number of sensors constraint in optimization problem given by Equation 6.9 is replaced with $|\mathbb{S}| > M$. Then, minimum Bayesian CRB with the desired PSL optimization problem with the new constraint can be stated as

$$\mathbb{S}_{\text{CRB}} \triangleq \arg\min_{\mathbb{S}} \quad \text{CRB}_{\text{Bayesian}}$$

$$
\begin{aligned}
\text{s.t.} \qquad |\mathbb{S}| &> M \\
\text{SNR} &= \text{SNR}_{\text{opt}} \\
\max\left(\text{PSL}_\phi\right) &\leq \text{PSL}_{\text{max}} \\
\phi &\in [\phi_l, \phi_r]
\end{aligned}
\qquad (6.17)
$$

where $M = 16$, $\text{SNR}_{\text{opt}} = 0$ dB, $\text{PSL}_{\text{max}} = -13$ dB, $\phi_l = 30°$, $\phi_r = 150°$, $\text{CRB}_{\text{Bayesian}}$ and PSL_ϕ are calculated by using Equation 5.10 and 5.3 respectively. This optimization problem can be viewed as a combination of the problems in Equation 6.15 and 6.16. PSL_{max} is selected as -13 dB to obtain the PSL of a ULA in the worst case. Without PSL constraint, optimization tries to select all 32 elements to minimize beamwidth and maximize array gain of the selected layout. By having a narrower beamwidth, local errors are minimized due to the mainlobe. High sidelobes are observed when all elements of three octave array are selected. Having a PSL constraint forces the optimization to select a narrower aperture to reduce sidelobe levels and wider beamwidth is obtained as a result. Minimization of CRB with a PSL constraint results in a new layout with narrower aperture than MinCRB.

In Figure 6.17a, sensor positions of selected array layout are shown with red markers in addition to the TOA with blue markers. With the PSL constraint, all elements are not selected like MinCRB. In comparison to ULA, a wider aperture is obtained. In Figure 6.17b, beampatterns of the 16 sensor ULA and the selected array for $\phi_0 = 90°$ are shown. A narrower beamwidth is obtained with the sidelobe levels around -13 dB. In Figure 6.17c, PSL values for steering angles $0° \leq \phi \leq 180°$ are shown for the selected layout with red dash-dot line. Maximum sidelobe levels for $30° \leq \phi_0 \leq 150°$ are around -13 dB with decimal differences between the values for different steering angles. RMSE and Bayesian CRB curves are shown in Figure 6.17d. In comparison with ULA, both Bayesian CRB and RMSE at 0 dB is not minimized despite of lower RMSE values for $\text{SNR} > 0$ dB.
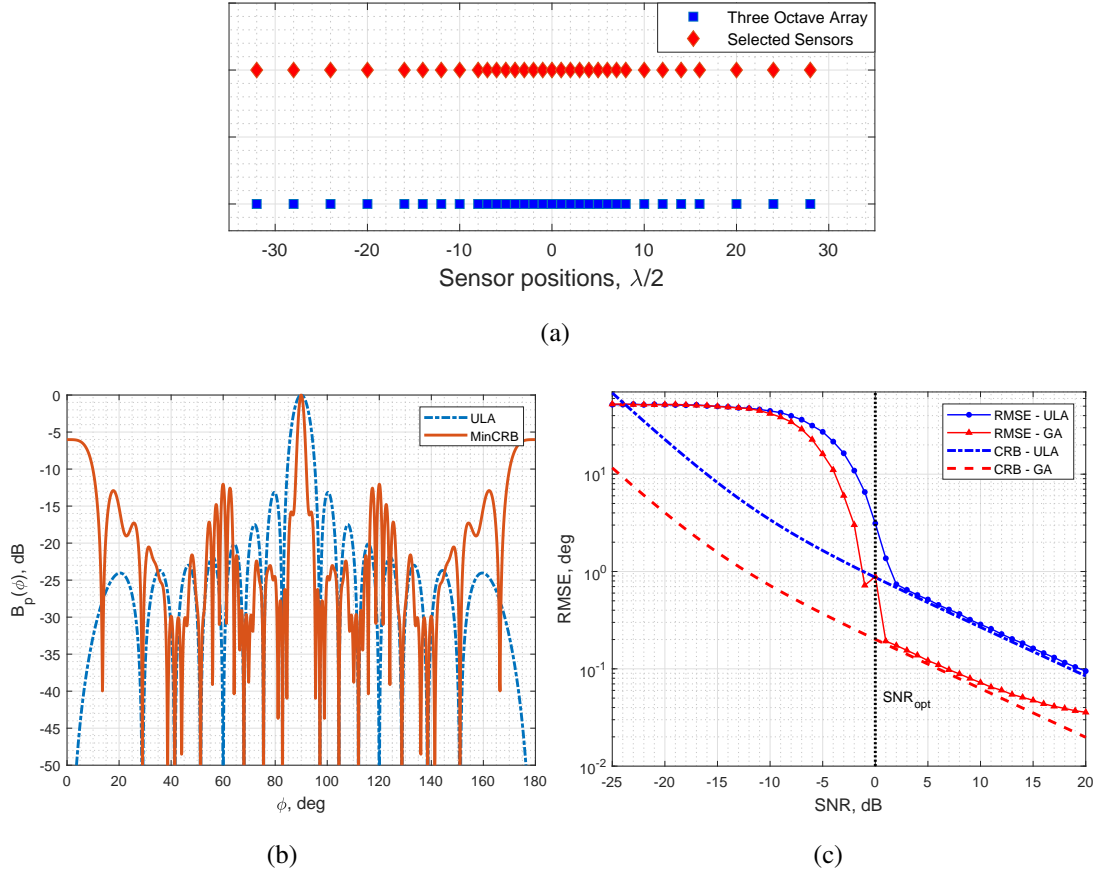
Figure 6.17: (a) Selected sensor positions for minimum Bayesian CRB optimization with PSL constraint, (b) beampattern for ULA with $M = 16$ and MinCRB+PSL with $M = 20$, (c) PSL levels for minimum Bayesian CRB optimization with PSL constraint, (d) RMSE - SNR for Bartlett method using 16 sensor ULA and 20 sensor MinCRB+PSL with $\text{SNR}_{\text{opt}} = 0$ dB, $P = 1$, $N = 1$, $N_{\text{MTC}} = 10000$, $\phi_l = 30°$, $\phi_r = 150°$

6.6.4 Bayesian MIE Optimization

In order to find an optimum array for more than 16 sensors by minimizing Bayesian MIE, number of sensors constraint in optimization problem given by Equation 6.10 is replaced with $|\mathbb{S}| > M$. Then, minimum Bayesian MIE optimization problem with

the new constraint can be stated as

$$\mathbb{S}_{\text{MIE}} \triangleq \underset{\mathbb{S}}{\arg\min} \quad \text{MIE}_{\text{Bayesian}}(\text{SNR})$$
$$\text{s.t.} \quad |\mathbb{S}| > M$$
$$\text{SNR} = \text{SNR}_{\text{opt}} \tag{6.18}$$
$$\phi \sim U[\phi_l, \phi_r]$$

where $M = 16$, $\text{SNR}_{\text{opt}} = 0$ dB, $\phi_l = 30°$, $\phi_r = 150°$ and $\text{MIE}_{\text{Bayesian}}$ is calculated by using Equation 5.17. MIE approximates RMSE by combining CRB and interval error probabilities. Without fixed number of sensors constraint, optimization maximizes array gain to decrease CRB by selecting all sensors of three octave array.
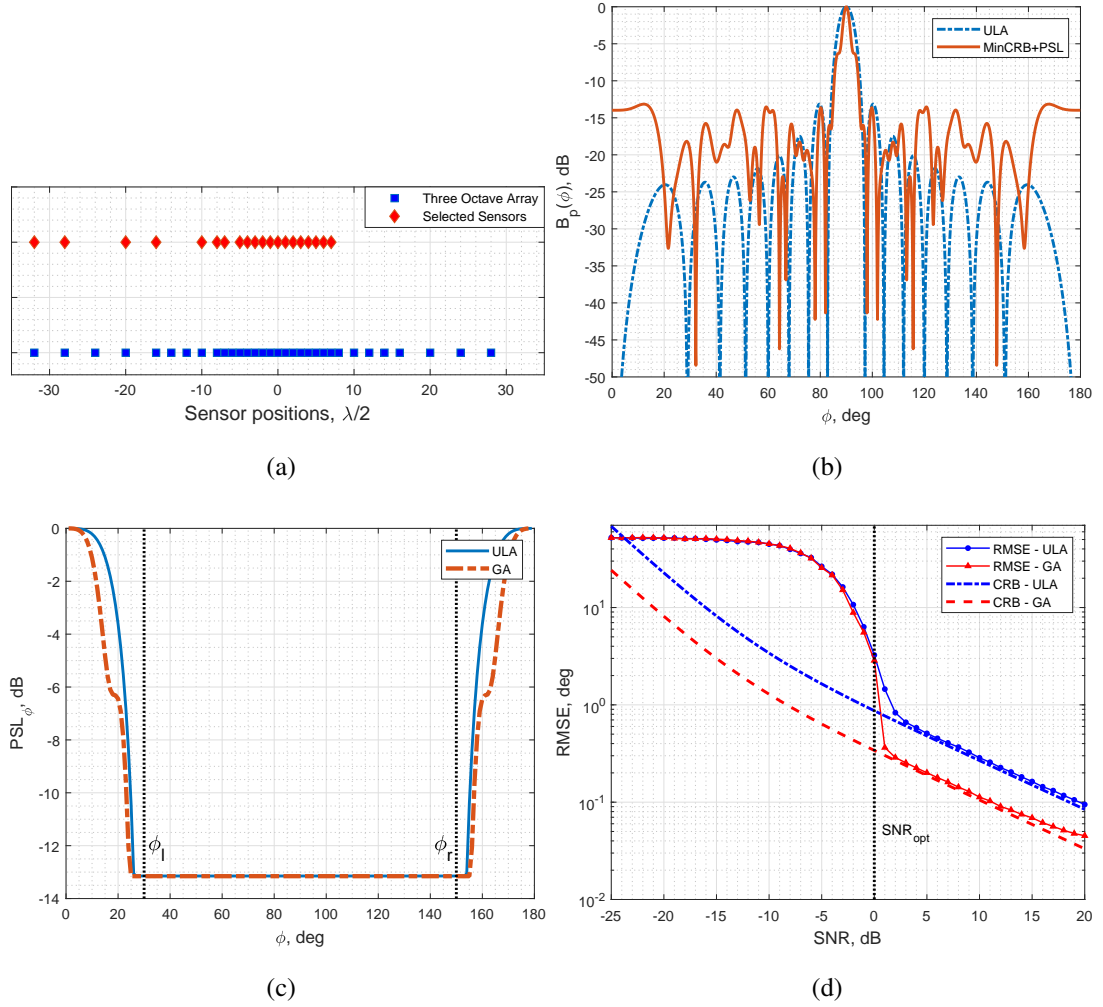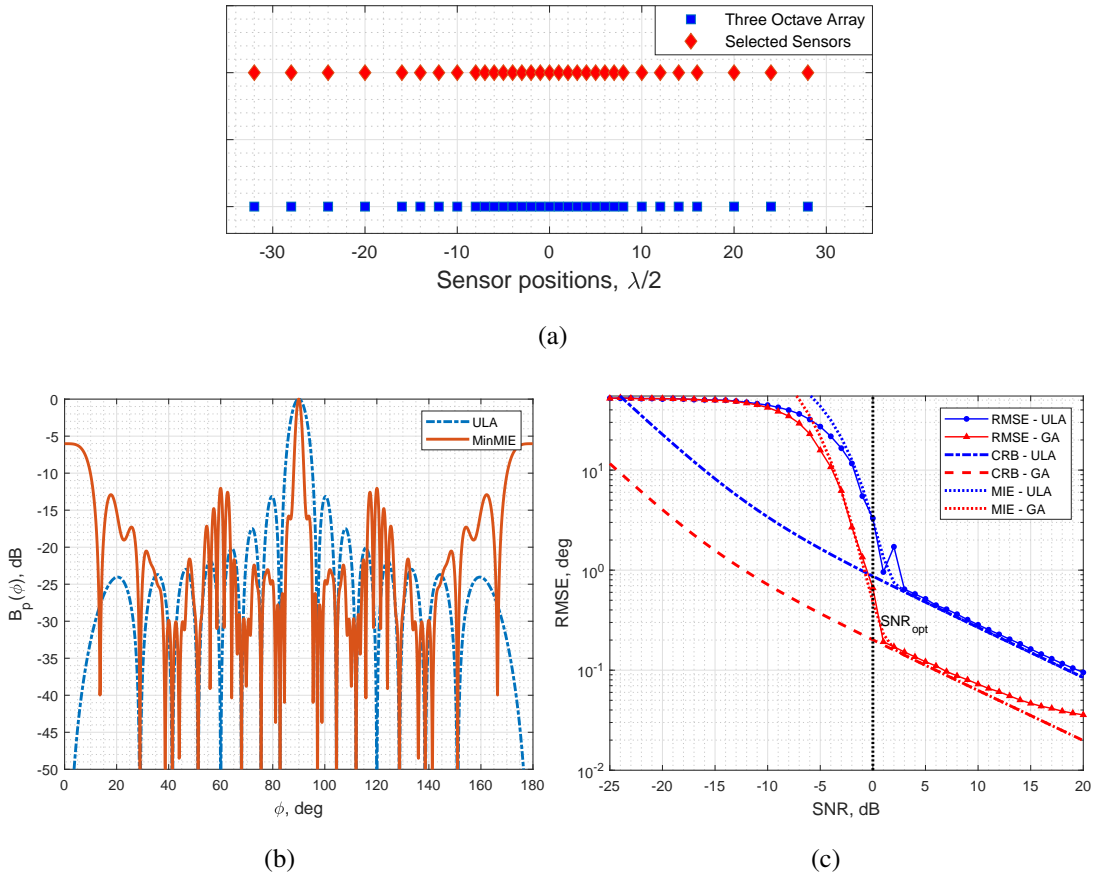

(a)

(b)

(c)

Figure 6.18: (a) Selected sensor positions for minimum Bayesian MIE optimization, (b) beampattern for ULA with $M = 16$ and MinMIE with $M = 32$, (c) RMSE - SNR for Bartlett method using 16 sensor ULA and 32 sensor MinMIE with $\text{SNR}_{\text{opt}} = 0$ dB, $P = 1$, $N = 1$, $N_{\text{MTC}} = 10000$, $\phi_l = 30°$, $\phi_r = 150°$

In Figure 6.18a, sensor positions of selected array layout are shown with red markers in addition to the TOA with blue markers. This optimization also chooses all elements of the TOA as the array layout like the minimum CRB optimization. Beampatterns for the selected layout and 16 sensor ULA are shown for the steering angle $\phi_0 = 90°$ in Figure 6.18b. High sidelobes are observed for the selected layout as a result of being a sparse array. In Figure 6.18c, RMSE, Bayesian CRB and Bayesian MIE curves are shown for the selected array and 16 sensor ULA. RMSE and Bayesian MIE values of the selected array layout are lower than ULA since it uses the whole aperture of the TOA.

6.6.5 Minimum Redundancy Optimization

In order to find an optimum array for more than 16 sensors by minimizing redundancy, number of sensors constraint in optimization problem given by Equation 6.11 is replaced with $|\mathbb{S}| > M$. Then, minimum redundancy optimization problem with the new constraint can be stated as

$$
\begin{aligned}
\mathbb{S}_{MRA} &\triangleq \arg\min_{\mathbb{S}} \quad R \\
\text{s.t.} \quad |\mathbb{S}| &> M \\
\mathbb{D} &= \mathbb{U}
\end{aligned}
\tag{6.19}
$$

where R is calculated by using Equation 4.7 and $\mathbb{D} = \mathbb{U}$ means that difference coarray $\mathbb{D}$ is hole-free.

Aim of minimum redundancy optimization is selecting a layout with maximum spatial efficiency of sensor placement. In Figure 6.7c, it is seen that maximum central ULA segment can be obtained by using 16 sensors. Therefore, maximum obtainable aperture length is $40\lambda/2$ for minimum redundancy array selection. In order to obtain minimum redundancy with more than 16 sensors, optimization tries to select minimum number of sensors with an aperture of $40\lambda/2$.

In Figure 6.19a, sensor positions of selected array layout are shown with red markers in addition to the TOA with blue markers. Leftmost element of the TOA is selected in the new array layout to increase the aperture. Difference coarray weight function for the selected array is shown in Figure 6.19c. Redundancy of the selected layout is

3,4 and central ULA length $|\mathbb{U}|$ is 81. Redundancy of this layout is higher than MRA with 16 sensors despite of having same central ULA length. Using an extra sensor does not bring an advantage to the MRA in terms of spatial efficiency.

In Figure 6.19b, beampatterns for MRA obtained with the optimization are shown when the array is steered to $90°$. Beampattern using Bartlett beamformer is plotted with blue dash-dots and the one for spatially smoothed difference coarray is plotted with red line. Lower sidelobe levels are observed with the PSL being -13 dB since the beamforming is done by using the coarray elements.
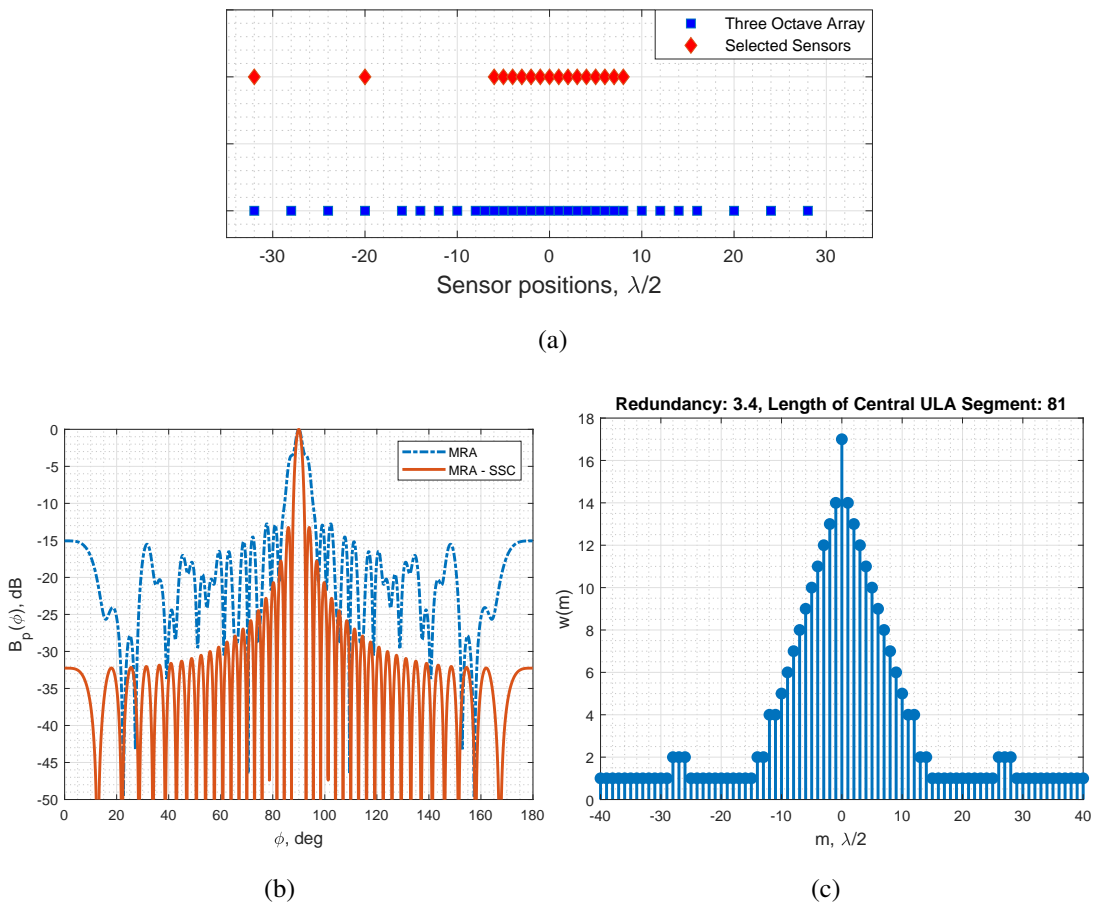

(a)

(b)

(c)

Figure 6.19: (a) Selected sensor positions for minimum redundancy optimization, (b) beampattern using Bartlett and Spatially Smoothed Coarray for MRA with $M = 17$, (c) weight function of difference coarray for MRA with $M = 17$

6.6.6 Robust Minimum Redundancy Optimization

For selecting more than 16 sensors, robust minimum redundancy optimization given in Equation 6.14 can be modified by replacing sensor number constraint with $|\mathbb{S}| > M$ and fragility constraint with $M_{essential} = 2$. Then, robust minimum redundancy optimization problem with the new constraint can be stated as

$$
\begin{aligned}
\mathbb{S}_{RMRA} &\triangleq \arg\min_{\mathbb{S}} \quad R \\
\text{s.t.} \quad |\mathbb{S}| &> M \\
\mathbb{D} &= \mathbb{U} \\
M_{essential} &= 2 \\
M &\geq 4
\end{aligned}
\tag{6.20}
$$

where R is calculated by using Equation 4.7 and $\mathbb{D} = \mathbb{U}$ means that difference coarray $\mathbb{D}$ is hole-free. There is a tradeoff between central ULA length of difference coarray and robustness against sensor failure. In Figure 6.10c, it is seen that maximum central ULA length which is equal to $16\lambda/2$ can be obtained using 16 sensors. This length cannot exceed this number when the number of selected sensors is higher than 16. In order to keep redundancy minimum, minimum number of sensors is selected by the optimization.

In Figure 6.20a, sensor positions of selected array layout are shown with red markers in addition to the TOA with blue markers. Using the constraint of having two essential sensors and fixed sensor positions forces the optimization to select a 17 sensor ULA as the new layout. Difference coarray weight function for the selected array are shown in Figure 6.20c. Redundancy of the selected layout is 8,5 and central ULA length $|\mathbb{U}|$ is 33. Main aim of robust minimum redundancy array optimization is to find a robust array as much as ULA with less redundancy. Since the optimization can choose elements from fixed sensor positions of the TOA, it does not find a different array than ULA. Also higher redundancy and same central ULA length is obtained when compared with RMRA with 16 sensors.

In Figure 6.20b, beampatterns for RMRA obtained with the optimization are shown when the array is steered to $90°$. Beampattern using Bartlett beamformer is plotted with blue dash-dots and the one for spatially smoothed difference coarray is plotted with red line. PSL of the spatially smoothed coarray is higher than PSL of the

beampattern generated with Bartlett method, whereas the beamwidths are same.

(a)

(b)

(c)
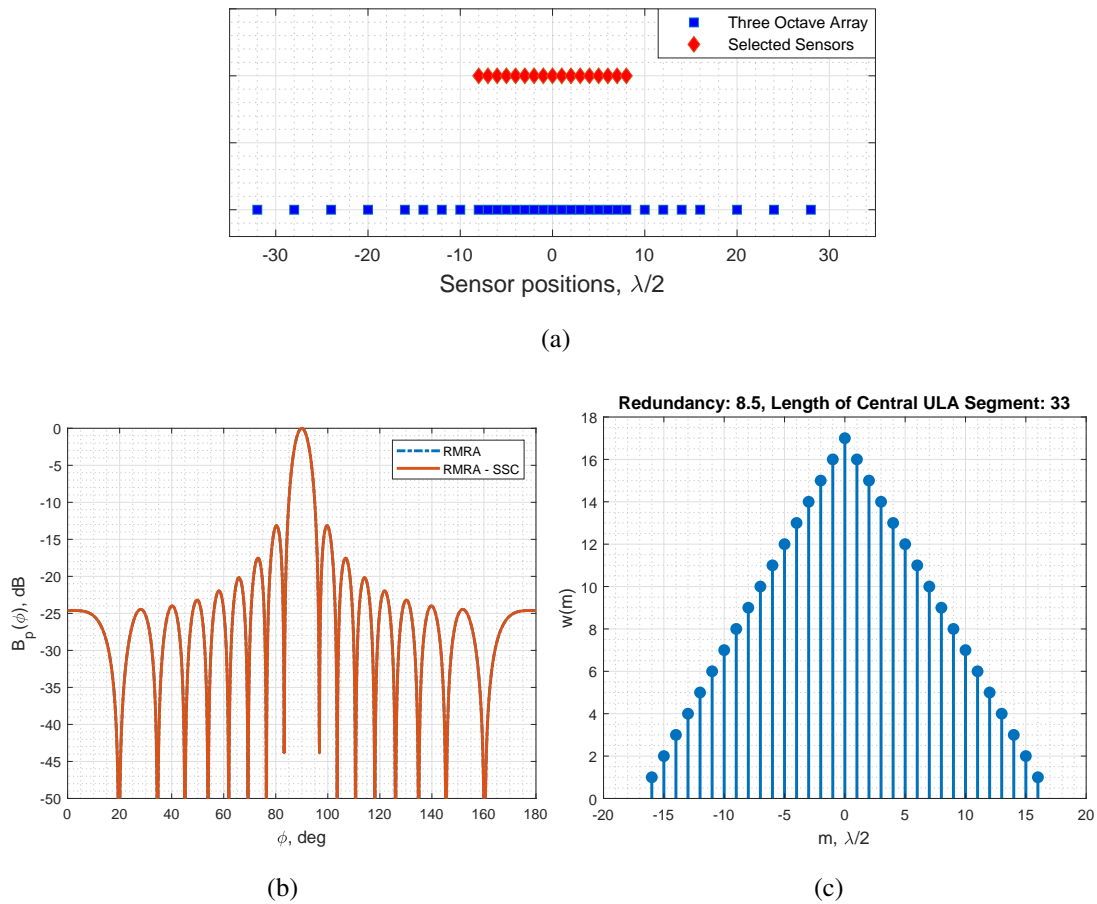
Figure 6.20: (a) Selected sensor positions for robust minimum redundancy optimization, (b) beampattern using Bartlett and Spatially Smoothed Coarray for RMRA with $M = 17$, (c) weight function of difference coarray for RMRA with $M = 17$

6.7 Performance Comparison of the Arrays Found by Optimization (M>16)

Array layout optimization results with more than 16 sensors for different cost functions are provided in section 6.6. Proposed array layouts and 16 sensor ULA are compared in terms of DOA estimation method, DOF and aperture length in Table 6.2. Bartlett beamformer is used for DOA estimation for all of the arrays in the table except for MRA and RMRA which use SS-MUSIC technique. DOFs of MRA and RMRA are 81 and 33 in the coarray domain. However, DOFs are reduced to 41 and

17 as a consequence of spatial smoothing. Aperture lengths in the table are given as a multiple of Nyquist distance $\lambda/2$ for 4 kHz. Apertures of MRA and RMRA are 40 and 16 according to Figures 6.19a and 6.20a. But, they are reduced to 20 and 8 after smoothing the array for SS-MUSIC. Minimum aperture in Table 6.2 is 8 and belongs to RMRA, whereas maximum aperture is 60 for the arrays obtained with minimum CRB and minimum MIE optimization. Throughout this section, arrays obtained in 6.6.1, 6.6.2, 6.6.3, 6.6.4, 6.6.5, 6.6.6 are denoted by MinMaxPSL, MinCRB, MinCRB+PSL, MinMIE, MRA and RMRA respectively.

Table 6.2: Number of sensors (M), DOA estimation methods, DOFs and aperture lengths and computation times for different arrays with more than 16 sensors

Array Type	M	Method	DOF	Aperture ($\lambda/2$)	Time (ms)
ULA	16	Bartlett	16	15	6,03
MinMaxPSL	18	Bartlett	18	20	6,06
MinCRB	32	Bartlett	32	60	7,94
MinCRB+PSL	20	Bartlett	20	39	6,31
MinMIE	32	Bartlett	32	60	7,94
MRA	17	SS-MUSIC	41	20	40,68
RMRA	17	SS-MUSIC	17	8	40,68

In Figure 6.21a, array layouts with more than 16 sensors and ULAs with 16, 18, 20 and 32 sensors are compared by calculating RMSE of the angle estimations as a function of SNR for $N = 1$ snapshot, $P = 1$ source, averaged over $N_{\mathrm{MTC}} = 10000$ simulations using deterministic signal model. In each MTC simulation, source DOA is selected randomly from uniform distribution between $\phi_l = 30°$ and $\phi_r = 150°$. MinCRB and MinMIE have the best performances in the asymptotic region, whereas RMRA has the worst performance according to the RMSE values. As mentioned in section 6.5, lower RMS errors are obtained for larger apertures. MinCRB and MinMIE have the best performances in the asymptotic region as a result of having the maximum aperture length. Both subarrays have all 32 elements of three octave array. ULA with 32 sensor has lower threshold SNR and higher RMS errors in the

asymptotic region when it is compared with the three octave array. Since three octave array has a sparse layout, it has higher sidelobes, which results in higher threshold SNR due to the ambiguity. Highest RMSE values belong to RMRA because of the minimum aperture length.
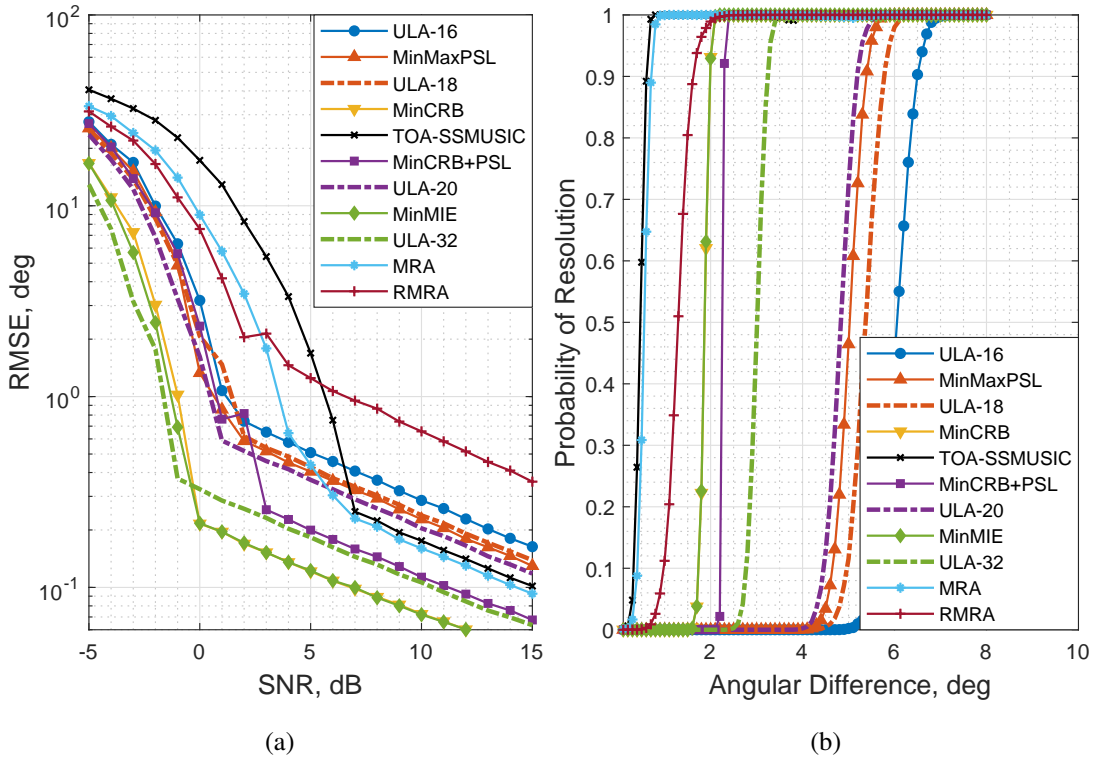
Figure 6.21: (a) RMSE - SNR for 16 sensor ULA and arrays selected by GA with $M > 16$, $P = 1$, $N = 1$, $N_{\mathrm{MTC}} = 10000$, $\phi_l = 30°$, $\phi_r = 150°$, (b) Probability of resolving two sources for 16 sensor ULA and arrays selected by GA with $M > 16$, $P = 2$, $N = 100$, $\mathrm{SNR} = 10$ dB, $N_{\mathrm{MTC}} = 10000$

RMSE performances of MinCRB+PSL, MRA, MinMaxPSL and ULA with 16 sensor are compatible with their apertures given in Table 6.2. Although both subarrays have same number of sensors, threshold SNR of ULA with 20 sensor is lower than the one for MinCRB+PSL. Similar to the relation between three octave array and ULA with 32 sensor, having a larger aperture increases threshold SNR due to the false detections of high sidelobe levels and decreases RMS errors in the asymptotic region as a result of having narrower beamwidth. RMSE performances of MinMaxPSL and ULA with 18 sensors are close to each other because their beampatterns are similar to each other.

Performance of three octave array with SS-MUSIC method is shown with black markers. It is seen that higher RMSE values and threshold SNR are obtained when it is compared with the result of Bartlett beamformer which is shown with yellow (Min-CRB) and green (MinMIE) markers. Aperture of three octave array is reduced to 20 when SS-MUSIC method is used as a result of spatial smoothing and central ULA length. Both MRA and three octave array have same threshold SNR and RMSE values in the asymptotic region using SS-MUSIC since their central ULA length are equal to each other. Despite of having the same aperture length with MinMaxPSL, MRA performs better due to SS-MUSIC method which is a subspace DOA estimator. Minimum threshold SNR is obtained with MinCRB and MinMIE and its value is 0 dB. These two array layouts are the optimum selection among all arrays with lower RMS errors and ability to work at lower SNR values.

Threshold SNR of a layout depends on two parameters which are array gain and sidelobe levels. By using more number of sensors, array gain can be increased and lower threshold SNR is obtained. In Figure 6.21a, it is seen that threshold SNRS of 20 sensor ULA and 32 sensor ULA are 1 and -1 dB respectively. Array gain in linear scale is equal to the number of sensors for ULAs when Equation 2.49 is used. Array gain difference in dB scale between these layouts can be calculated as $10 \log_{10}(32) - 10 \log_{10}(20) = 2$ dB. Sidelobe level is another important parameter for threshold SNR. In Figure 6.21a, it is seen that threshold SNR of ULA with 32 sensors is lower than three octave array although they have same number of sensors. Peak to sidelobe level of ULA with 32 sensor is -13,5 dB and it is -6 dB for three octave array. Having higher sidelobe levels increase the ambiguity in DOA estimation problem. Therefore, higher threshold SNR is obtained with the three octave array.

In Figure 6.22a, probability of detection is estimated as a function of SNR for given arrays using $N = 1000$ snapshots and stochastic signal model. There are $P = 9$ sources at $\{30°, 45°, 60°, 75°, 90°, 105°, 120°, 135°, 150°\}$. Equation 6.4 is used for estimating the probability of detection with source number estimation using MDL method. Probabilities are calculated by averaging the results of $N_{\mathrm{MTC}} = 10000$ simulations. Detection performances of all arrays increase with increasing SNR and equal to 1 after some point. MRA has the best detection performance because it can operate at lower SNR values with high probabiliy of detection. Three octave array with

SS-MUSIC method has similar detection performance since central ULA segment for both arrays is same. Performances of MinMaxPSL, MinCRB+PSL and three octave array (MinCRB and MinMIE) are worse than the ULAs with same number of sensors (ULA-18, ULA-20 and ULA-32). Three octave array (MinCRB and MinMIE) has the worst detection performance because of having high sidelobe levels in its beam-pattern caused by sparsity. High sidelobes bring an ambiguity in DOA estimation because of false target detection. This ambiguity problem could be solved by using other DOA estimation techniques such as dual apodization. For source SNR values higher than 1 dB, all subarray layouts can detect 9 sources correctly.
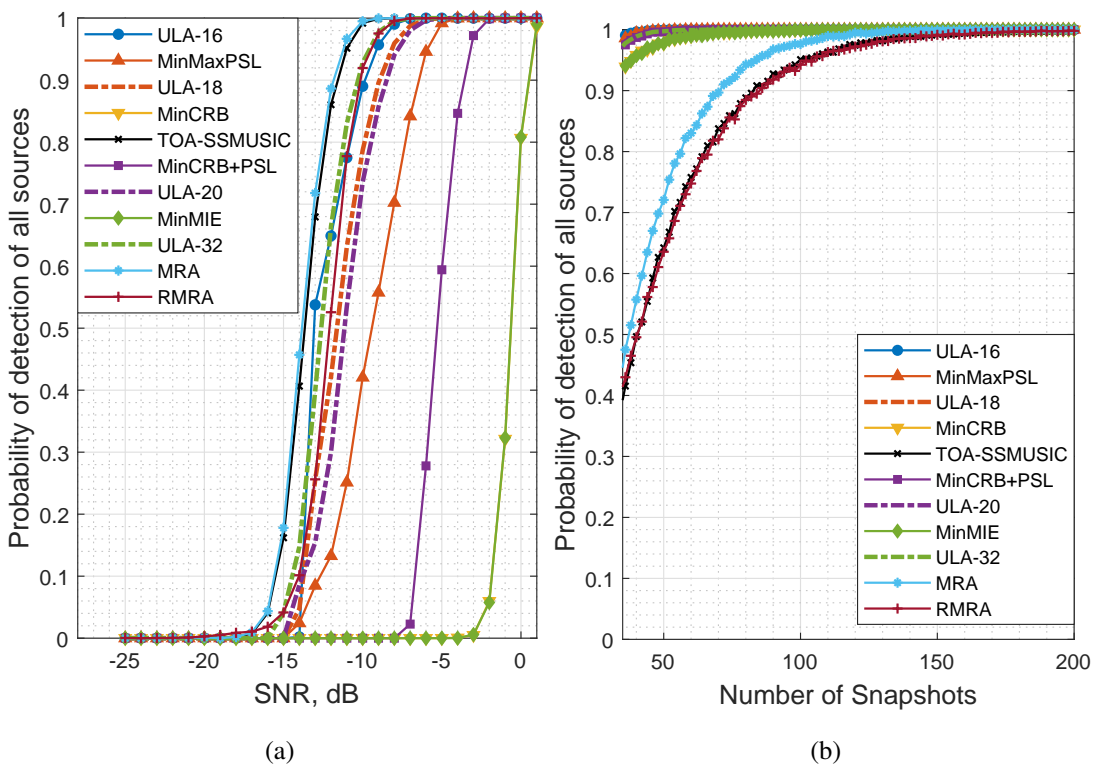
Figure 6.22: Probability of detection of all sources for 16 sensor ULA and arrays selected by GA using $M > 16$, $P = 9$, $N_{\mathrm{MTC}} = 10000$, Source DOA Angles $= \{30°, 45°, 60°, 75°, 90°, 105°, 120°, 135°, 150°\}$ as a function of (a) SNR with $N = 1000$ and (b) number of snapshots with $\mathrm{SNR} = 5$ dB

In Figure 6.22b, probability of detection is estimated as a function of snapshots for given arrays using $\mathrm{SNR} = 5$ dB and the remaining simulation parameters are same

with the ones used for Figure 6.22a. Detection performances of all arrays increase rapidly with increasing number of snapshots. MRA and RMRA have lower probability of detection when the number of snapshots is below 200 because SS-MUSIC requires more snapshots than classical methods such as Bartlett beamformer. Three octave array has a similar performance when it is used with SS-MUSIC. Remaining subarrays perform similar to each other.

In Figure 6.21b, probability of resolving two sources is shown as a function of angular difference between DOAs of the sources using stochastic source model. Equation 6.6 is used for calculating the probability of resolution with $\mathrm{SNR} = 10$ dB, $N = 100$ snapshots and $N_{\mathrm{MTC}} = 10000$ simulations. MRA has the best performance with the ability to detect two sources with $1°$ angular difference. Three octave array has the same performance with SS-MUSIC because of having same central ULA segment in its difference coarray. ULA with 16 sensor performs worst since its aperture is the smallest and Bartlett beamformer is used for DOA estimation. Having the advantage of SS-MUSIC which is a superresolution method, RMRA performs better than the most of the arrays despite of a small aperture. Capability of resolving two closed sources is the highest for MinCRB and MinMIE among the arrays which uses Bartlett beamformer. Similar to the RMSE performances in Figure 6.21a, probability of resolution performance also depends on the array aperture in addition to the DOA estimation method. Performances of MinMaxPSL, MinCRB+PSL and three octave array (MinCRB and MinMIE) are better than the ULAs with same number of sensors (ULA-18, ULA-20 and ULA-32) as a result of wider aperture.

According to results presented in this section, three octave array (MinCRB and Min-MIE) outperform other arrays with lower RMS error, lower threshold SNR and higher resolution for target separation despite of a relatively worse performance of detecting multiple sources using Bartlett beamformer. Detection performance of a layout is not directly related to the number of sensors. High sidelobe levels are observed for three octave array since it is a sparse array. Sparsity of the array increases false target detection which is the reason for poor detection performance at low SNR values. In Figures 6.23a and 6.23b, waterfall displays of Bartlett beamformer output for ULA with 16 sensor (octave-3) and three octave array are shown. In Figure 6.23b, peaks at $0°$, $60°$, $90°$, $120°$ and $180°$ are available although there is one source at $90°$. Except for $90°$,

these peaks are appeared in the display because of the high sidelobes of three octave array. Existence of them may confuse the user and they can be classified as targets which do not exist in the environment. Using other DOA estimation methods such as SS-MUSIC and dual apodization can solve this ambiguity problem. MinCRB+PSL is also an optimum solution in terms of the multiple source detection performance. MRA with 17 sensors is not advantageous as MRA with 16 sensors because central ULA length is not increased.
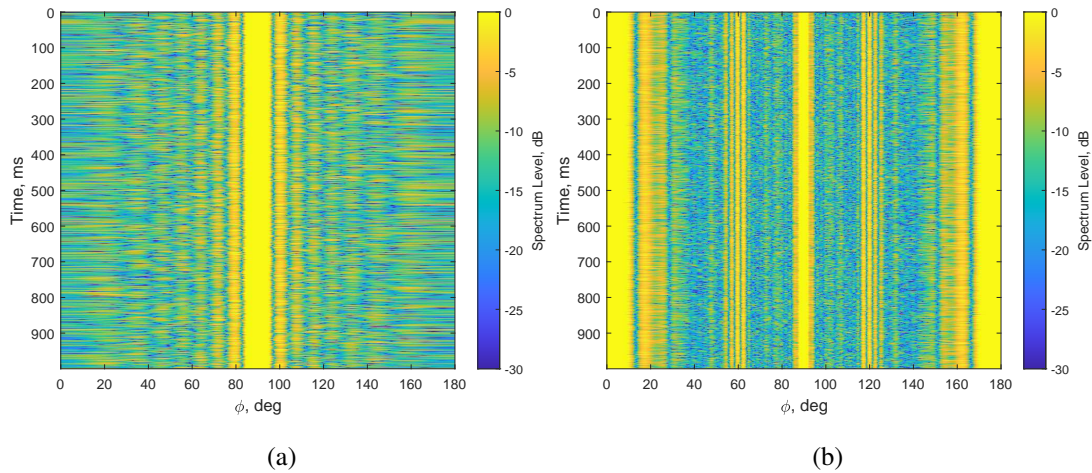

Figure 6.23: Waterfall displays of Bartlett beamformer output using $P = 1,\ \mathrm{SNR} = 10$ dB, $\phi_s = 90°$ for (a) ULA $(M = 16)$, (b) three octave array $(M = 32)$

6.8 Two-Subarray-Layouts With Dual Apodization

SS-MUSIC is superior to the Bartlett beamfomer as a DOA estimator in terms of RMS error for angle estimation and target separation despite of high computational complexity. Dual apodization is a low computational cost method which could bring the narrow beamwidth and low PSL at the same time. Subarrays for this method can be chosen by the genetic algorithm using different cost functions. In [52], both layout and weights for the subarrays are found using the genetic algorithm by minimizing the peak sidelobe level between the first null points of the two subarrays for broadside steering. In this section, array layouts from section 6.4 and TOA are used as the sub-arrays for dual apodization. Weight vectors for the subarrays are fixed and calculated

using Equations 3.45 and 3.46. Three different two-subarray-layouts are given with their beampatterns and spatial spectra.

6.8.1 Layout - 1 for Dual Apodization

(a)

(b)

(c)

Figure 6.24: (a) Sensor positions for Layout - 1, (b) beampatterns of Subarray-1 and Subarray-2 for Layout-1, (c) spatial spectra of Subarray-1, Subarray-2 and dual apodization for Layout-1 with $N = 1000$, $P = 2$, $\mathrm{SNR} = 20$ dB, Source DOA Angles = $\{85°, 95°\}$

In the first layout, both subarrays have 16 sensors. MinCRB explained in 6.4.2 is selected as subarray-1 to reach the maximum aperture of TOA for obtaining the minimum beamwidth. ULA is selected as subarray-2 to obtain low sidelobe levels. Similar layout selection is also used in [10]. In Figure 6.24a, sensor positions of subarray-2 are shown with red markers in addition to subarray-1 with blue markers. Beampat-

terns for the selected subarrays are shown for the steering angle $\phi_0 = 90°$ in Figure 6.24b. An example of spatial spectra for subarray-1 (MinCRB), subarray-2 (ULA) and dual apodization method are illustrated in Figure 6.24c. These spectra are generated by using *N = 1000* snapshots. There are *P = 2* narrowband sources with *SNR = 20 dB* and DOA angles of them are $\{85°, 95°\}$. Grating lobes caused by MinCRB are removed by ULA while preserving the narrow beamwidth. However, high level peaks are observed around the source DOAs, which may increase the false alarms.

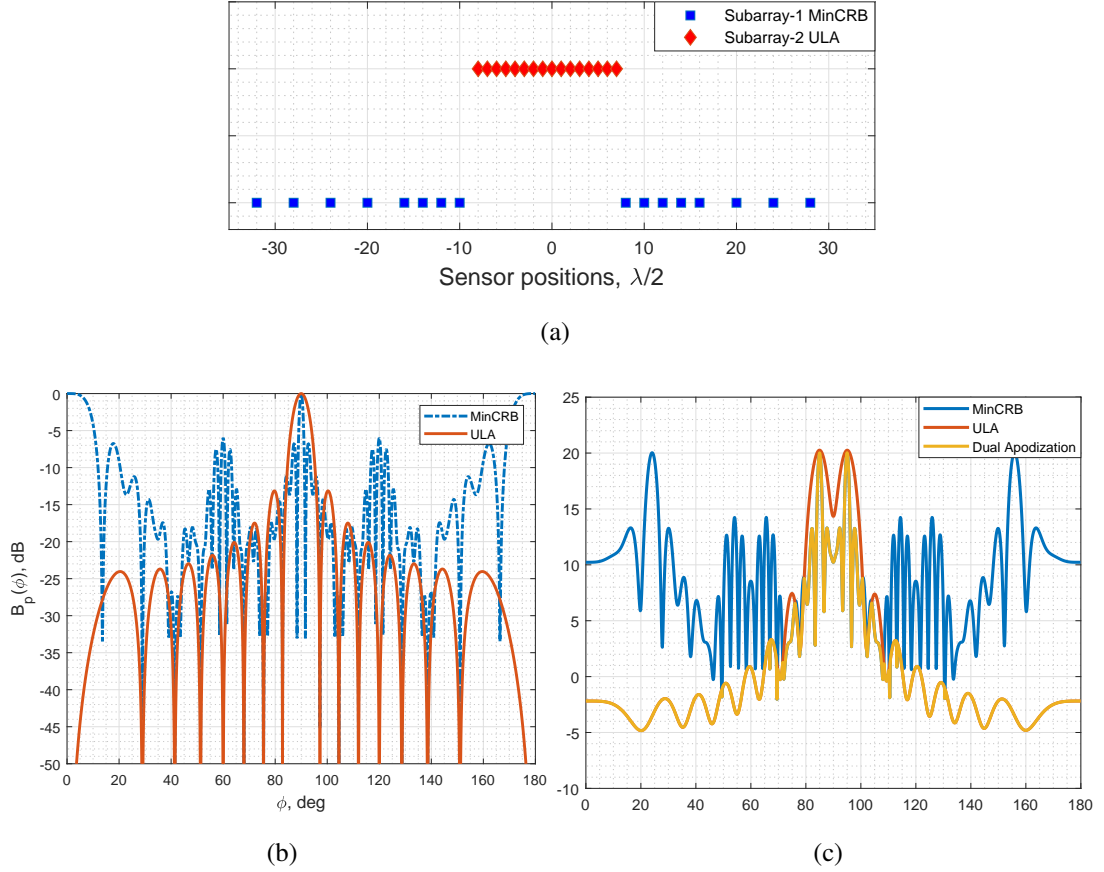### 6.8.2 Layout - 2 for Dual Apodization
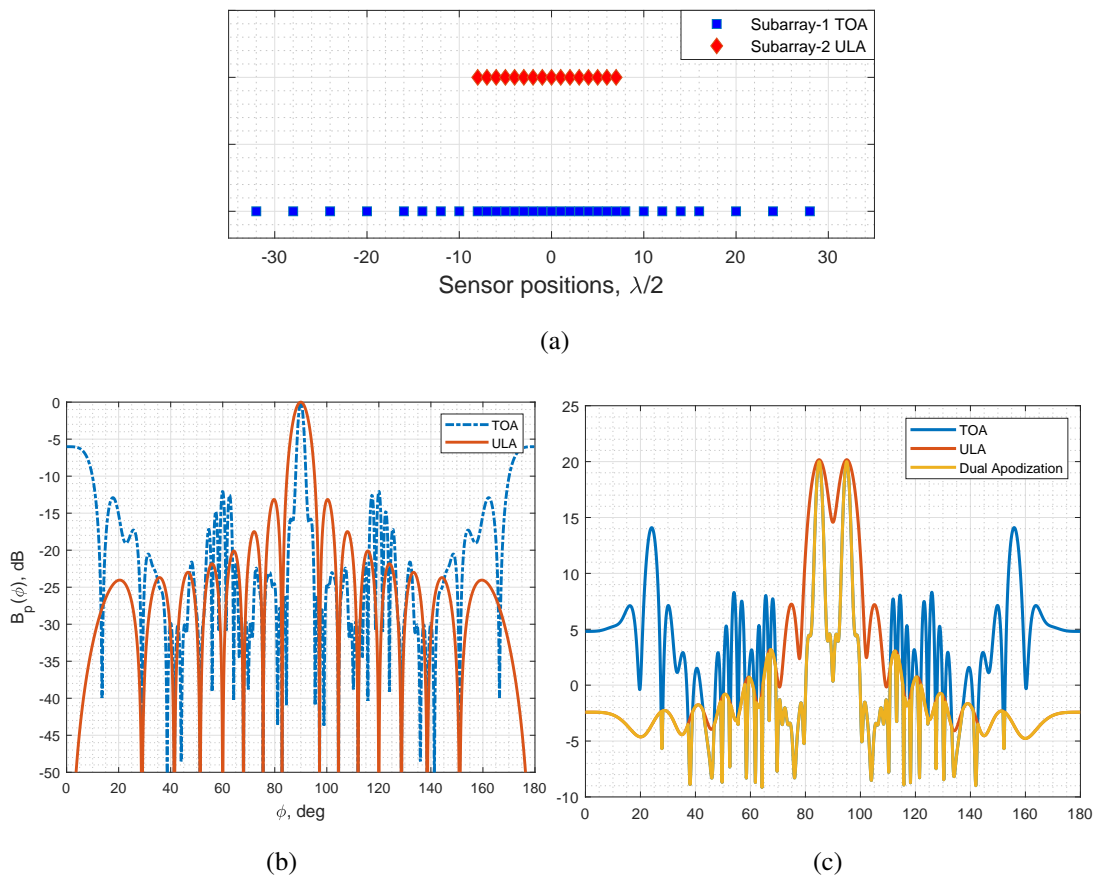

(a)

(b)

(c)

Figure 6.25: (a) Sensor positions for Layout - 2, (b) beampatterns of Subarray-1 and Subarray-2 for Layout-2, (c) spatial spectra of Subarray-1, Subarray-2 and dual apodization for Layout-2 with $N = 1000$, $P = 2$, $\mathrm{SNR} = 20$ dB, Source DOA Angles $= \{85°, 95°\}$

In the second layout, TOA is selected as subarray-1 to reach the maximum aperture and maximize the array gain. ULA is selected as subarray-2 to obtain low sidelobe levels. In Figure 6.25a, sensor positions of subarray-2 are shown with red markers in addition to subarray-1 with blue markers. Beampatterns for the selected subarrays are shown for the steering angle $\phi_0 = 90°$ in Figure 6.25b. An example of spatial spectra for subarray-1 (TOA), subarray-2 (ULA) and dual apodization method are illustrated in Figure 6.25c. These spectra are generated by using $N = 1000$ snapshots. There are $P = 2$ narrowband sources with $\mathrm{SNR} = 20$ dB and DOA angles of them are $\{85°, 95°\}$. High sidelobes caused by TOA are removed by ULA while preserving the narrow beamwidth.

6.8.3   Layout - 3 for Dual Apodization

In the third layout, TOA is selected as subarray-1 to reach the maximum aperture and maximize the array gain. MinMaxPSL explained in 6.4.1 is selected as subarray-2 to obtain lowest sidelobe levels for 16 sensor arrays given in 6.4. In Figure 6.26a, sensor positions of subarray-2 are shown with red markers in addition to subarray-1 with blue markers. Beampatterns for the selected subarrays are shown for the steering angle $\phi_0 = 90°$ in Figure 6.26b. An example of spatial spectra for subarray-1 (TOA), subarray-2 (MinMaxPSL) and dual apodization method are illustrated in Figure 6.25c. These spectra are generated by using $N = 1000$ snapshots. There are $P = 2$ narrowband sources with $\mathrm{SNR} = 20$ dB and DOA angles of them are $\{85°, 95°\}$. It is observed that dual apodization spectrum of Layout-3 is similar to the spectrum of Layout-2 since layout of MinMaxPSL shows similarities with ULA.
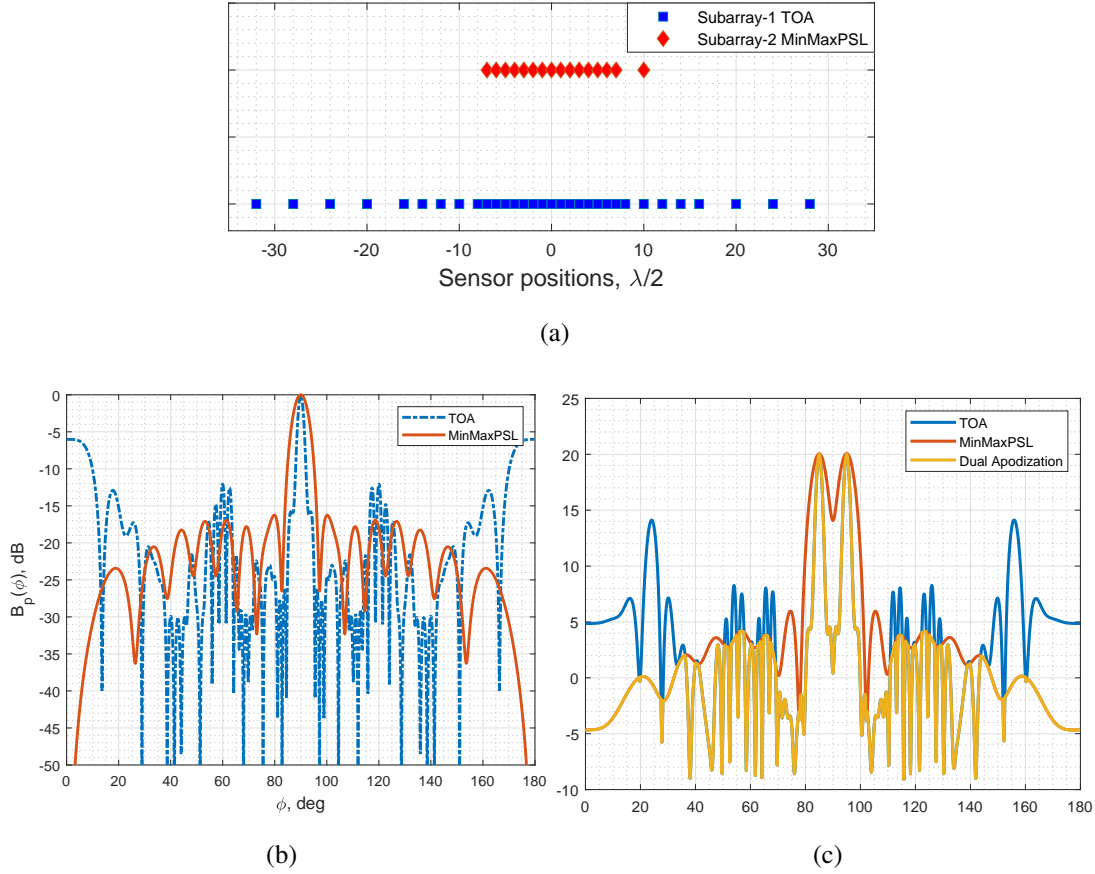
Figure 6.26: (a) Sensor positions for Layout - 3, (b) beampatterns of Subarray-1 and Subarray-2 for Layout-3, (c) spatial spectra of Subarray-1, Subarray-2 and dual apodization for Layout-3 with $N = 1000$, $P = 2$, SNR $= 20$ dB, Source DOA Angles $= \{85°, 95°\}$

6.9 Performance Comparison of the Two-Subarray-Layouts With Dual Apodization

Results of two-subarray-layouts are provided in section 6.8. All of the proposed array layouts are used with Bartlett beamformer and they have the maximum aperture of TOA. Array layouts are compared according to the RMS errors in DOA estimation, detection and source separation performances.

In Figure 6.27a, array layouts are compared by calculating RMSE of the angle estimations as a function of SNR for $N = 1$ snapshot, $P = 1$ source, averaged over

$N_{\mathrm{MTC}} = 10000$ simulations using deterministic signal model. In each MTC simulation, source DOA is selected randomly from uniform distribution between $\phi_l = 30°$ and $\phi_r = 150°$. Performances of all three proposed layouts are close to each other. There are negligible differences between them. By comparing with 16 sensor ULA, lower RMS values are obtained because of using maximum aperture.
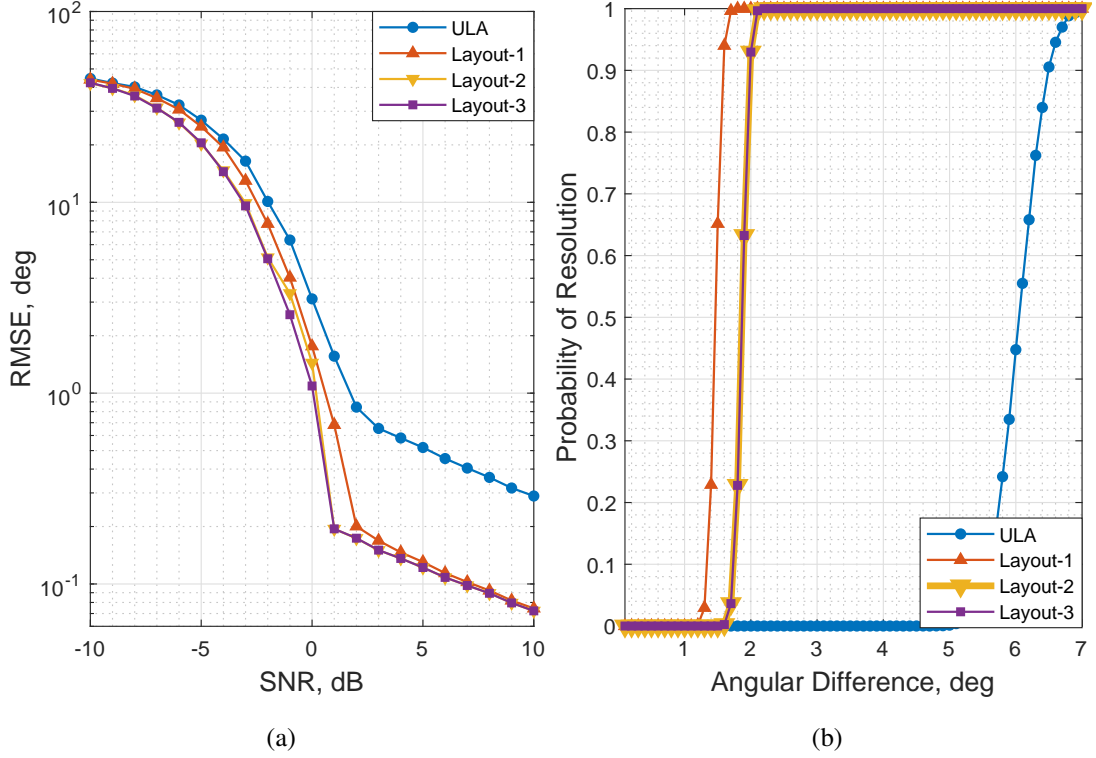
Figure 6.27: (a) RMSE - SNR for 16 sensor ULA and Two-Subarray-Layouts with $P = 1$, $N = 1$, $N_{\mathrm{MTC}} = 10000$, $\phi_l = 30°$, $\phi_r = 150°$, (b) Probability of resolving two sources for 16 sensor ULA and Two-Subarray-Layouts with $P = 2$, $N = 100$, $\mathrm{SNR} = 10$ dB, $N_{\mathrm{MTC}} = 10000$

In Figure 6.28a, probability of detection is estimated as a function of SNR for given arrays using $N = 1000$ snapshots and stochastic signal model. There are $P = 9$ sources at $\{30°, 45°, 60°, 75°, 90°, 105°, 120°, 135°, 150°\}$. Equation 6.4 is used for estimating the probability of detection with source number estimation using Algorithm 3. Probabilities are calculated by averaging the results of $N_{\mathrm{MTC}} = 10000$ simulations. Layout-2 and layout-3 have the best detection performances since both arrays use TOA as subarray-1. Layout-3 performs worse than ULA as a consequence

of grating lobes of MinCRB.

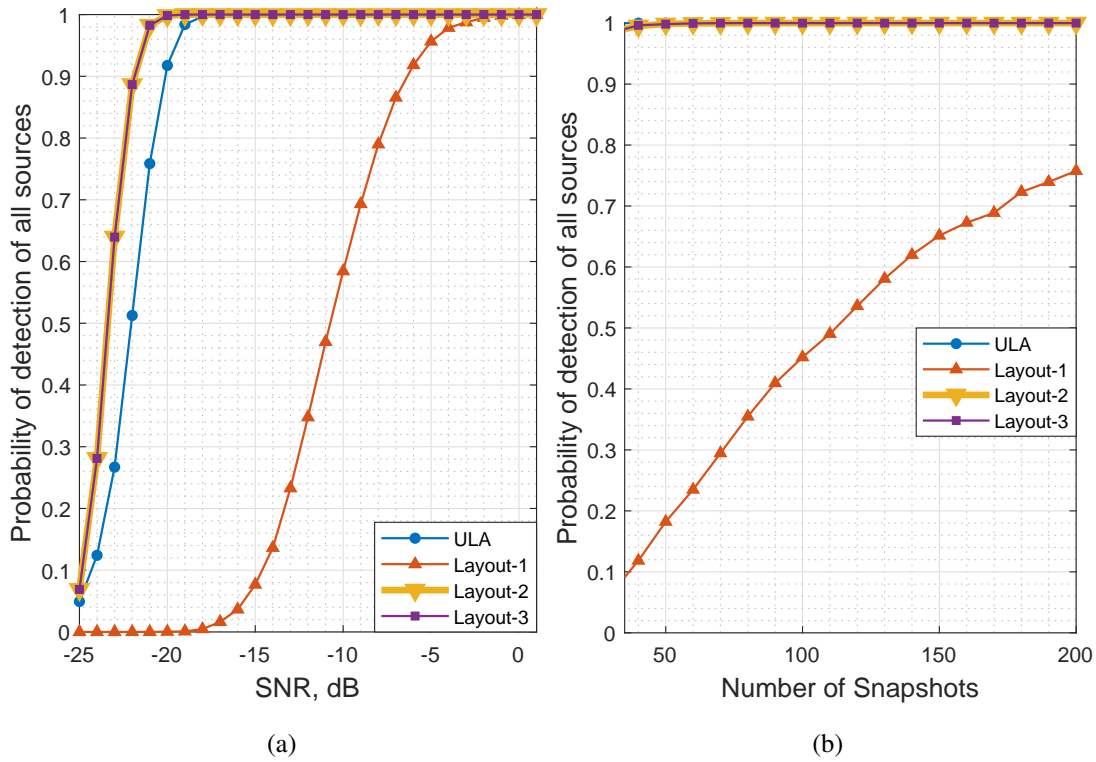Figure 6.28: Probability of detection of all sources for 16 sensor ULA and Two-Subarray-Layouts using $P = 9$, $N_{\mathrm{MTC}} = 10000$, Source DOA Angles $= \{30°, 45°, 60°, 75°, 90°, 105°, 120°, 135°, 150°\}$ as a function of (a) SNR with $N = 1000$ and (b) number of snapshots with $\mathrm{SNR} = 0$ dB

In Figure 6.28b, probability of detection is estimated as a function of snapshots for given arrays using $\mathrm{SNR} = 0$ dB and the remaining simulation parameters are same with the ones used for Figure 6.28a. In this figure, layout-2 and layout-3 also have the same detection performance. Due to the grating lobe problem of its subarray-1, layout-3 has a poor performance and requires more snapshots to reach unit probability.

In Figure 6.27b, probability of resolving two sources is shown as a function of angular difference between DOAs of the sources using stochastic source model. Equation 6.6 is used for calculating the probability of resolution with $\mathrm{SNR} = 10$ dB, $N = 100$ snapshots and $N_{\mathrm{MTC}} = 10000$ simulations. Unlike the RMSE and detection perfor-

mances, layout-1 has the best performance with the ability to detect two sources with
$1, 8°$ angular difference. Performances of layout-2 and layout-3 are also same in this
case. Difference between layout-1 and layout-2 is that first one uses MinCRB as the
subarray-1 while the other uses TOA. Both layout uses ULA as the subarray-2. De-
spite of using the same aperture length, beamwidths of MinCRB and TOA are $1, 5°$
and $2°$ respectively. Having a narrower beamwidth improves the source separation
performance of the array. MinCRB can be modelled as the TOA applied with a win-
dow whose k^{th} elements are zero for $k = \{9, \cdots, 24\}$ and remainin elements are 1.
As the number of elements which take zero values at the center of the array incraese,
beamwidth of the array narrows. In Figure 6.29, it is shown with a beampattern exam-
ple. Beampatterns of three different arrays are plotted and the beamwidth increases
as the number of sensors M increase. Array labelled with $M = 24$ has 24 sensors
from TOA and 8 sensors at the center of TOA are not used.
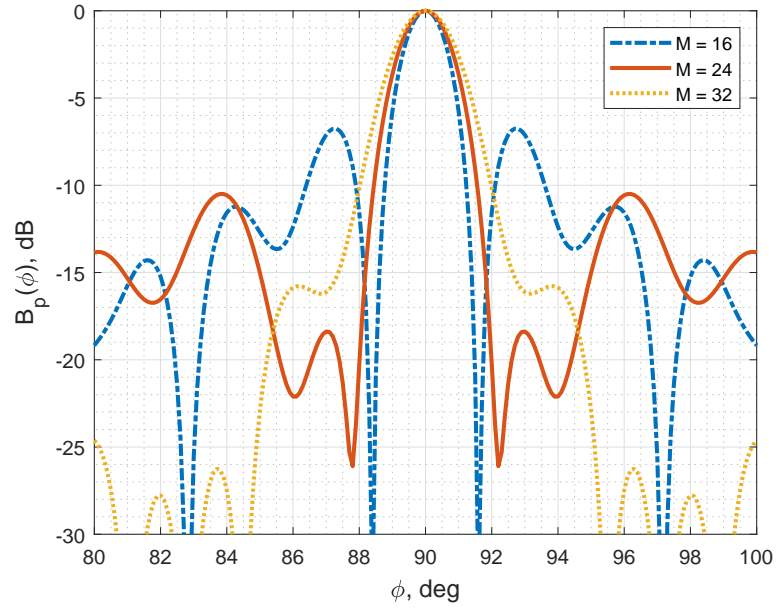
Figure 6.29: Beampatterns of TOA with 16, 8 and 0 sensor gap at the center

According to results presented in this section, Layout-2 and Layout-3 outperform
Layout-1 with a better detection performance. Ambiguity problem of three octave
array is solved by using ULA and MinMaxPSL as second subarrays for dual apodiza-
tion method. Layout-1 seems to be superior in terms of resolution. But, it suffers
from the grating lobes and false alarms related to it.

CHAPTER 7

CONCLUSIONS AND FUTURE WORK

7.1 Conclusions

In this thesis, different approaches to subarray selection problem for octave arrays are studied in optimization framework. Octave arrays are formed by combining a number of uniform line arrays with different element spacings. With conventional DOA estimation methods, only ULA at the center is used for the highest design frequency band. Using sensors apart from the inner ULA increases the aperture, which results in higher resolution and lower error for DOA estimation. In addition, using additional sensors outside the inner ULA increases the array gain and reduces the threshold SNR. Array layouts are selected by genetic algorithm with different cost functions and their performances are presented.

In the second chapter, narrowband signal model and related parameters are explained. Then, classical and coarray based DOA estimation methods are presented in the third and fourth chapters. Information about genetic algorithm and cost functions used in the optimizations are given in the fifth chapter. Optimization problems, their results and performance comparisons are shown in the sixth chapter.

In the fifth chapter, Bayesian CRB and Bayesian MIE are derived for estimating the RMSE performance of arrays for a single source with a random DOA angle. To reduce the false alarms caused by the sidelobes, maximum of peak to sidelobe levels for different steering angles is used as another cost function. Then, a PSL constraint is added to the Bayesian CRB optimization to prevent grating lobes as a result of the selected layout. For finding an optimum array with a hole-free coarray, redundancy and fragility are found for obtaining MRA and RMRA from the elements of the three

octave array.

The proposed cost functions are applied for finding the optimum subarray layouts in the sixth chapter. Layouts with 16 sensors are found with the cost functions to select a new array instead of ULA with the same number of sensors. MRA with 16 sensors has the maximum DOF with SS-MUSIC method, so it can detect more sources than the any other proposed arrays. Bayesian CRB optimization with the PSL constraint gives the best result using 16 sensors for Bartlett beamformer method. Lower RMS errors and higher target separation performance are obtained as a result of using a wider aperture. Then, fixed number of sensors constraint is removed and the optimization problems are modified to find new subarrays with more than 16 sensors. Simulation results for the layouts found by the new optimization problems show that Bayesian CRB optimization with the PSL and the TOA show the best performances with the Bartlett technique. Maximum array gain and aperture length are obtained by using all elements of TOA. To improve the RMSE and resolution performances with a less computational complexity than SS-MUSIC, three different two-subarray-layouts are proposed for using dual apodization method. These layouts are also compared with the same performance metrics that are used for the previous scenarios.

According to the results presented in Chapter 6, there is a trade-off between RMS error for DOA estimation and detection performance for layout selection problem. Selecting a subarray with wider aperture using elements of three octave array results in narrower beamwidth. Less RMS error in the asymptotic region and higher resolution could be obtained as a result of having narrower beamwidth. However, a sparse layout is selected from the elements of three octave array when it is aimed to select a wider apeture. High sidelobes and false target detections are observed when the selected layout is sparse. Detection performance degrades as a result of increasing number of false detections.

Threshold SNR is another important array parameter for subarray selection problem. It sets a lower bound on input SNR at which the system can work properly. In Chapter 6, it is seen that array gain and sidelobe level affect the value of threshold SNR. Lower threshold values are observed for the subarrays with higher array gain as a result of using more number of sensors. High sidelobe levels increase the ambiguity in DOA

114

estimation because of the false detections. Threshold SNR values for the layouts with higher sidelobe levels are higher due to the ambiguity problem.

To conclude, it is possible to obtain better array layouts than ULA from the TOA and considerable improvements are observed in terms of RMS errors, detection and resolution performances without increasing the computational complexity. Number of detectable sources could be increased by using sparse ararys such as MRA at the expense of longer computation time.

7.2 Future Work

Although optimum subarrays are found from the discrete positions of the TOA, these optimizations and performance analyses are made for the narrowband signals. In the wideband scenario, sensor spacings in terms of the wavelength are changed for each frequencies. Also, the difference coarrays will be different within the frequency band of the wideband. Idea of finding a subarray with the genetic algorithm can be extended to the wideband signals as a future work. Optimizations presented in this thesis are limited to the linear arrays. Further work can be done for finding a more generalized optimization for any type of array. It is seen that SS-MUSIC technique is a superior DOA algorithm despite of its high computational complexity. A low complexity superresolution method with spatial smoothing could be proposed to solve this issue in the future.

REFERENCES

[1] A. D. Waite, *Sonar for practising engineers*. Wiley, 2002.

[2] K. Becker and J. Preston, "The ONR five octave research array (FORA) at Penn State," in *Oceans 2003. Celebrating the Past... Teaming Toward the Future (IEEE Cat. No. 03CH37492)*, vol. 5, pp. 2607–2610, IEEE, 2003.

[3] M. S. Bartlett, "Smoothing periodograms from time-series with continuous spectra," *Nature*, vol. 161, no. 4096, pp. 686–687, 1948.

[4] H. Krim and M. Viberg, "Two decades of array signal processing research: the parametric approach," *IEEE Signal Process. Mag.*, vol. 13, no. 4, pp. 67–94, 1996.

[5] J. Capon, "High-resolution frequency-wavenumber spectrum analysis," *Proceedings of the IEEE*, vol. 57, no. 8, pp. 1408–1418, 1969.

[6] K. Buckley and L. Griffiths, "An adaptive generalized sidelobe canceller with derivative constraints," *IEEE Trans. Antennas Propag.*, vol. 34, no. 3, pp. 311–319, 1986.

[7] S. L. Wilson, "Convergence of the SMI and the diagonally loaded SMI algorithms with weak interference," *IEEE Trans. Antennas Propag.*, vol. 38, no. 3, 1990.

[8] P. Stoica, Z. Wang, and J. Li, "Robust capon beamforming," in *Conference Record of the Thirty-Sixth Asilomar Conference on Signals, Systems and Computers, 2002.*, vol. 1, pp. 876–880, IEEE, 2002.

[9] H. C. Stankwitz, R. J. Dallaire, and J. R. Fienup, "Nonlinear apodization for sidelobe control in SAR imagery," *IEEE Trans. Aerosp. Electron. Syst.*, vol. 31, no. 1, pp. 267–279, 1995.

[10] E. Epçaçan, T. Çiloğlu, Ç. Candan, and E. Mehmetcik, "Removing grating lobes in sparse sensor arrays with a nonlinear approach," in *2015 23nd Signal Processing and Communications Applications Conference (SIU)*, pp. 1950–1953, IEEE, 2015.

[11] R. Schmidt, "Multiple emitter location and signal parameter estimation," *IEEE Trans. Antennas Propag.*, vol. 34, no. 3, pp. 276–280, 1986.

[12] R. Roy and T. Kailath, "ESPRIT-estimation of signal parameters via rotational invariance techniques," *IEEE Trans. Acoust., Speech, Signal Process.*, vol. 37, no. 7, pp. 984–995, 1989.

[13] A. Moffet, "Minimum-redundancy linear arrays," *IEEE Trans. Antennas Propag.*, vol. 16, no. 2, pp. 172–175, 1968.

[14] E. Vertatschitsch and S. Haykin, "Nonredundant arrays," *Proceedings of the IEEE*, vol. 74, no. 1, pp. 217–217, 1986.

[15] C.-L. Liu and P. Vaidyanathan, "Robustness of coarrays of sparse arrays to sensor failures," in *2018 IEEE International Conference on Acoustics, Speech and Signal Processing (ICASSP)*, pp. 3231–3235, IEEE, 2018.

[16] P. Pal and P. P. Vaidyanathan, "Nested arrays: A novel approach to array processing with enhanced degrees of freedom," *IEEE Trans. Signal Process.*, vol. 58, no. 8, pp. 4167–4181, 2010.

[17] W.-K. Ma, T.-H. Hsieh, and C.-Y. Chi, "DOA estimation of quasi-stationary signals via Khatri-Rao subspace," in *2009 IEEE international conference on acoustics, speech and signal processing*, pp. 2165–2168, IEEE, 2009.

[18] J. H. Holland, *Adaptation in natural and artificial systems*. Ann Arbor: The University of Michigan Press, 1975.

[19] D. E. Goldberg, *Genetic algorithms in search, optimization, and machine learning*. Addison-Wesley Publishing Company, 1989.

[20] J. E. Baker, "Adaptive selection methods for genetic algorithms," in *Proceedings of an International Conference on Genetic Algorithms and their applications*, vol. 1, Hillsdale, New Jersey, 1985.

[21] R. Poli, J. Kennedy, and T. Blackwell, "Particle swarm optimization," *Swarm intelligence*, vol. 1, no. 1, pp. 33–57, 2007.

[22] R. L. Haupt, "Thinned arrays using genetic algorithms," *IEEE Trans. Antennas Propag.*, vol. 42, no. 7, pp. 993–999, 1994.

[23] W. P. Keizer, "Large planar array thinning using iterative FFT techniques," *IEEE Trans. Antennas Propag.*, vol. 57, no. 10, pp. 3359–3362, 2009.

[24] C. Cui, W. T. Li, X. T. Ye, and X. W. Shi, "Hybrid genetic algorithm and modified iterative Fourier transform algorithm for large thinned array synthesis," *IEEE Antennas Wireless Propag. Lett.*, vol. 16, pp. 2150–2154, 2017.

[25] T. Birinci and Y. Tanık, "Optimization of nonuniform array geometry for DOA estimation with the constraint on gross error probability," *Signal processing*, vol. 87, no. 10, pp. 2360–2369, 2007.

[26] C.-L. Liu and P. Vaidyanathan, "Cramér–Rao bounds for coprime and other sparse arrays, which find more sources than sensors," *Digital Signal Processing*, vol. 61, pp. 43–61, 2017.

[27] F. Athley, "Threshold region performance of maximum likelihood direction of arrival estimators," *IEEE Trans. Signal Process.*, vol. 53, no. 4, pp. 1359–1373, 2005.

[28] H. L. Van Trees, *Optimum array processing: Part IV of detection, estimation, and modulation theory*. John Wiley & Sons, 2004.

[29] R. Bansal, "The far-field: How far is far enough?," *Applied Microwave & Wireless*, vol. 11, no. 11, pp. 59–60, 1999.

[30] T. E. Tuncer and B. Friedlander, *Classical and modern direction-of-arrival estimation*. Academic Press, 2009.

[31] R. G. Gallager, "Circularly-symmetric Gaussian random vectors," *preprint*, pp. 1–9, 2008.

[32] A. Ksienski and R. McGhee, "Radar signal processing for angular resolution beyond the Rayleigh limit," *Radio and Electronic Engineer*, vol. 34, no. 3, pp. 161–174, 1967.

[33] M. Souden, J. Benesty, and S. Affes, "A study of the LCMV and MVDR noise reduction filters," *IEEE Trans. Signal Process.*, vol. 58, no. 9, pp. 4925–4935, 2010.

[34] B. N. Parlett, *The symmetric eigenvalue problem.* SIAM, 1998.

[35] V. V. Reddy, M. Mubeen, and B. P. Ng, "Reduced-complexity super-resolution DOA estimation with unknown number of sources," *IEEE Signal Process. Lett.*, vol. 22, no. 6, pp. 772–776, 2014.

[36] T.-J. Shan, M. Wax, and T. Kailath, "On spatial smoothing for direction-of-arrival estimation of coherent signals," *IEEE Trans. Acoust., Speech, Signal Process.*, vol. 33, no. 4, pp. 806–811, 1985.

[37] J. H. Cozzens and M. J. Sousa, "Source enumeration in a correlated signal environment," *IEEE Trans. Signal Process.*, vol. 42, no. 2, pp. 304–317, 1994.

[38] Y. I. Abramovich, N. K. Spencer, and A. Y. Gorokhov, "Detection-estimation of more uncorrelated Gaussian sources than sensors in nonuniform linear antenna arrays. II. Partially augmentable arrays," *IEEE Trans. Signal Process.*, vol. 51, no. 6, pp. 1492–1507, 2003.

[39] S. U. Pillai, Y. Bar-Ness, and F. Haber, "A new approach to array geometry for improved spatial spectrum estimation," *Proceedings of the IEEE*, vol. 73, no. 10, pp. 1522–1524, 1985.

[40] S. Pillai and F. Haber, "Statistical analysis of a high resolution spatial spectrum estimator utilizing an augmented covariance matrix," *IEEE Trans. Acoust., Speech, Signal Process.*, vol. 35, no. 11, pp. 1517–1523, 1987.

[41] Y. I. Abramovich, D. A. Gray, A. Y. Gorokhov, and N. K. Spencer, "Positive-definite Toeplitz completion in DOA estimation for nonuniform linear antenna arrays. I. Fully augmentable arrays," *IEEE Trans. Signal Process.*, vol. 46, no. 9, pp. 2458–2471, 1998.

[42] Y. I. Abramovich, N. K. Spencer, and A. Y. Gorokhov, "Positive-definite Toeplitz completion in DOA estimation for nonuniform linear antenna arrays. II. Partially augmentable arrays," *IEEE Trans. Signal Process.*, vol. 47, no. 6, pp. 1502–1521, 1999.

[43] R. Kruse, C. Borgelt, C. Braune, S. Mostaghim, M. Steinbrecher, F. Klawonn, and C. Moewes, *Computational intelligence*. Springer, 2011.

[44] K. Sastry, D. Goldberg, and G. Kendall, "Genetic algorithms," in *Search methodologies*, pp. 97–125, Springer, 2005.

[45] G. Syswerda, "Uniform crossover in genetic algorithms," in *Proceedings of the third international conference on Genetic algorithms*, pp. 2–9, Morgan Kaufmann Publishers, 1989.

[46] K. Deep, K. P. Singh, M. L. Kansal, and C. Mohan, "A real coded genetic algorithm for solving integer and mixed integer optimization problems," *Applied Mathematics and Computation*, vol. 212, no. 2, pp. 505–518, 2009.

[47] P. Stoica, E. G. Larsson, and A. B. Gershman, "The stochastic CRB for array processing: A textbook derivation," *IEEE Signal Process. Lett.*, vol. 8, no. 5, pp. 148–150, 2001.

[48] C. D. Richmond, "Capon algorithm mean-squared error threshold SNR prediction and probability of resolution," *IEEE Trans. Signal Process.*, vol. 53, no. 8, pp. 2748–2764, 2005.

[49] M. Wax and T. Kailath, "Detection of signals by information theoretic criteria," *IEEE Trans. Acoust., Speech, Signal Process.*, vol. 33, no. 2, pp. 387–392, 1985.

[50] R. Hunger, *Floating point operations in matrix-vector calculus*. Munich University of Technology, Inst. for Circuit Theory and Signal . . . , 2005.

[51] E. Gentilho, P. R. Scalassara, and T. Abrão, "Direction-of-Arrival Estimation Methods: A Performance-Complexity Tradeoff Perspective," *Journal of Signal Processing Systems*, vol. 92, no. 2, pp. 239–256, 2020.

[52] E. Epcacan and T. Ciloglu, "A hybrid nonlinear method for array thinning," *IEEE Trans. Antennas Propag.*, vol. 66, no. 5, pp. 2318–2325, 2018.